©Copyright 2025
Christopher Earl Woodburn

Advancements in High-pressure Chemistry: Informing Biosignature Detection and Aqueous Salt Equilibria

Christopher Earl Woodburn

A dissertation
submitted in partial fulfillment of the
requirements for the degree of

Doctor of Philosophy

University of Washington

2025

Reading Committee:
Baptiste Journaux, Chair
Brandi M. Cossairt
Gary P. Drobny

Program Authorized to Offer Degree:
Department of Chemistry

University of Washington

Abstract

Advancements in High-pressure Chemistry: Informing Biosignature Detection and Aqueous Salt Equilibria

Christopher Earl Woodburn

Chair of the Supervisory Committee:
Baptiste Journaux
Department of Earth and Space Sciences

High-pressure chemistry is an interdisciplinary science concerned with the behavior of materials often above 100 megapascals (MPa). These conditions—thousands of times greater than atmospheric pressure—facilitate a variety of unique processes and phenomena otherwise inaccessible in the typical laboratory setting. Of note, high-pressure techniques can provide insights into the environments of the outer solar system. With the recent launch of the Europa Clipper (October 2024) and the Dragonfly rotorcraft to Titan (planned 2028), predictive information about icy ocean worlds is vital to both mission success and the search for life elsewhere in the Universe. This dissertation presents advancements in biosignature detection and the mapping of equilibria in salt-water binaries of interest to the chemistry and Earth and space science communities. The activity of an ice-binding peptide against a high-pressure, non-hexagonal phase of ice is evaluated, and the high-pressure melting curves of water ices in the presence of relevant ions for oceans of our solar system are determined. The former, inspired by the life-preserving mechanisms of organisms at boundary conditions on Earth, reveals that the growth of tetragonal ice VI and, by extension, other exotic ice polymorphs can be moderated by ice recrystallization inhibition (IRI) agents. A new method for performing splat assays at high pressure is developed, opening the door for comparable works on the habitability of icy worlds and ocean exoplanets. The latter provides funda-

mental, thermodynamic data characterizing the liquidus lines of water up to 1400 MPa and a three molal (mol/kg) concentration of magnesium sulfate, sodium sulfate, and magnesium chloride. Melting curves are compared to an ideal solution model extended to high pressures, with implications on the behavior of mixed systems and the subsurface oceans of icy worlds. The applications of and possibilities for high-pressure chemistry are endless, and I look forward to seeing future creative advancements in this burgeoning field of research.

TABLE OF CONTENTS

LIST OF FIGURES

LIST OF TABLES

ACKNOWLEDGMENTS

This dissertation would not have been possible without the support of faculty in the Department of Chemistry and the Department of Earth and Space Sciences at the University of Washington. Thanks to my advisor, Professor Baptiste Journaux, for his unwavering guidance and mentorship. Thanks to Professor Brandi Cossairt, Professor Al Nelson, and Graduate Program Coordinator Christine Gormley, for their support and advice. Thanks to Professor Andrea Carroll, for making my time as a TA special. Thanks to Joey Pasterski, PhD; Marshall Seaton, PhD; Dr. Melissa Trainer; and Dr. Morgan Cable—collaborating with you and with NASA was the highlight of my graduate career. And finally, thanks to professors Jim Larrabee and Sunhee Choi, for igniting my passion for chemistry at Middlebury College.

DEDICATION

To Baptiste. For always believing in me.

To Mom, Dad, and Kathryn. For all the love and support.

To Christine. For keeping me sane.

Chapter 1
INTRODUCTION

High-pressure research is a field motivated by curiosity. Its roots can be traced back to the mid-17th century, when questioning minds like Torricelli—who developed the first mercury barometer after a disagreement with his mentor, Galileo—and Pascal discovered that Earth's atmosphere has weight [1]. The contributions of these pioneers are immortalized in the modern-day International System of Units (SI); pascal (Pa) is the SI unit for pressure, and torr (Torr) is the de facto unit for vacuum strength. Since, technological improvements in high-pressure methodology have transformed the field into an interdisciplinary bulwark at the forefront of fundamental, scientific discovery.

1.1 Water at Pressure

Water makes for an interesting case study in the high-pressure field. The behavior of water at pressure is pertinent to the physical sciences, and findings mirror the evolution of high-pressure apparatus. Any material—including pure substances, like water—can exist in a variety of states dependent on pressure and temperature [2]. The preferred state is governed by the Gibbs free energy:

$$G = U - TS + pV \tag{1.1}$$

where at equilibrium G is minimized [3]. At low temperatures T and pressures p, internal energy U is the dominant term. A solid, crystalline structure limits the movement of particles, reducing kinetic energy and selecting ordinary ice Ih as the appropriate phase [2]. At higher temperatures, entropy S overcomes the contribution from internal energy and moves the equilibrium towards phases of increasing disorder. It is important to note that ice Ih is anomalous. As water freezes, the orientation of strong hydrogen bonding interactions

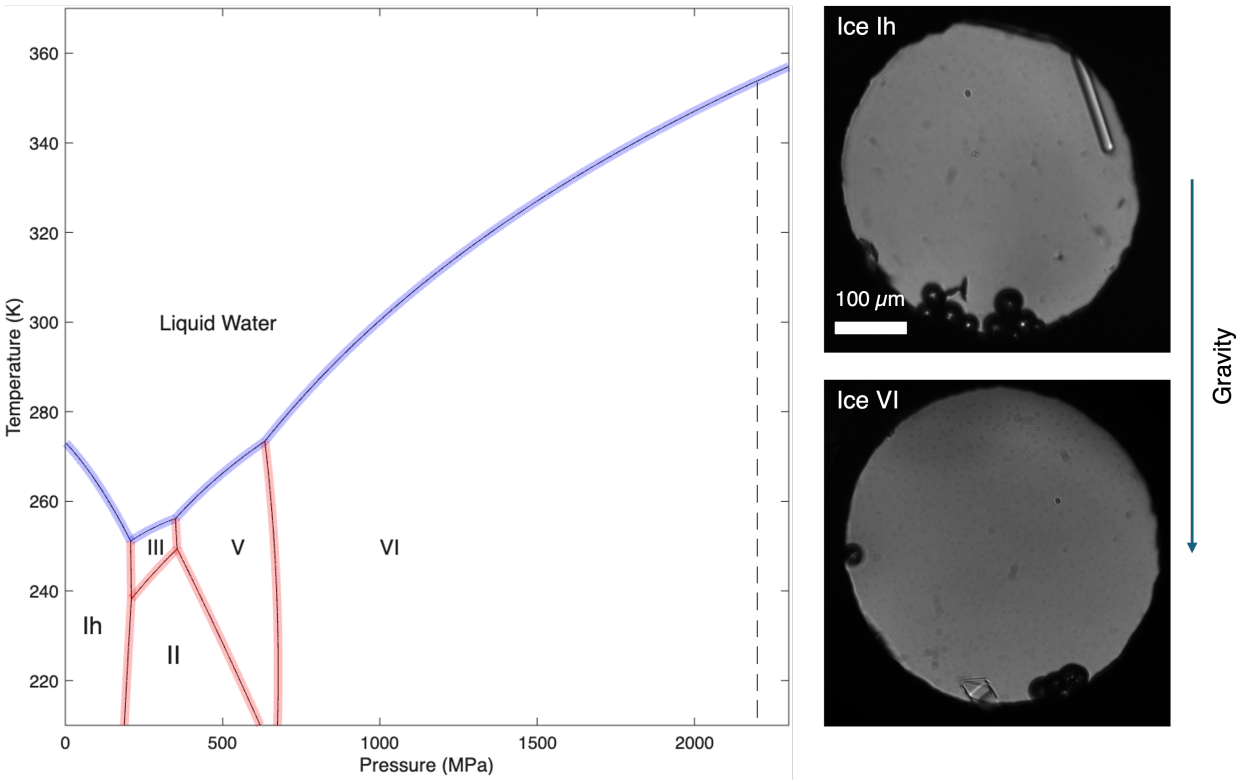

Figure 1.1: Left: phase diagram of water up to 2300 MPa [5]. Highlighted regions indicate melting curves (blue) and solid-solid phase transitions (red) that are thermodynamically constrained and are in agreement with published data [5]. The dashed line at 2200 MPa is the solid-solid phase transition between ices VI and VII. Naming of ices is based on their order of discovery, not their order of appearance on the phase diagram. Right: micrographs of single crystals of ice Ih and ice VI. As suggested by (1.1), ice Ih floats, whereas ice VI sinks (density, 1.31 g cm^{-3}) [6]. Dark spheres are ruby chips used as pressure calibrants. The scale bar is 100 µm for both micrographs.

between molecules pushes them farther apart, creating a larger volume as compared to the liquid fraction. This is observed physically (ice Ih floats above liquid water) and is reflected in the phase diagram—the Clapeyron equation for ice Ih is negative with respect to pressure (Figure 1.1) [4]. However, at higher pressures, volume V has a more pronounced effect on Gibbs free energy; in order to minimize the energy of the system, volume must also decrease, and the equilibrium shifts towards phases that occupy less space [2]. This implies that there must be some form or forms of ice that are denser than both the liquid and ice Ih.

Indeed, multiple high-pressure, higher density phases of ice were discovered at the be-

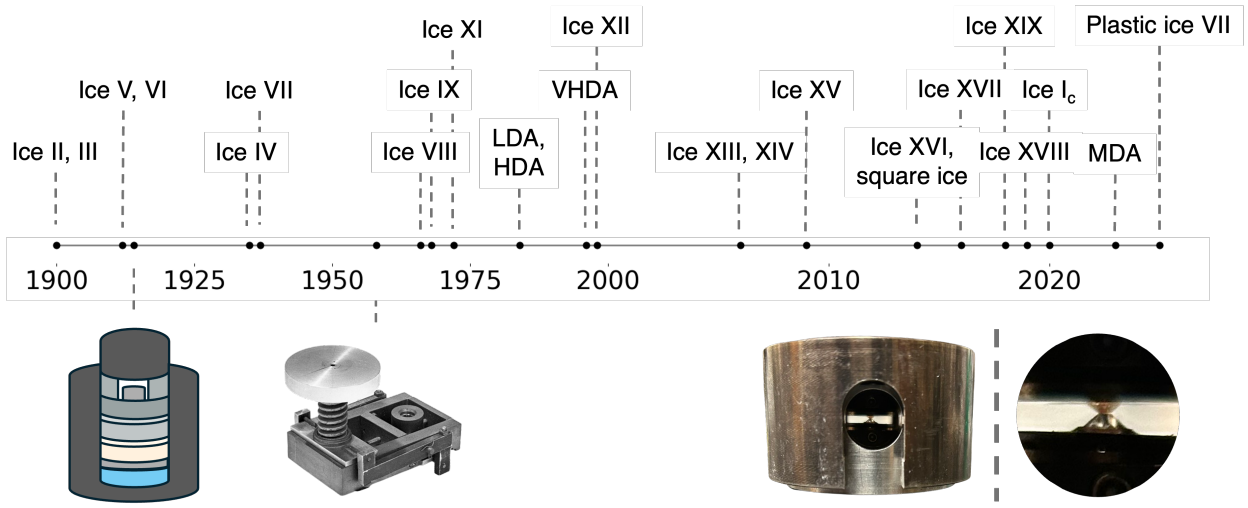

Figure 1.2: A timeline tracking the discovery of both crystalline and low-, medium-, high-, and very high-density amorphous (xDA, respectively) ices (above) coincident with the development of high-pressure equipments (below) [7–29]. Amorphous ices are less arranged compared to the other solid phases, and exist somewhere between a glassy, almost liquid-like state and a significantly disordered crystal [30]. Ice X is notably absent from the timeline, as its formation is still contested despite numerous efforts, the most recent being in 2022 [31]. From left to right: a diagram of Bridgman's seal and pictures of the original DAC—courtesy of the National Institute of Standards and Technology (NIST) museum—and a present-day BX90 DAC.

ginning of the 20th century. Between Tammann (1903) and Bridgman (1912, 1937), five stable ice polymorphs were identified up to 4 GPa [7–9]. Bridgman, "the father of modern high-pressure physics," was the first to account for systematic changes in volume at pressure [2]. His measurements—using a piston by which pressure is produced and simultaneously monitored—are still in agreement with the phase diagram for water (Figure 1.1) [5].

Today, there are 20 known crystalline and four amorphous forms of ice (July 2025). The invention of the diamond anvil cell (DAC) allowed for the formation and characterization of many of these ices (Figure 1.2) [10]. Ices are classified based on Bridgman's original nomenclature, using Roman numerals that track the discovery of each phase in increasing chronological order [8]. While the stability and structure of these phases are varied, most high-pressure forms tend to follow "ice rules" [32]. That is, interactions between water molecules in the bulk phase require tetrahedral coordination of hydrogen bonds, regardless

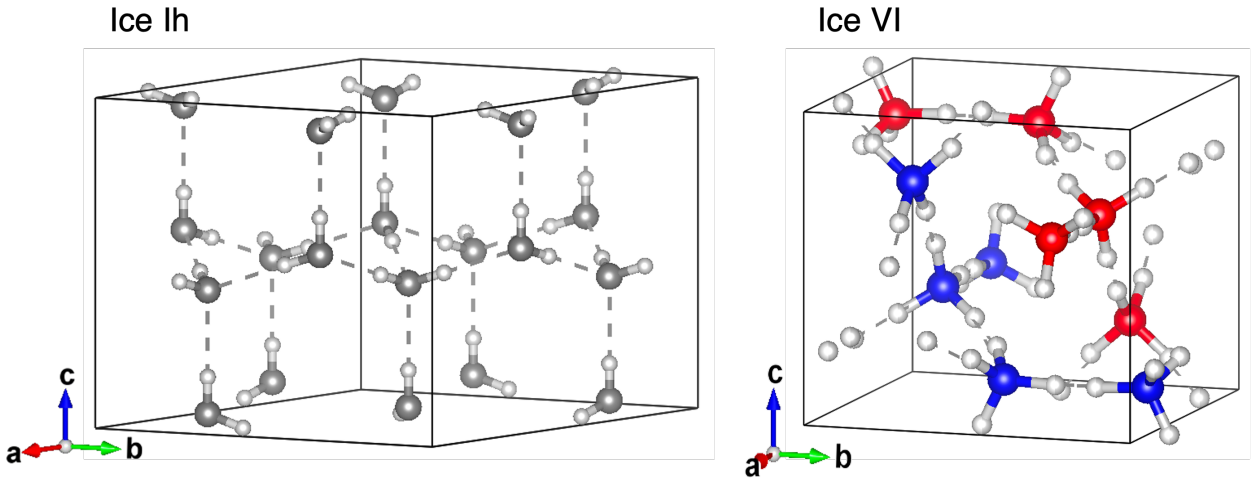

Figure 1.3: Left: the crystal structure of hexagonal ice Ih ($P6_3/mmc$) [32]. Oxygen and hydrogen sites are colored gray and white, respectively. Right: the crystal structure of tetragonal ice VI ($P4_2/nmc$) [33]. Ice VI is a self-clathrate; interpenetrating networks of H-bonded water molecules are colored blue and red. Both of these structures are proton disordered, following the ice rules.

of proton order or disorder. There are some trends common to the ices included in the phase diagram of Figure 1.1. Namely, as pressure increases along an isotherm, ice crystals are compressed, reducing interatomic distance and increasing density—both within a single phase and when transitioning to other polymorphs—in agreement with (1.1). A side-by-side comparison of the crystal structures of two of these ices, ice Ih and ice VI, is provided with Figure 1.3. Compared to hexagonal ice Ih, ice VI has a tetragonal crystal structure containing 10 water molecules per unit cell. Ice VI can be isolated at just below one GPa while at room temperature, and thus is relatively easy to access for high-pressure experiments. And while most exotic phases of ice have only been observed in the laboratory setting, ice VI has been found within inclusions of naturally-occurring cuboid diamond [34]. The search for new ices is ongoing, recently via the milling of medium-density amorphous ice and the trapping of plastic-like ice VII [28, 29]. As the catalog of high-pressure ices grows, so too does an understanding of the behavior of materials under extreme conditions.

1.2 Applications of High-pressure Chemistry

The chemical field's fascination with water is just one of the many ways by which high-pressure research influences the scientific community. Studies on pressure-effects include the behavior of geo- and biochemical systems, the structure of materials, and the advantage of synthetic processes at unique conditions. For example:

- High-pressure laser heating of calcium carbonate in the presence of carbon dioxide produces an anhydrous, mixed pyrocarbonate, likely stable in Earth's transition zone as part of the deep carbon cycle (Figure 1.4, a) [35].

- Bacteria *S. oneidensis* MR-1 and *E. coli* retain metabolic activity at pressure when trapped within intercrystalline liquid versus ice VI (Figure 1.4, b) [36].

- Pressurization of $CsPbBr_3$ leads to transitions in crystal structure, with direct implications on band gap and optoelectronic properties (Figure 1.4, c) [37].

- Alkali halides used as inert, pressure-transmitting media demonstrate a surprising reactivity with some rare-earth metals at very high pressures and temperatures exceeding 2000 K (Figure 1.4, d) [38].

More broadly, high-pressure experimentation is a versatile and ingenious tool that is central to advancements in condensed matter research, novel materials, and planetary and Earth and space sciences. Despite pressure being a fundamental thermodynamic parameter, our understanding of chemistry was—until recently—historically limited to studies carried out at or close to atmospheric conditions. Now, chemists can navigate regimes otherwise constrained to inaccessible, physical locations common throughout the Universe, e.g., deep within the interiors of planets and celestial bodies, by equipment that fit in the palm of their hand.

Reactivity and the chemical behavior of materials is governed in part by the arrangement of atomic orbitals and valence electrons. These can be controlled by environmental

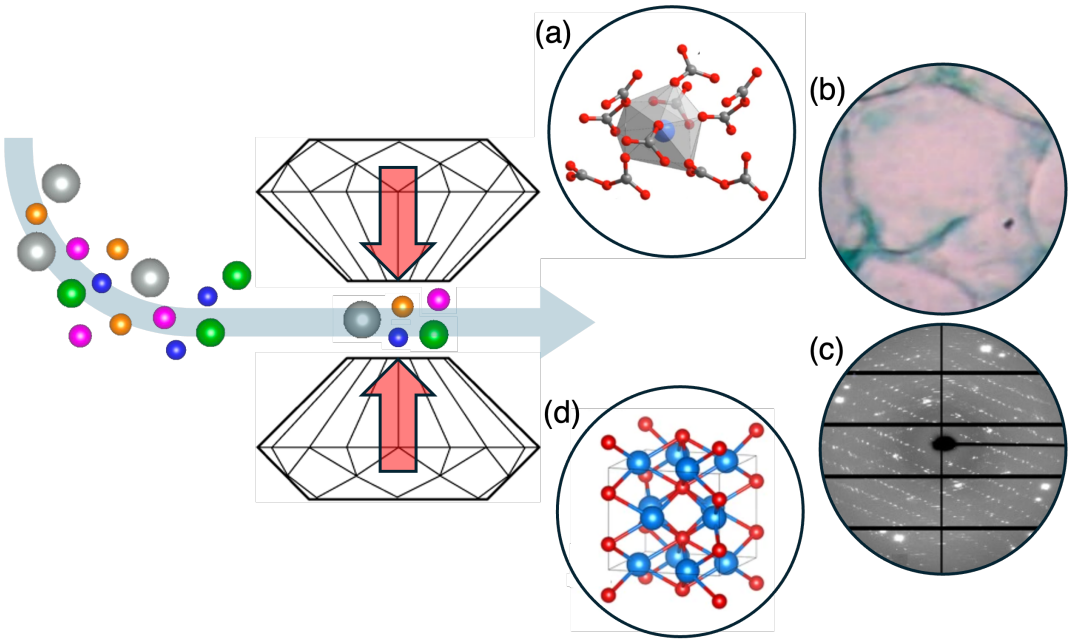

Figure 1.4: Examples of high-pressure chemistry, adapted. (a): Coordination of a Ca^{2+} ion in $Ca_3[C_2O_5]_2[CO_3]$ [35]. (b): Active *E. coli* between ice VI crystals at 1400 MPa [36]. (c): Merged diffraction image of $CsPbBr_3$ at 2.08 GPa [37]. (d): Y_2Cl crystal structure at about 41 GPa [38].

parameters like temperature and pressure. In fact, at very high pressures approaching 100 GPa, the molar volume and interatomic distances of most solid and liquid substances is at least halved [39]. This affects the energetic favorability of even the most stable states of matter. Through pressure-induced phase transitions alone, like the ones for water in the previous section, graphite can be converted to diamond—a widely known, consumer-forward process responsible for over half of the diamonds set in engagement rings in 2024 [40]. Creation of synthetic diamond via high-pressure high-temperature and chemical vapor deposition techniques also permits fine control of defects, making engineered diamonds useful for biological sensing, imaging of magnetic fields, and next-generation communication and quantum computing technologies [41]. Electronic overlap of atoms due to extreme pressures even introduces metallic character to elements like silicon ($\sim$ 10 to 12 GPa), iodine ($\sim$ 20 GPa), sulfur ($\sim$ 72 GPa), and oxygen ($\sim$ 100 GPa) [42, 43]. Efforts into isolating metallic hydrogen—assumed to exist above 400 GPa and considered a primary constituent of Jupiter

and other Jovian worlds—are ongoing and highly disputed since Ginzburg famously posed the problem in 1971 [44–46].

Along with the metallization of substances, the search for superconductivity has and continues to be an emergent, high-impact area in chemistry and material science. Many of the same elements discussed above have been documented to exhibit superconductive properties, i.e., electrical conductivity without energy loss at a specified temperature, at equivalent or higher pressures [43]. Unfavorable stoichiometries at atmospheric conditions can also be stabilized by gigapascal-level pressures [47]. For instance, transition metal nitrides like Zr_3N_4 and Hf_3N_4, containing 3d and 4d electrons, behave as metals instead of insulators with high hardness and superconducting behavior [48]. Famously, hydrogen sulfide (H_2S) displays superconductivity at 203 K when compressed to approximately 90 GPa. This is the highest recorded temperature for a superconductor to date—albeit still 90 degrees below room temperature—and is attributed to the novel stoichiometry H_3S produced via the pressure-induced decomposition of H_2S [49]. Unrelated to the hunt for superconductors, but interesting nonetheless, are the number of stable sodium chloride compounds that violate chemical intuition ($NaCl_3$, Na_3Cl, Na_2Cl, Na_3Cl_2, and $NaCl_7$) between 20 and 142 GPa [50].

Phase stability, particularly at high pressures, has implications on other systems beyond the observation of unusual and rare materials. The limit of stability for liquid and aqueous chemical mixtures is traditionally defined by the eutectic—the lowest temperature at which the liquid is at equilibrium. Most investigations into liquid-solid phase equilibria, and classically for binary solutions of salts in water, are focused on the relationship between melting temperatures and concentrations of dissolved compounds at ambient pressures. At high pressures, the solubility and stability of materials changes. In the case of aqueous magnesium sulfate ($MgSO_4$), its solubility limit dramatically increases with pressure while at room temperature; though, the high pressure eutectic is at a lower concentration (roughly 14 wt% $MgSO_4$ at 2 GPa) for ice VI as compared to ambient pressure and low temperature conditions (roughly 17 wt% $MgSO_4$ at 269 K) for ice Ih [51]. Recently, the absolute limit of liquid stability for aqueous systems was discovered and defined as the cenotectic by Zarriz,

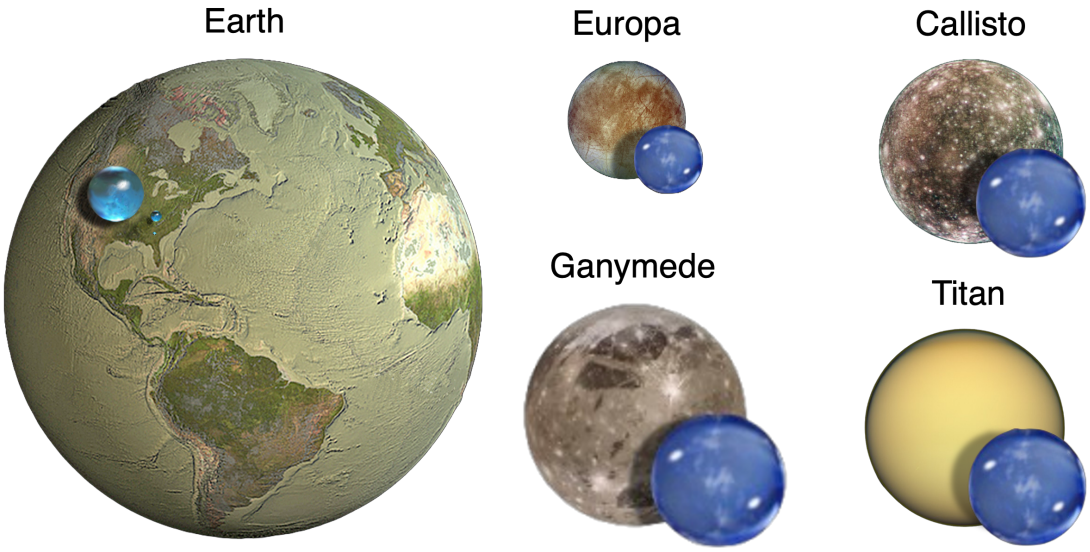

Figure 1.5: A depiction of Earth and select icy moons. Bodies and hydrospheres (blue) are to scale. Titan, Ganymede, and Callisto are about 35% water by weight and contain > 10x the amount of water on Earth. Europa is about 10% water by weight with > 2x the amount of water on Earth. Images: NASA/JPL/DLR. Adapted from Journaux.

Journaux, and Powell-Palm (2024) [52]. This is a new thermodynamic invariant point that describes the lowest temperature for liquid equilibria at any combination of pressures and concentrations of solutes. These parameters are pertinent to the expected composition of the large, ice-covered ocean worlds of the outer solar system, and influence the circulation of nutrient-rich fluids, the creation of brines and mushy layers within ice crusts, and the potential habitability of ice and ocean adjacent environments that are of interest to the in-progress and planned space flight missions of the upcoming decade [52].

1.3 Icy Ocean Worlds

High-pressure chemistry is essential to inform the exploration of terrestrial and extraterrestrial environments. Many moons of the outer solar system contain liquid water fractions significantly greater than that of Earth (Figure 1.5). The interior structures of Titan, Ganymede, and Callisto are expected to contain large subsurface oceans sandwiched beneath

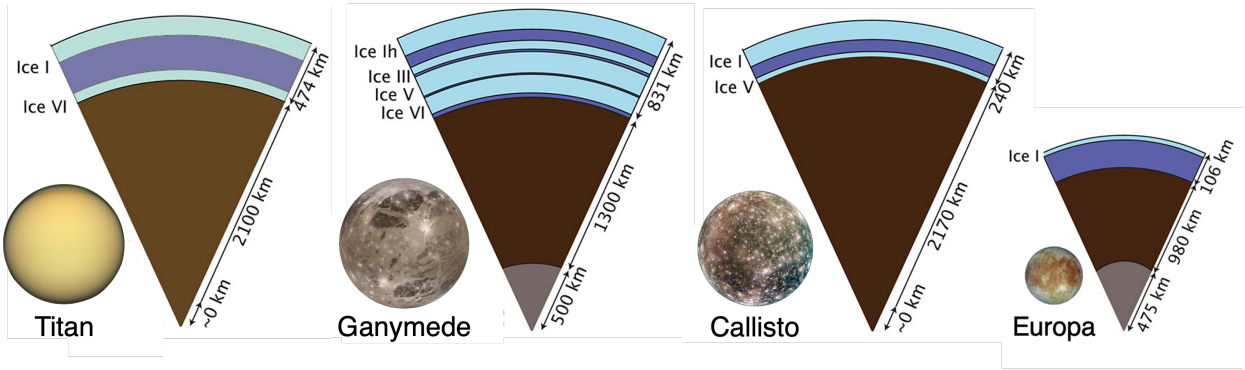

Figure 1.6: Interior structures of select icy moons with subsurface oceans. These are dependent on the radial profiles presented in Vance et al. (2018) with qualifications from Journaux et al. (2020) [53–55]. In particular, the structure of Ganymede assumes transport of minerals between high-pressure ices; otherwise, there are no stable liquid layers between ices III, V, and VI. For Europa, if the hydrosphere exceeds a thickness of 165 km, ice III may also appear at the bottom [56]. Adapted from Vance et al. (2018) [54].

an upper crust of ice Ih and one or more lower layers of high-pressure ices (Figure 1.6) [53, 54]. The chemical composition of the hydrospheres of these worlds is a salient topic in planetary science and astrobiology. In addition to organics like ammonia and methanol, a combination of salts such as NaCl, $MgSO_4$, Na_2SO_4, and $MgCl_2$ have been detected at the surface and are expected to be also present in deep reservoirs [53, 57, 58]. Assuming the transport of salts from nutrient-rich core to ocean layer, celestial, icy worlds may satisfy the prerequisite conditions to host putative, extant life [59, 60].

Some icy worlds will be explored over the next decade by ambitious, robotic space missions. These include the National Aeronautics and Space Administration's (NASA) Europa Clipper and Dragonfly missions, which will collect data quantifying the habitability of these worlds. In particular, the Clipper will concretely determine Europa's makeup and verify the existence of a subsurface ocean [61]. Over the course of nearly 50 unique flybys around Europa—some as close to 25 kilometers to its surface—the Clipper will scan almost the entire area of the moon. It is the largest spacecraft ever developed and successfully launched for an orbital mission, and should arrive to the Jovian system in 2030. It has nine instruments that

will collect data through a variety of imaging approaches (both spectral and spatial) and *in situ* analytical techniques. These will be able to distinguish between fresh and saline water ices, endogenic and exogenic inorganic and organic materials, and plumes that may provide information about active, subsurface chemical processes [62]. Likewise, the Dragonfly will assess the prebiotic conditions on Titan and the prevalence of interior and exterior biosignatures [63]. The rotorcraft will be able to land on Titan. Among other capabilities, Dragonfly will detect surface and atmospheric molecules (of masses up to 2000 Daltons), quantify bulk subsurface elemental composition, measure almost a dozen geophysical and meteorological properties, and image both samples and the surrounding environment. About once every two days on Titan—about once a month in Earth time—the rotorcraft will fly between planned landing sites. The Dragonfly mission is expected to launch in mid-2028 and arrive to Saturn's moon in the mid-2030s [63]. Anticipating the behavior of and analyzing the potential materials within Europa, Titan, and other icy worlds is of utmost importance. High-pressure chemistry is uniquely positioned to assist these efforts.

Biosignature detection is primarily informed by observations of biological and chemical markers specific to life on Earth, how necessary these features are for the survival of organisms, and how easily their characteristics can be identified and differentiated by techniques pertinent to planned fly-by, orbital, and lander architectures [64, 65]. Both the Europa Clipper and Dragonfly missions will use mass spectrometry (impact ionization and laser desorption, respectively) to analyze a wide range of simple and complex organics, providing vital information on the detailed, chemical structure of materials ejected from or present on icy worlds. A concern of biosignature detection is the stability of such materials; chemical degradation can occur under a variety of environmental pathways once the metabolic products or building blocks of organisms are no longer held at equilibrium [64]. In this instance, exposure of putative biosignatures to high pressures—one of the many types of adverse environmental parameters—may help assess their lifetime and identify unique degradation products, reducing ambiguity. Still, there are further advantages to high-pressure experimentation not previously outlined by well-accepted biosignature frameworks. If putative life is expected to

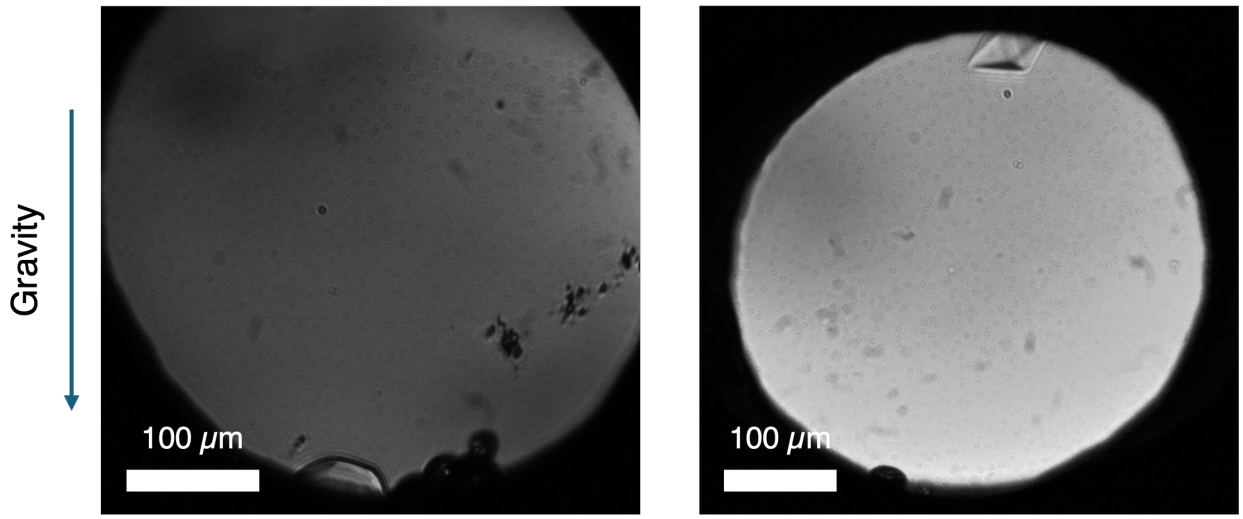

Figure 1.7: Images of single crystals of ice VI in equilibrium with the liquid and residing along the high-pressure melting curves of the $MgSO_4$-H_2O binary. Depending on the concentration of $MgSO_4$, ice VI is more dense (left) or less dense (right) than the liquid. Sample concentrations are about about 1.3 mol/kg and or 2.2 mol/kg, respectively. Scale bars are 100 µm.

exist beneath the surface of icy worlds, it must experience and be able to tolerate pressures significantly higher than those common to ecosystems on Earth, demanding adaptions that can be predicted and identified via novel, high-pressure methodologies. Materials that remain active at high pressure and are directly linked to the known chemical and biological functions of organisms should be considered.

Knowledge of icy, ocean worlds can also be supplanted by the consideration of solutes and the affect they might have on presumed internal structure. In Figure 1.6, the given interior of Ganymede is a prime example. As previously mentioned, the solubility of inorganic salts like $MgSO_4$ can increase significantly with pressure—so much so, in fact, that the density of the highly concentrated, briny solutions exceeds that of the preferential high-pressure ice polymorph (Figure 1.7). Magnesium sulfate is expected to be a major component of the hydrosphere of Ganymede, containing an ocean of up to 10 wt% $MgSO_4$ [66]. If the concentration of $MgSO_4$ is sufficiently high as to promote density inversion (Figure 1.7)—salt ions are not expected to incorporate into the lattices of ice VI and lower pressure polymorphs—

the creation of stable, briny regimes between layers of high-pressure ices on Ganymede is plausible [53, 67, 68]. Additionally, salts can play a major role in determining the stability of ices at different pressures and temperatures. If their concentrations exceeds that of the eutectic boundary, salt-hydrates will form instead of ice [51]. Combinations of salts and other organic solutes are expected on icy, ocean worlds; yet, the majority of the modeling of their interiors relies on the phase diagram of pure water rather than those specific to salt-water binaries, ternary systems, and so on [69]. This emphasizes the need for further determinations of aqueous salt equilibria at the pressures, temperatures, and concentrations applicable to the hydrospheres of icy worlds.

As of now, the Europa Clipper is already en route and the Dragonfly mission is proceeding on schedule. There remains a limited amount of time to broaden our understanding of the features of icy worlds and the biosignatures they may contain before these mission collect new and exciting data. By identifying more materials of interest in the search for life elsewhere in the Universe, libraries of potential biosignatures can be expanded and traits common among them can be elucidated via mission-relevant analytical techniques. Similarly, by observing the behavior of fundamental aqueous systems at unique thermodynamic conditions, current models of icy worlds can be improved and future geophysical data can be better interpreted. High-pressure chemistry provides the means to do both.

1.4 Mission Statement

In this dissertation, two works are presented. The first is a novel examination of ice-binding activity at high pressure. It shows not only that oligopeptides can function under extreme conditions—contrary to their design—but also that similar materials may constitute a new class of biosignature relevant to the exploration of icy worlds. The second is a mapping of melting curves at pressure for ice Ih and ice VI in the presence of inorganic salt ions. These findings expand upon the known melting curve of pure water and quantify concentrations at which binary salt systems are ideal. The metrological relevance of these works is also assessed.

References

1. Nellis, W. J. in *Ultracondensed Matter by Dynamic Compression* 63–78 (Cambridge University Press, 2017).
2. Fletcher, N. H. *The Chemical Physics of Ice* (Cambridge University Press, 1970).
3. Gibbs, J. W. On the equilibrium of heterogeneous substances. *Am. J. Sci.* **s3-16,** 441–458 (1878).
4. Atkins, P. W., De Paula, J. & Keeler, J. *Atkins' Physical Chemistry* (Oxford University Press, 2018).
5. Journaux, B. *et al.* Holistic Approach for Studying Planetary Hydrospheres: Gibbs Representation of Ices Thermodynamics, Elasticity, and the Water Phase Diagram to 2,300 MPa. *J. Geophys. Res. E: Planets* **125,** e2019JE006176 (2020).
6. Kamb, B. Structure of Ice VI. *Science* **150,** 205–209 (1965).
7. Tammann, G. *Kristallisieren und Schmelzen - Ein Beitrag zur Lehre der Änderungen des Aggregatzustandes* (Barth/Leipzig, 1903).
8. Bridgman, P. W. Water, in the Liquid and Five Solid Forms, under Pressure. *Proc. Am. Ac. A. Sc.* **47,** 441–558 (1912).
9. Bridgman, P. W. The Phase Diagram of Water to 45,000 kg/cm2. *J. Chem. Phys.* **5,** 964–966 (1937).
10. Piermarini, G. & Block, S. in *A Century of Excellence in Measurements, Standards, and Technology: A Chronicle of Selected NBS/NIST Publications, 1901-2000* (National Institute of Standards and Technology, 2001).
11. Bridgman, P. W. The Technique of High Pressure Experimenting. *Proc. Am. Ac. A. Sc.* **49,** 627–643 (1914).
12. Bridgman, P. W. The Pressure-Volume-Temperature Relations of the Liquid, and the Phase Diagram of Heavy Water. *J. Chem. Phys.* **3,** 597–605 (1935).

13. Whalley, E., Davidson, D. W. & Heath, J. B. R. Dielectric Properties of Ice VII. Ice VIII: A New Phase of Ice. *J. Chem. Phys.* **45,** 3976–3982 (1966).

14. Whalley, E., Heath, J. B. R. & Davidson, D. W. Ice IX: An Antiferroelectric Phase Related to Ice III. *J. Chem. Phys.* **48,** 2362–2370 (1968).

15. Shuji, K. Dielectric Dispersion and Phase Transition of KOH Doped Ice. *J. Phys. Soc. Jpn.* **32,** 1442–1442 (1972).

16. Mishima, O., Calvert, L. D. & Whalley, E. 'Melting ice' I at 77 K and 10 kbar: a new method of making amorphous solids. *Nature* **310,** 393–395 (1984).

17. Mishima, O. Relationship between melting and amorphization of ice. *Nature* **384,** 546–549 (1996).

18. Lobban, C., Finney, J. L. & Kuhs, W. F. The structure of a new phase of ice. *Nature* **391,** 268–270 (1998).

19. Salzmann, C. G., Radaelli, P. G., Hallbrucker, A., Mayer, E. & Finney, J. L. The Preparation and Structures of Hydrogen Ordered Phases of Ice. *Science* **311,** 1758–1761 (2006).

20. Salzmann, C. G., Radaelli, P. G., Mayer, E. & Finney, J. L. Ice XV: A New Thermodynamically Stable Phase of Ice. *Phys. Rev. Lett.* **103,** 105701 (2009).

21. Kantor, I. *et al.* BX90: A new diamond anvil cell design for X-ray diffraction and optical measurements. *Rev. Sci. Instrum.* **83,** 125102 (2012).

22. Falenty, A., Hansen, T. C. & Kuhs, W. F. Formation and properties of ice XVI obtained by emptying a type sII clathrate hydrate. *Nature* **516,** 231–233 (2014).

23. Algara-Siller, G. *et al.* Square ice in graphene nanocapillaries. *Nature* **519,** 443–445 (2015).

24. Del Rosso, L., Celli, M. & Ulivi, L. New porous water ice metastable at atmospheric pressure obtained by emptying a hydrogen-filled ice. *Nat. Commun.* **7,** 13394 (2016).

25. Gasser, T. M. *et al.* Experiments indicating a second hydrogen ordered phase of ice VI. *Chem. Sci.* **9,** 4224–4234 (2018).

26. Millot, M. *et al.* Nanosecond X-ray diffraction of shock-compressed superionic water ice. *Nature* **569,** 251–255 (2019).

27. Salzmann, C. G. & Murray, B. J. Ice goes fully cubic. *Nat. Mater.* **19,** 586–587 (2020).

28. Rosu-Finsen, A. *et al.* Medium-density amorphous ice. *Science* **379,** 474–478 (2023).

29. Rescigno, M. *et al.* Observation of plastic ice VII by quasi-elastic neutron scattering. *Nature* **640,** 662–667 (2025).

30. Davies, M. B., Rosu-Finsen, A., Salzmann, C. G. & Michaelides, A. Low-density amorphous ice contains crystalline ice grains. *Phys. Rev. B* **112,** 024203 (2025).

31. Grande, Z. M. *et al.* Pressure-driven symmetry transitions in dense H_2O ice. *Phys. Rev. B* **105,** 104109 (2022).

32. Bernal, J. D. & Fowler, R. H. A Theory of Water and Ionic Solution, with Particular Reference to Hydrogen and Hydroxyl Ions. *J. Chem. Phys.* **1,** 515–548 (1933).

33. Kuhs, W. F., Finney, J. L., Vettier, C. & Bliss, D. V. Structure and hydrogen ordering in ices VI, VII, and VIII by neutron powder diffraction. *J. Chem. Phys.* **81,** 3612–3623 (1984).

34. Kagi, H. *et al.* Evidence for ice VI as an inclusion in cuboid diamonds from high P-T near infrared spectroscopy. *Mineral. Mag.* **64,** 1089–1097 (2000).

35. Spahr, D. *et al.* $Ca_3[C_2O_5]_2[CO_3]$ is a pyrocarbonate which can be formed at p, T-conditions prevalent in the Earth's transition zone. *Commun. Chem.* **7,** 238 (2024).

36. Sharma, A. *et al.* Microbial Activity at Gigapascal Pressures. *Science* **295,** 1514–1516 (2002).

37. Zhang, D. *et al.* Pressure induced structural and electronic band transition in $CsPbBr_3$. *Commun. Chem.* **7,** 175 (2024).

38. Yin, Y. *et al.* Synthesis of rare-earth metal compounds through enhanced reactivity of alkali halides at high pressures. *Commun. Chem.* **5,** 122 (2022).

39. McMillan, P. F. Chemistry at high pressure. *Chem. Soc. Rev.* **35,** 855–857 (2006).

40. Friesen, G. *Lab-Grown Diamonds Boom: Is It Game Over For Mined Diamonds?* [Online; accessed 23-July-2025]. 2025.

41. Savage, N. Quantum diamond sensors. *Nature* **591,** S37–S37 (2021).

42. Ahrens, T. J. Elements, Oxides, Silicates: High Pressure Phases With Implications for the Earth's Interior. *Eos Trans. AGU* **69,** 964–964 (1988).

43. Amaya, K., Shimizu, K. & Eremets, M. I. Search for Superconductivity under Ultrahigh Pressure. *Int. J. Mod. Phys. B* **13,** 3623–3625 (1999).

44. Wigner, E. & Huntington, H. B. On the Possibility of a Metallic Modification of Hydrogen. *J. Chem. Phys.* **3** (1935).

45. Ginzburg, V. L. What problems of physics and astrophysics seem now to be especially important and interesting (thirty years later, already on the verge of XXI century)? *Phys. Usp.* **42,** 353–373 (1999).

46. Gregoryanz, E. *et al.* Everything you always wanted to know about metallic hydrogen but were afraid to ask. *Matter Radiat. Extremes* **5,** 038101 (2020).

47. Zhang, L., Wang, Y., Lv, J. & Ma, Y. Materials discovery at high pressures. *Nat. Rev. Mater.* **2,** 17005 (2017).

48. Zerr, A. *et al.* Recent Advances in New Hard High-Pressure Nitrides. *Adv. Mater.* **18,** 2933–2948 (2006).

49. Drozdov, A. P., Eremets, M. I., Troyan, I. A., Ksenofontov, V. & Shylin, S. I. Conventional superconductivity at 203 kelvin at high pressures in the sulfur hydride system. *Nature* **525,** 73–76 (2015).

50. Zhang, W. *et al.* Unexpected Stable Stoichiometries of Sodium Chlorides. *Science* **342,** 1502–1505 (2013).

51. Nakamura, R. & Ohtani, E. The high-pressure phase relation of the $MgSO_4$–H_2O system and its implication for the internal structure of Ganymede. *Icarus* **211,** 648–654 (2011).

52. Zarriz, A., Journaux, B. & Powell-Palm, M. J. On the equilibrium limit of liquid stability in pressurized aqueous systems. *Nat. Commun.* **15,** 10666 (2024).

53. Journaux, B. *et al.* Large Ocean Worlds with High-Pressure Ices. *Space Sci. Rev.* **216,** 7 (2020).

54. Vance, S. D. *et al.* Geophysical Investigations of Habitability in Ice-Covered Ocean Worlds. *J. Geophys. Res. E: Planets* **123,** 180–205 (2018).

55. Néri, A., Guyot, F., Reynard, B. & Sotin, C. A carbonaceous chondrite and cometary origin for icy moons of Jupiter and Saturn. *Earth Planet. Sci. Lett.* **530,** 115920 (2020).

56. Kimura, J. Europa's structural conditions for the existence of subsurface ocean and the absence of metallic core-driven magnetic field. *Planet. Space Sci.* **243,** 105868 (2024).

57. Hibbitts, C. A., Stockstill-Cahill, K., B., W. & Paranicas, C. Color centers in salts - Evidence for the presence of sulfates on Europa. *Icarus* **326,** 37–47 (2019).

58. Trumbo, S. K., Brown, M. E. & Hand, K. P. Sodium chloride on the surface of Europa. *Sci. Adv.* **5,** eaaw7123 (2019).

59. Hernandez, J., Caracas, R. & Labrosse, S. Stability of high-temperature salty ice suggests electrolyte permeability in water-rich exoplanet icy mantles. *Nat. Commun.* **13,** 3303 (2022).

60. Journaux, B. Salty ice and the dilemma of ocean exoplanet habitability. *Nat. Commun.* **13,** 3304 (2022).

61. Asstd. Q&A Europa Clipper mission. *Nat. Commun.* **16,** 3837 (2025).

62. Becker, T. M. *et al.* Exploring the Composition of Europa with the Upcoming Europa Clipper Mission. *Space Sci. Rev.* **220,** 49 (2024).

63. Barnes, J. W. *et al.* Science Goals and Objectives for the Dragonfly Titan Rotorcraft Relocatable Lander. *Planet. Sci. J.* **2,** 130 (2021).

64. Neveu, M., Hays, L. E., Voytek, M. A., New, M. H. & Schulte, M. D. The Ladder of Life Detection. *Astrobiology* **18,** 1375–1402 (2018).

65. Green, J. *et al.* Call for a framework for reporting evidence for life beyond Earth. *Nature* **598,** 575–579 (2021).

66. Vance, S., Bouffard, M., Choukroun, M. & Sotin, C. Ganymede's internal structure including thermodynamics of magnesium sulfate oceans in contact with ice. *Planet. Space Sci.* **96,** 62–70 (2014).

67. Journaux, B. *et al.* Salt partitioning between water and high-pressure ices. Implication for the dynamics and habitability of icy moons and water-rich planetary bodies. *Earth Planet. Sci. Lett.* **463,** 36–47 (2017).

68. Vance, S. & Brown, M. J. Thermodynamic properties of aqueous $MgSO_4$ to 800 MPa at temperatures from -20 to 100 °C and concentrations to 2.5 molkg^{-1} from sound speeds, with applications to icy world oceans. *Geochim. Cosmochim. Acta* **110,** 176–189 (2013).

69. Journaux, B., Daniel, I., Caracas, R., Montagnac, G. & Cardon, H. Influence of NaCl on ice VI and ice VII melting curves up to 6 GPa, implications for large icy moons. *Icarus* **226,** 355–363 (2013).

Chapter 2
METHODOLOGY AND METROLOGY

There are a number of factors that contribute to the success of experiments at high pressure.[1] These can be split into two general categories: diamond anvil cell (DAC) and equipment design, and data collection and calibration. The relevance of each depends on experimental intent.

2.1 Diamond Anvil Cell and Equipment Design

Choice components of DACs and related equipment have a significant impact on experimental capabilities and findings. Nonetheless, the overall construction and underlying principles of DACs are consistent across their wide variety of design. A schematic of the core of a DAC is provided in Figure 2.1.

A DAC in its simplest form consists of two opposing diamond anvils. These anvils are supported so that their culets—the small, flat surface below the outer edge of the diamond at which its facets converge—are parallel and well-aligned [1]. A hollowed-out, metal gasket is pinched between the diamond culets in order to create a sample chamber. Materials of interest are added first, and then the remaining volume is filled with a pressure transmitting medium. A pressure sensor is also typically included inside the cell. Most common optical pressure gauges are ruby spheres (Al_2O_3:Cr^{3+}) containing a standard amount of chromium, diamond, quartz, samarium-doped yttrium aluminum garnet (Sm:YAG), and others. Section 2.1.2 describes these gauges in more detail.

In the scope of this work, analytical techniques coupled with DACs focus on optical microscopy and spectroscopy. When a cell is properly configured, ice grains can be well resolved,

[1]This chapter is the author's original work.

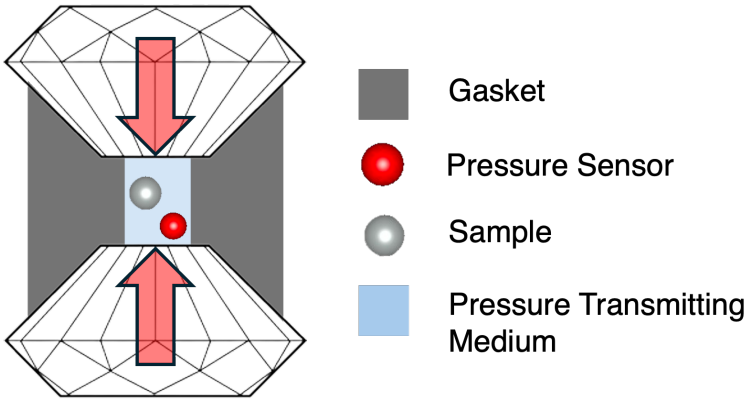

Figure 2.1: A representative schematic of the core of a diamond anvil cell. A sample, sensor, and pressure transmitting medium are trapped between a gasket and the culets of two opposing diamond anvils. This comprises the sample chamber. As the anvils are forced closer together, high uniform pressures are achieved within the sample chamber.

selected, and measured for size; Raman scattering in the visible region can be observed from single crystals; and high-intensity photoluminescence spectra can be collected from pressure sensors. More broadly, other techniques and applications include vibrational spectroscopy in the infrared, Brillouin scattering microscopy, x-ray diffraction and x-ray absorption spectroscopies, nuclear magnetic resonance, characterization of electrical and magnetic properties of materials, lifetime and sound speed studies, and more [2–10].

The operation of a DAC relies on the relationship:

$$p = \frac{F}{A} \tag{2.1}$$

where pressure p is defined as the magnitude of the normal force F applied perpendicular to the area A [11]. As the culet size of diamond anvils usually ranges from 100 µm to one mm, only a moderate amount of force is required to quickly reach pressures exceeding one GPa. For example, using 700 µm diameter culets, one GPa of pressure is achieved with about 385 newtons (N) of force; in perspective, this force is within the expected average grip strength for most young, male adults [12]. Diamond is an incredibly hard material with a compressive

yield strength of 130 to 140 GPa [13]. That, paired with a high optical transparency—extending from the ultraviolet (UV) to far infrared (IR) region—is why diamond is the preferred element for most high-pressure applications [14]. Scientists have even reached static pressures upwards of 600 GPa using DACs fitted with micro-semi-spheres that act as sources of additional pressure [15]. To reduce the risk of mechanical failure when running a high-pressure experiment inside of a DAC, the anvils remain in close alignment (including parallelism, see Figure 2.1), and the gasket material is chosen accordingly to resist the entire range of pressure and strain of the experiment.

2.1.1 Diamond Anvil Cell Preparation

Often, a high-pressure experiment starts with selecting the right parts for the job. These include: the diamond anvils, the gasket material, the chamber size, the pressure sensor, and the pressure transmitting medium. The individual components to build a DAC, and the gasket for the sample chamber, are shown in Figure 2.2 and Figure 2.3, respectively.

Diamonds are classified by type and prevalence of chemical impurity. Either metric influences the characteristic photoluminescence (PL) and IR spectra of diamond. The most common element trapped in naturally-occurring and man-made diamond is nitrogen, responsible for point defects and combination color centers at the atomic level [16]. Type Ia and Ib diamonds contain a relatively high concentration of nitrogen, upwards of 200 parts per million (ppm) [17]. Type IIa diamonds have almost near-undetectable levels of nitrogen by IR absorption spectroscopy [18]. Despite their exceptional purity, type IIa diamonds can still present intense peaks in the visible region. High-pressure high-temperature (HPHT) annealing of type IIa diamonds promotes lattice reconfiguration and the destruction of lingering defects [19].

Spectral features from diamond can drown out or obfuscate signals from samples at pressure. For water, the O-H stretching region of its Raman spectrum between 3000 and 3800 wavenumbers (cm^{-1}) is used to differentiate between phases of ice (see Section 2.1.3). Nitrogen-vacancy (NV) centers, a nearest-neighbor point defect consisting of a substitutional

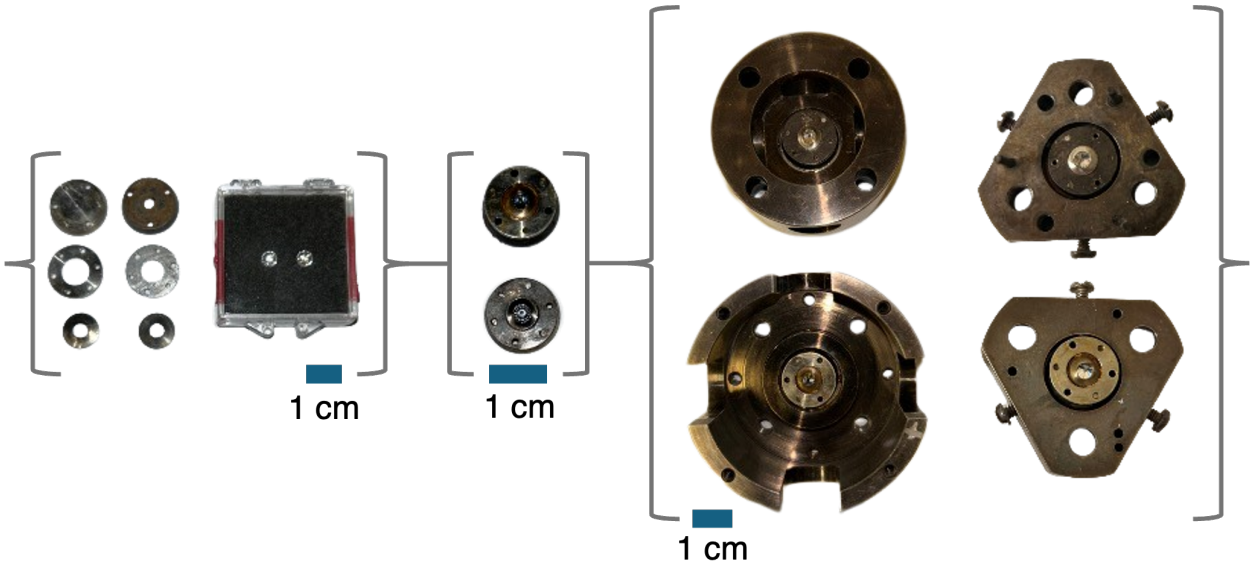

Figure 2.2: The assembly of a diamond anvil cell. From left to right: selection of diamond anvils and diamond supporting plates, the completed seats, and each half of a working cell. Two types of cells are pictured in the right-most bracket, a BX90 (left) and a MDAC (right). The scale bar (blue) for each grouping of parts is 1 cm.

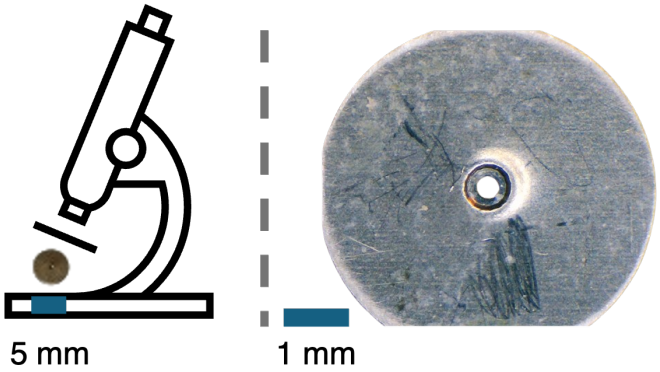

Figure 2.3: Left: a gasket for a diamond anvil cell, true to size. Right: the same gasket as viewed under a microscope. The gasket is 5 mm in diameter and 250 µm thick. At the center of the gasket are the depressed or dimpled area and the drilled sample chamber. Dimensions are 700 µm by 150 µm and 400 µm by 150 µm, respectively. This particular gasket is Inconel® 718. Scale bars (blue) are 5 mm and 1 mm, respectively.

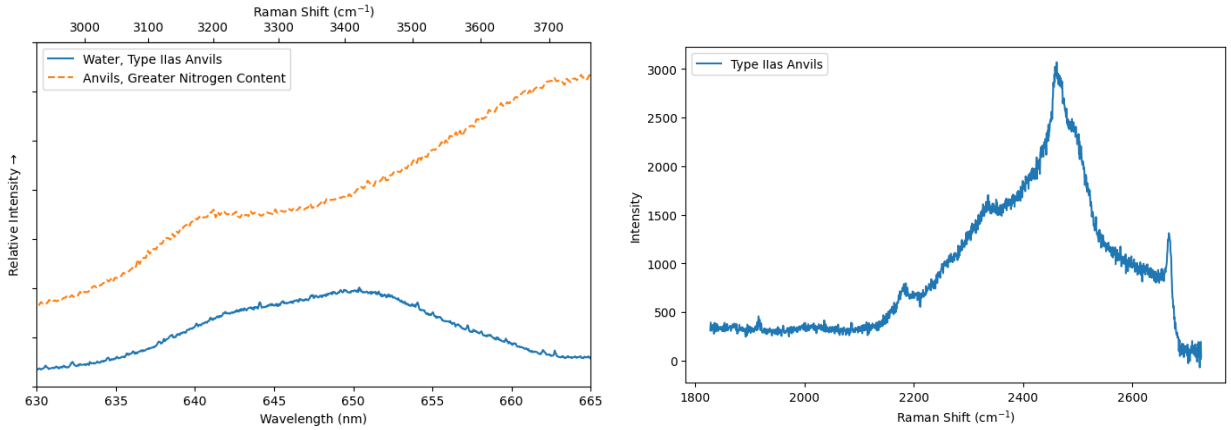

(a) (b)

Figure 2.4: Spectra of (a) liquid water O-H stretching Raman modes using type IIas anvils (blue) and negatively-charged NV center PL (orange) and (b) second-order diamond Raman scattering observed in the combination region of a 2 m solution of sodium sulfate. Features from diamond hide sample peaks of interest.

nitrogen atom and a lattice vacancy, have a strong PL signature that coincides with these Raman-active modes [20]. For this reason, it is recommended that type IIa diamonds with ultra-low Raman fluorescence and birefringence (type IIas, Almax easyLab) are selected as anvils for DAC work investigating the behavior of high-pressure ices (Figure 2.4, a). That being said, some spectral contribution from diamond anvils is unavoidable. For example, second-order diamond Raman scattering between 1800 and 2800 cm^{-1} overlaps with possible combination modes assigned to sodium sulfate decahydrate ($Na_2SO_4 \cdot 10H_2O$, mirabilite), metastable heptahydrate ($Na_2SO_4 \cdot 7H_2O$), and concentrated solutions of sodium sulfate [21]. Identification of these samples is better facilitated by observation of their lattice modes, internal sulfate modes, or internal water modes (Figure 2.4, b). Regardless, understanding viable sample characterization techniques and anticipating potential interference from diamond anvils is an important part of the high-pressure experimental method.

The exact dimensions of the DAC sample chamber should also be considered. Diamond anvil culet size, gasket material, and final sample chamber diameter and thickness are all

adjustable and interrelated parameters that control: (i) the pressures accessible during an experiment, and (ii) the behavior of samples at pressure. In general, as described by (2.1), the total area of the sample is inversely proportional to the pressure applied to the sample itself. In practice, this means that the pressure exerted on a sample can be modulated by culet, indentation of the gasket between the culets (dimpling), and drilling of the hole in the gasket, in that order.

The maximum pressure achieved during a high-pressure experiment is foremost limited by the failure of the diamond anvils themselves. Diamonds with flat culets (as pictured in Figure 2.1) are the simplest type of anvil and can withstand the least amount of strain, capped at about 100 GPa [22]. These pressures are well-above those relevant to the hydrospheres of icy worlds—the conditions of which provide the experimental framework for Chapters 3 and 4—so flat culets are appropriate for use here. The diameter of the culet further restricts the DAC pressure limit. Smaller culet diameters can reach higher pressures. A culet with a diameter of 350 µm is safe to use up to 50 GPa, whereas one with a 700 µm diameter should stay below 10 GPa [22]. Diamonds are an expensive laboratory resource, and careful thought should be put towards maximum pressure as an experimental parameter.

Likewise, gasket material, dimpling thickness, and drilled diameter are all tied to culet size. To prevent deformation of the gasket under pressure—which can lead to sample loss, uneven distribution of pressure, and damage to the diamond anvils—metals with a corresponding hardness are chosen. Rhenium and tungsten gaskets can tolerate extremely high pressures (> 40 GPa), whereas stainless steel or Inconel® alloy are sufficient for general use. Additionally, the risk of deformation is mitigated by dimpling the gasket to a thickness below 90 µm, and by drilling a hole generally between 30 and 60% of culet diameter (Figure 2.3). These dimensions shape the sample chamber. Proper gasket preparation is often the difference between running a complete experiment and having to scrap the gasket, dispose of valuable sample material, and dedicate hours to reconstructing the cell.

There is some extra nuance in experimental design based on sample chamber dimensions not explicitly related to pressure. Certainly, if the experiment is low-risk, selecting the

largest available dimensions makes sample loading and pressurization smoother. However, the behavior of materials—especially liquids like water—is at times dependent purely on sample chamber diameter and thickness. Some examples:

- Approximating the water filling the sample chamber as a single droplet, a diameter of 400 µm equates to somewhere between 15 and 35 degrees of potential supercooling [23]. This means that the liquid phase can remain relatively metastable either at temperatures below the freezing point for water or at pressures above the melting lines for high-pressure ices. Wider diameters reduce the degree of supercooling experienced by aqueous samples, easing the nucleation of high-pressure ice polymorphs.

- In Chapter 3, the growth of ice VI crystals is monitored over time to quantify the extent of ice recrystallization inhibition (IRI) activity of different biomolecules. If the sample chamber is too deep, multiple layers of ice can form simultaneously, blurring grain boundaries and complicating the quantification of grain growth via segmentation analysis (Figure 2.5, left). In this case, the gasket is dimpled to a thickness between 40 and 50 µm—thinner than the advised 10% lower limit. Preparation of extremely shallow gasket chambers risks damaging anvils and leads to more severe gasket deformation at equivalent pressures.

- In contrast, single crystals of ice Ih and ice VI are selected in Chapter 4 to map the previously undetermined melting curves of aqueous salt solutions at different concentrations. If the sample chamber is too shallow, ice grains will adhere to the top of the culet surface instead of maturing in equilibrium with the liquid (Figure 2.5, right). Materials stuck to the diamond anvil experience friction as a source of non-hydrostatic stress [24]. Gaskets are dimpled to a thickness greater than 20% of the culet diameter. While this causes gasket deformation at lower pressures—generally beginning at or around one GPa—gaskets can potentially be reused for multiple experiments if treated carefully.

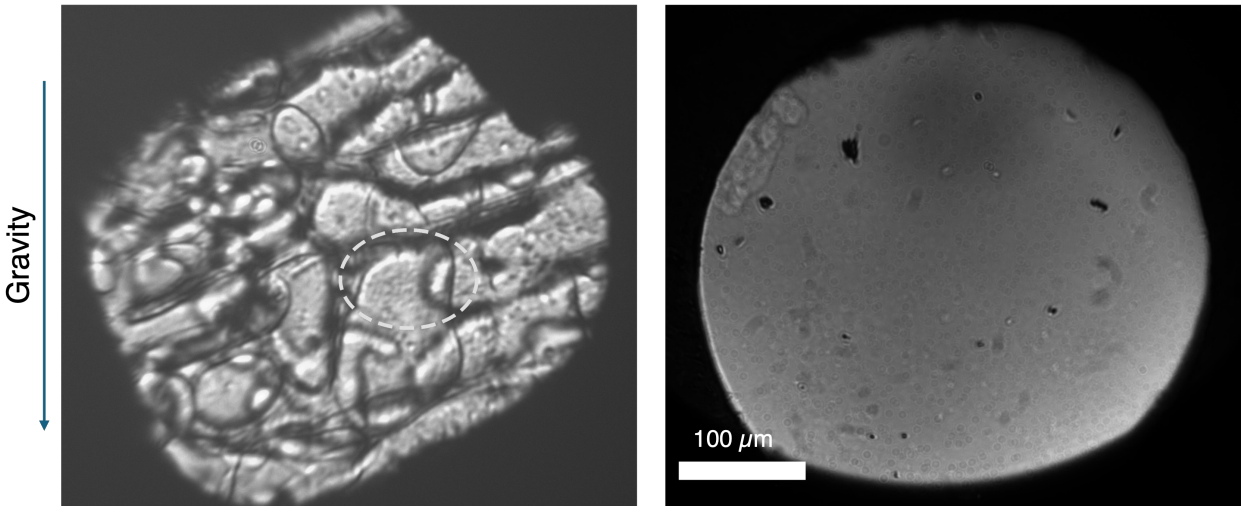

Figure 2.5: Micrographs of (left) the growth of ice VI using a 0.5 m NaCl with 1 mg/mL non-ice-binding peptide, where grains boundaries of ice at various depths are overlapping, and (right) ice VI stuck to the bottom culet surface in a metastable, saturated solution of $MgCl_2$, where the crystal does not grow or shrink with pressure in the typical manner (upper left of the sample chamber). Scale bar is 100 µm. The dashed oval in the left image is a marking for the laser spot of the optical system.

It falls to the user to determine the best sample chamber configuration for each experiment.

DACs have remained a popular tool in the study of materials at high pressure for more than 50 years. Consequently, there are several different types of DACs available to researchers today. Of these, two are presented in Figure 2.2, the Merrill-Bassett diamond anvil cell (MDAC) and the BX90 (an acronym for Brillouin scattering–x-ray diffraction with a 90° opening angle) [1, 25]. Both the MDAC and the BX90 rely on the manual tightening of screws to generate force. To ensure that diamonds remain aligned during an experiment, the MDAC has guiding rods for its plates to slide along, whereas the BX90 leverages a miniature, mechanically-fit piston and cylinder design. The guiding rods of the MDAC tend to stick and bend over time, so the BX90 is generally the more reliable cell. Either represents a major achievement in high-pressure instrumentation.

2.1.2 Pressure Sensors

Pressure sensors used in high-pressure experiments include ruby (Al_2O_3:Cr^{3+}), metals like copper, gold and platinum, minerals like quartz and diamond, and other synthetic materials like samarium-doped yttrium aluminum garnet (Sm:YAG). More specifically, the response of these sensors to pressure is treated as a gauge, i.e., ruby photoluminescence (PL) lines, lattice spacings of metals measured via x-ray diffraction (XRD), the IR spectra or Raman shift of minerals, and the optical fluorescence bands of other materials [26–33]. The most common pressure gauge at temperatures below 500 K is ruby. Its PL signal is intense, and calibrations are precise up to 2.5% of the measured pressure below 150 GPa. This precision can be improved for pressures at or below one GPa if the temperature is known to within ± 0.5 K [28]. It can also be refined to a similar margin by using the dual ruby method described hereafter. Other pressure gauges, especially those reliant upon XRD or IR, are limited by the accessibility of their technique and usually have larger uncertainties below a few GPa. These remain widely used due to their reliability and stability at higher pressures and temperatures. Raman of diamond anvils is a suitable secondary indicator of pressure, though it is considered less precise compared to the ruby gauge [34, 35], with pressure uncertainties around 100 MPa below one GPa.

The pressure dependence of ruby PL spectra was first identified in 1972 up to 2.2 GPa and later standardized for use as a gauge in 1978 up to 100 GPa [36, 37]. Prior to its discovery, pressures for DAC work were estimated by screw tightness with relatively little confidence (nearing ± 30%) [36]. Al_2O_3 is chemically inert and thus a choice material for pressure sensing. The shift of R1 lines was matched to changes in volume for transition metals based on their equations of state [37]. The resulting empirical function—an exponential in two variables that assumes the partial derivative of pressure with respect to the R1 line is linear—is still widely used today (with some modifications) and given below. The pressure

determined via the fluorescence doublet of Cr^{3+}-doped ruby spheres is:

$$P_{(Mbar)} = A * B[(1 + \frac{\Delta\lambda}{\lambda_0})^B - 1]^{-1} \tag{2.2}$$

where A and B are 19.04 and 7.665 megabar (Mbar), respectively, and λ is the wavelength of the ruby R1 line [26]. The coefficients A and B depend on the published calibration; the numbers above are according to Piermarini et al. (1975) and Mao et al. (1986) [26, 38]. At ambient temperatures and pressure, the literature value for the R1 line is near 694.25 nm [28]. This value varies slightly, dependent on the exact Cr^{3+} composition and the manufacturing techniques (e.g. amount of annealing, etc.) of the ruby spheres, so it is imperative to measure for a given batch. If temperature changes, λ_0 changes and should be either corrected or internally-referenced. Because of this temperature dependency, a low laser power must be used in order to prevent heating the ruby sphere when collecting data. To limit uncertainties related to temperature fluctuations, the easiest and most consistent way to determine pressure in externally heated or cooled DAC experiments is the dual ruby method, where at least one is included inside the sample chamber and another outside the DAC on the backside of an anvil. This way, the outer ruby in contact with the diamond anvil provides an *in situ* measurement of λ_0 at the same temperature as the ruby under pressure, since diamond has one of the highest known thermal conductivities for materials. An example of a pressure determination using the ruby gauge is shown in Figure 2.6.

The pressure determined via the Raman spectra of diamond anvils is:

$$P_{(GPa)} \cong K_0 \frac{\Delta\nu}{\nu_0}[1 + \frac{1}{2}(K_0' - 1)\frac{\Delta\nu}{\nu_0}] \tag{2.3}$$

where K_0 is the bulk modulus, K_0' is its pressure derivative, and $\Delta\nu/\nu_0$ is the relative Raman frequency change of the first-order diamond anvil mode [32]. The values for K_0 and K_0' using a hydrostatic pressure transmitting medium are 445 ± 20 GPa and 3.5 ± 0.5 GPa, respectively [39]. The edge frequency ν_0 is defined as 1334 ± 1 cm^{-1} at ambient pressure;

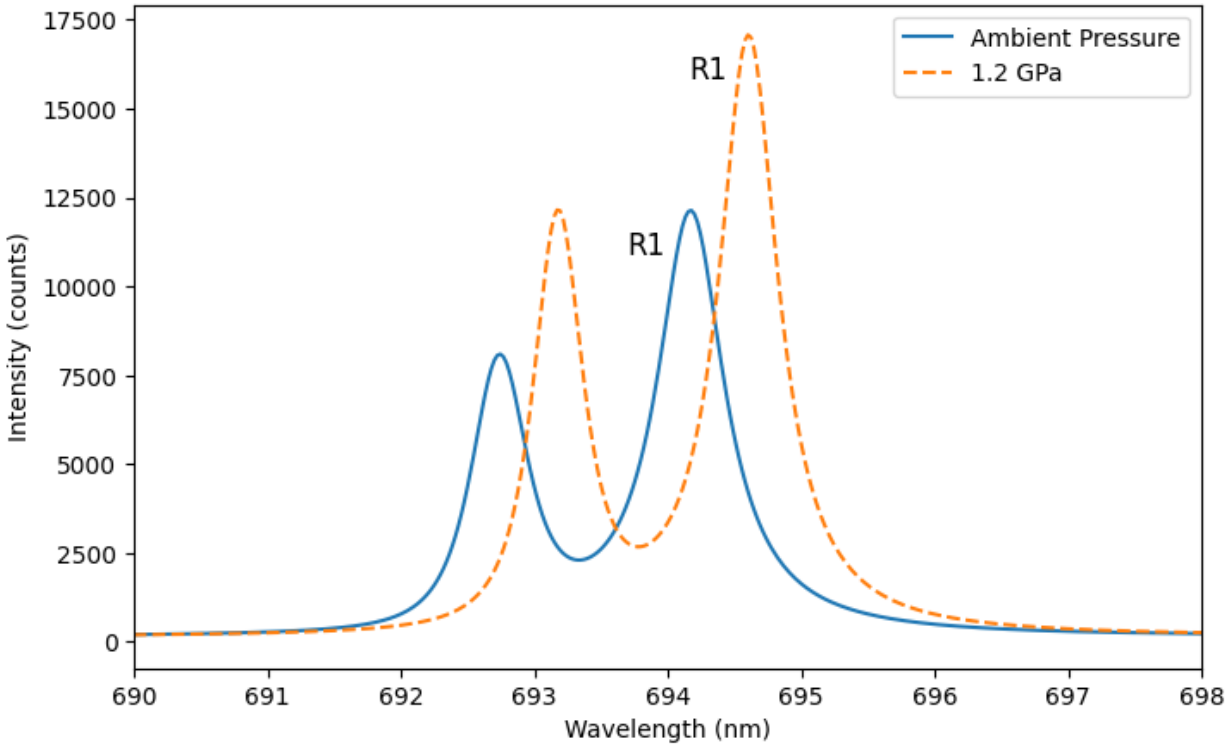

Figure 2.6: Spectra of the fluorescence doublet of ruby at 286.2 ± 0.6 K. Based on the reference (blue) and pressurized (orange) R1 lines, the calibrated pressure of this sample is 1195 ± 10 MPa. The reference PL spectra was collected from a single ruby sphere placed on the backside of the diamond anvil. The pressurized PL spectra was collected from a single ruby sphere in the sample chamber.

however, it is recommended to experimentally determine this value prior to loading the cell if diamond anvils are the primary pressure sensor or when expecting a loss of calibrant. The diamond anvil pressure gauge comes with caveats—the pressure chamber should be as small of a volume as possible; the Raman shift should be probed directly on top of or a few micrometers adjacent to the center of the anvil; and it should be probed exclusively on the internal surface of the anvil [35]. Deviating from these recommendations increases the uncertainty associated with the pressure measurement. An example of a pressure determination using the diamond anvil gauge is shown in Figure 2.7. The diamond gauge has an uncertainty closer to 50 to 100 MPa in the low pressure regime, so it is considered less reliable than ruby. For this reason, ruby is used as the primary pressure sensor for high-pressure experiments whenever possible.

2.1.3 Water as a Pressure Transmitting Medium

Pressure transmitting media also have an impact on the maximum pressures reached during an experiment. Though, as all experiments presented in Chapters 3 and 4 use water as both the sample and the pressure transmitting medium, this is not a major point of concern and will be briefly discussed in the context of the water Raman spectrum.

Pressure transmitting media, in theory, create an isotropic pressure environment in which gradients are minimized and pressure acts uniformly on the sample [40]. Due to shear stresses within single crystals of polycrystalline materials, ideal hydrostatic conditions are difficult to actualize in a DAC, both between grains of bulk solids and on samples interfacing with the diamond anvil. [24]. Fluids, inorganic salts, and even condensed or solidified inert gasses (e.g. Ar, Ne) offer hydrostatic and quasi-hydrostatic behavior at high pressure [41, 42]. Water is a hydrostatic medium free of gradient effects while in the liquid phase. As a solid, shear strains play a significant role in pressure distributions [41]. For these reasons, single crystals of high-pressure ices in equilibrium with the liquid are considered to be under hydrostatic pressure. If the majority of the water in the pressure chamber solidifies, it is important to remain close to the boundary of the phase transition. Otherwise, the assumption that

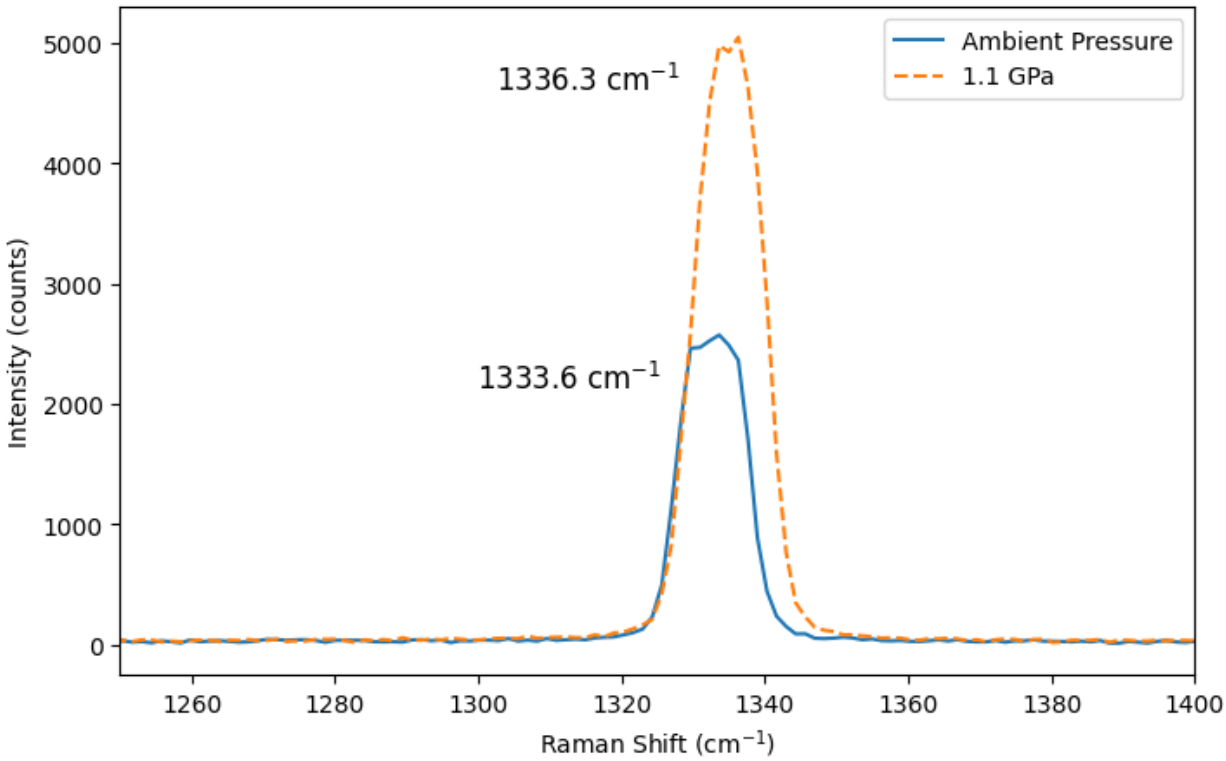

Figure 2.7: First-order Raman spectra from the culet of the diamond anvil both at ambient conditions (blue) and high pressure (orange). Based on the edge frequencies, the sample pressure is about 1.1 GPa. The peak stretches as pressure increases, and ultimately should be fit to a polynomial to better estimate sample pressures [35].

samples are under similar conditions is no longer valid.

In addition to visual cues and pressure calibrations, the water Raman spectra is foremost used to confirm the phase or phases of ice present during an experiment. The deconvolution of the broad O-H stretching band and assignment of individual vibrational modes have been the subject of historical debate; however, its general features change with pressure and structure [43]. Figure 2.8 shows the relative intensity and shift of the asymmetric and symmetric O-H stretching regions of liquid water, ice Ih, and ice VI. All three of these phases are proton disordered, meaning the position of hydrogen atoms is not necessarily fixed to a specific location at any given time. Rather, ice Ih and ice VI obey the ice rules, which require each oxygen atom to be surrounded by four hydrogen atoms—two covalently bonded, and two participating in hydrogen bonding [44].

The degree of hydrogen bonding in the liquid and solid forms dictates the primary contribution to the broad O-H stretching band. Hydrogen bonding in the liquid is weak compared to covalent bonding—hydrogen bonds are continuously broken and formed between random water molecules—and the ensuing flexible structure is reflected in the higher intensity of the asymmetric O-H stretching region (Figure 2.8, liquid water). Conversely, more extensive hydrogen bonding in the crystalline phases favors symmetric O-H stretching (Figure 2.8, ice Ih and ice VI) [45]. Furthermore, hydrogen bond strength and O-H bond strength are inversely related; that is, the stronger the hydrogen bond, the weaker the parent O-H bond [46]. As pressure is increased, the strength of hydrogen bonding within a single phase of ice increases, and the peak location of the symmetric stretching region red shifts to lower energies. Upon accessing a higher-pressure phase of ice, the hydrogen bonding lessens, and the peak blue shifts to higher energies instead (Figure 2.8, ice Ih and ice VI) [47]. These differences are on the order of 50 to 100 wavenumbers depending on the exact pressure and temperature conditions (Figure 2.8), and are accompanied by changes in overall band shape, so solid phases of ice are easily distinguished via Raman spectroscopy.

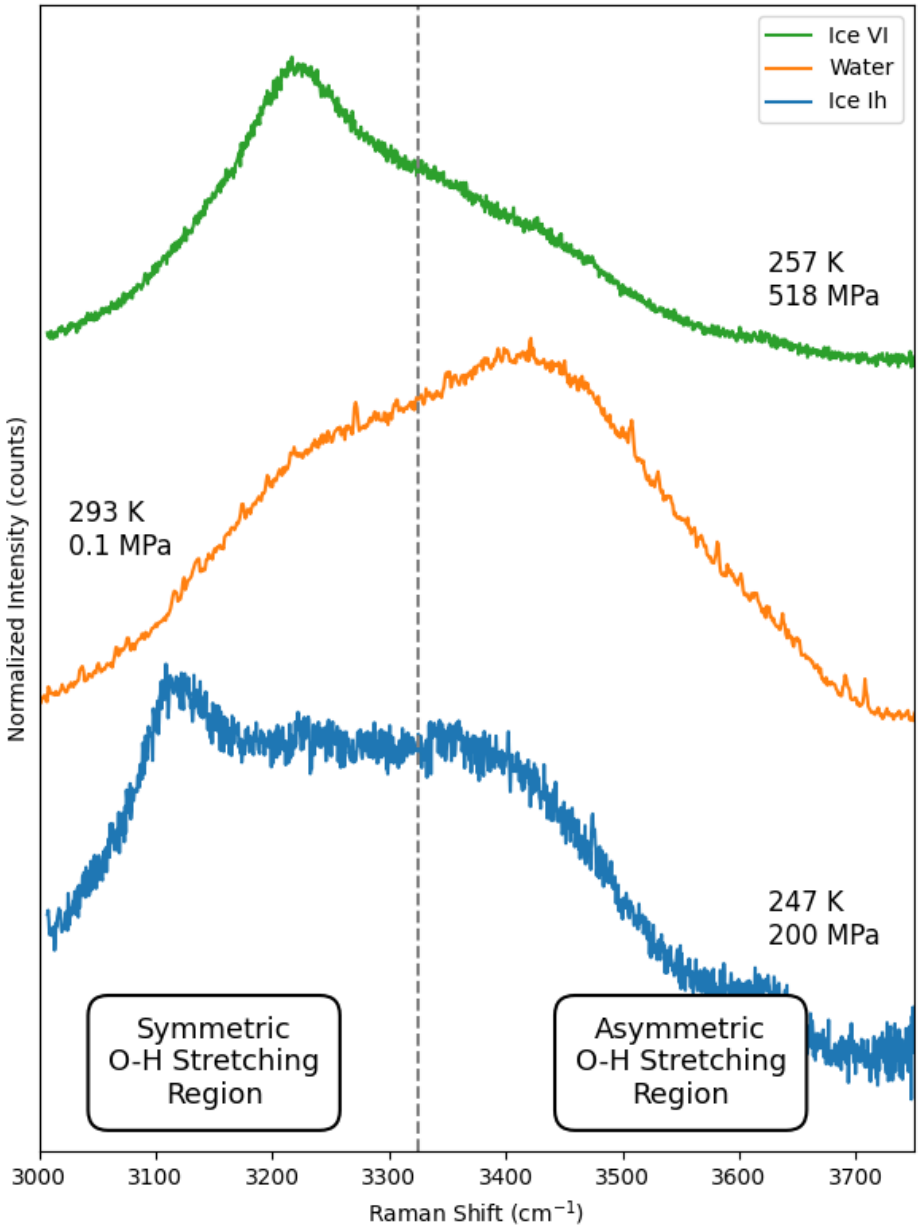

Figure 2.8: Example Raman spectra of the O-H stretching band for ice Ih (blue) at 247 K and 200 MPa, liquid water (orange) at 293 K and 0.1 MPa, and ice VI (green) at 257 K and 518 MPa. Spectra of ice Ih and ice VI were collected from single crystals inside a DAC at a 1 m concentration of $MgCl_2$. Ice Ih nucleates at some temperature below the freezing point. As pressure increases, ice Ih melts and the sample moves completely into the liquid phase, before isolating ice VI at pressures approaching one GPa. The dashed gray line separates regions that are more ice-like or liquid-like [45].

2.1.4 Low Temperature DAC Equipment

While DACs offer control over pressure, additional equipment is required to run experiments at non-ambient temperatures. In Chapter 4, the melting curves of water ices for salt binaries are determined at high pressures and low temperatures. In order to simultaneously regulate both parameters, a cryostat for the BX90 cell was designed in-house at the University of Washington Planetary Mineral Physics Laboratory. The components of the cryostat are displayed in Figure 2.9, and was built jointly by Prof. Baptiste Journaux and Dennis Canuelle at UW, modifying a preliminary design first developed by Noguchi and Okuchi (2016) [48]. The cryostat can reach temperatures as low as -50 °C.

Cryostat Assembly

The assembly of the cryostat, in detail, is as follows. A BX90 DAC is prepared, loaded, and pressurized as is typical for a high-pressure experiment. The top of the outer cylinder of the BX90 is screwed into the back window of the cryostat (Figure 2.9, 5). Small washers support two of the four screws to ensure that the BX90 sits parallel to the window, that the BX90 is not in contact with the window, and that the screws of the BX90, when tightened, do not make contact with the window. Once the BX90 is secured, the thermocouple that runs through a small hole on the front cryostat window (Figure 2.9, 6 and 7) is fed through the open body of the cryostat (Figure 2.9, 1) and plugged into an opening on the side of the BX90. The sensing tip of the thermocouple is in contact with the diamonds at the high-pressure sample chamber. Assuming there are no temperature gradients within the chamber, the thermocouple should give a relatively accurate reading of the sample temperature during the experiment. The BX90 is then slid into the cryostat body, and the back window is screwed into the cryostat. The front window is mechanically fit onto the cryostat. Both windows have O-rings that provide a hermetic seal. The rods that contact the screws on the bottom piston of the BX90 are installed (Figure 2.9, 8). The foam blocks that insulate the cryostat are placed around the copper blocks and Peltier coolers (Figure 2.9, 9 and 2), and

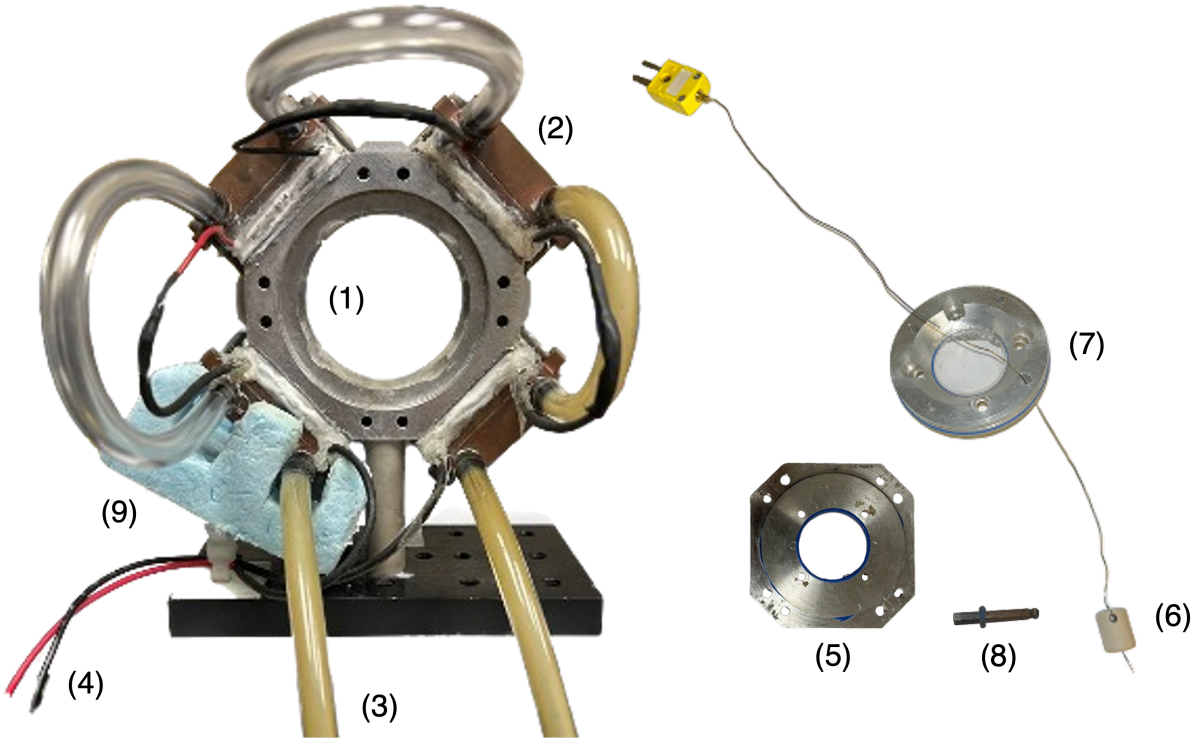

Figure 2.9: The assembly of a cryostat, compatible with the BX90 DAC. Components of interest are: (1) the cryostat body, mechanically fit to hold the BX90, (2) one of four sets of a copper block stacked on Peltier coolers, (3) exit and entrance flow lines for chilled water supply, (4) electrical connections for the power supply, (5) back window, to which the top of BX90 is secured, (6) thermocouple, with a plug to guide the tip of the thermocouple in contact with the diamond anvils, (7) the front window of the cryostat, (8) one of four rods that connect to the screws for the BX90, with O-rings that seal in the front window, and (9) one of four foam blocks that insulates the cryostat.

are cinched in place. Additional foam blocks around the front and back cryostat windows are added (not pictured).

The cryostat is on a mount that can be attached to a stage for use with an optical set-up. The sample chamber within the BX90 is aligned with the objective lens for the optics, so that images can be collected and the sample can be probed for PL and Raman spectroscopy. The exit and entrance flow lines of the cryostat are connected to a chilled water supply (Figure 2.9, 3). The water is fed through the four copper blocks that sit atop Peltier coolers on the cryostat body, removing heat from the system (Figure 2.9, 2). The Peltier coolers are wired in series, and the circuit is completed via connections to a power supply (Figure 2.9, 4). By modulating the voltage and amperage delivered to the Peltier coolers, the degree of cooling and thus the temperature of the sample chamber is controlled (Figure 2.10). The thermocouple is plugged into a temperature reader (Figure 2.9, 6). At particularly low temperatures (< -30 °C), condensation tends to form on the windows of the cryostat which hinders microscopic and Raman measurements, so a pressurized air supply is used to keep the windows dry.

2.2 Metrology

High-pressure experiments demand varying degrees of accuracy and precision. For instance, if pressure is used to generally characterize the sample environment or identify the sample phase, a simple calibration may suffice. If findings hinge on the exact pressure and temperature conditions—as is the case for thermodynamic phase equilibria measurements—data analysis is more intensive. Steps taken to improve the accuracy and precision of measurements are provided in detail.

2.2.1 Pressure Determination

As discussed in Section 2.1.2, Cr^{3+}-doped ruby spheres are accessible and reliable pressure sensors. The PL spectra of ruby is observed, and the wavelength associated with the R1 line is used to determine pressure, as per (2.2). A basic example of a ruby PL pressure calibration—

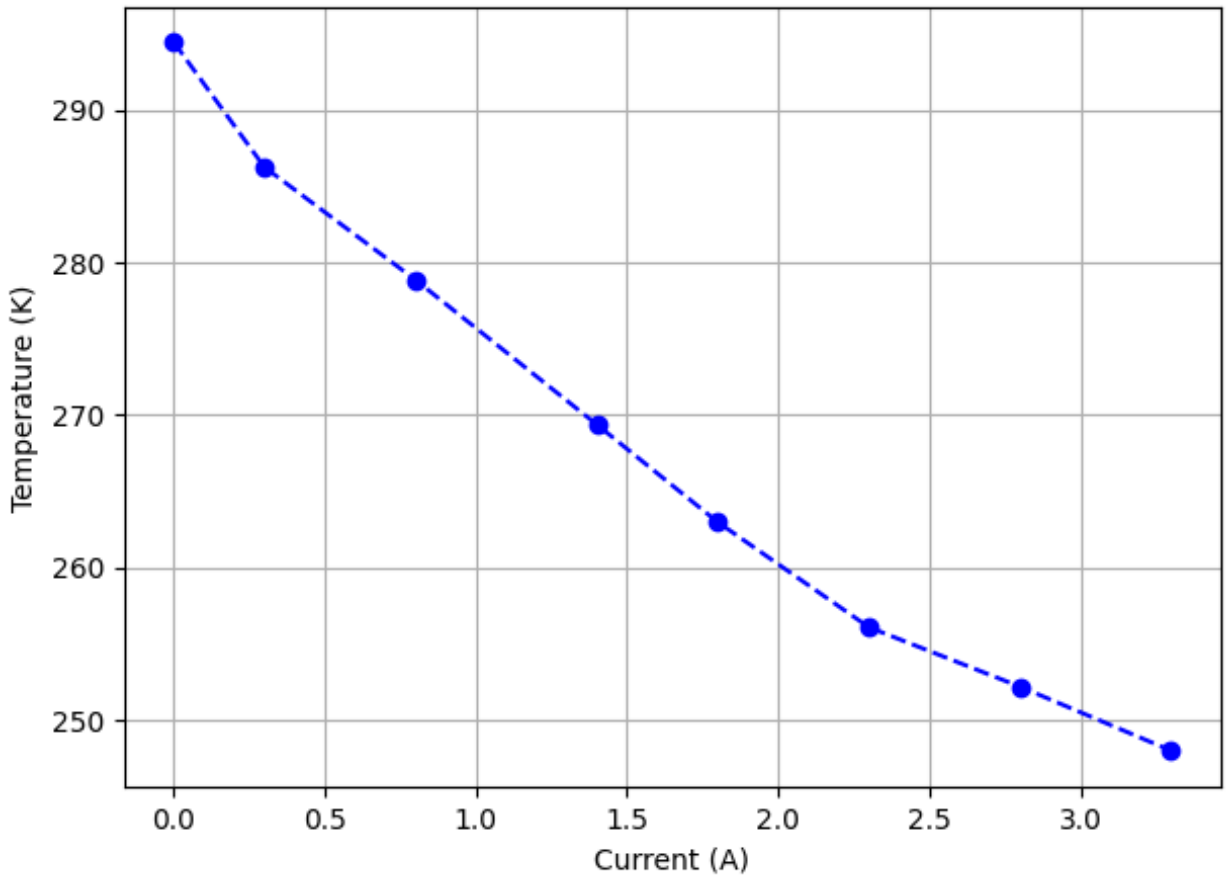

Figure 2.10: A plot of sample temperature and the current delivered in series (Figure 2.9, 4) to the Peltier cooling units (Figure 2.9, 2) of the DAC cryostat. Sample temperature was measured using a thermocouple (Figure 2.9, 6) in contact with a diamond anvil. Temperatures displayed are raw values as provided by a temperature reader from an experiment evaluating the melting curve of ice VI for a 2.2 m aqueous solution of $MgSO_4$. Temperature response is not linear, and as the cryostat apparatus cools, higher currents are required to reach lower temperatures.

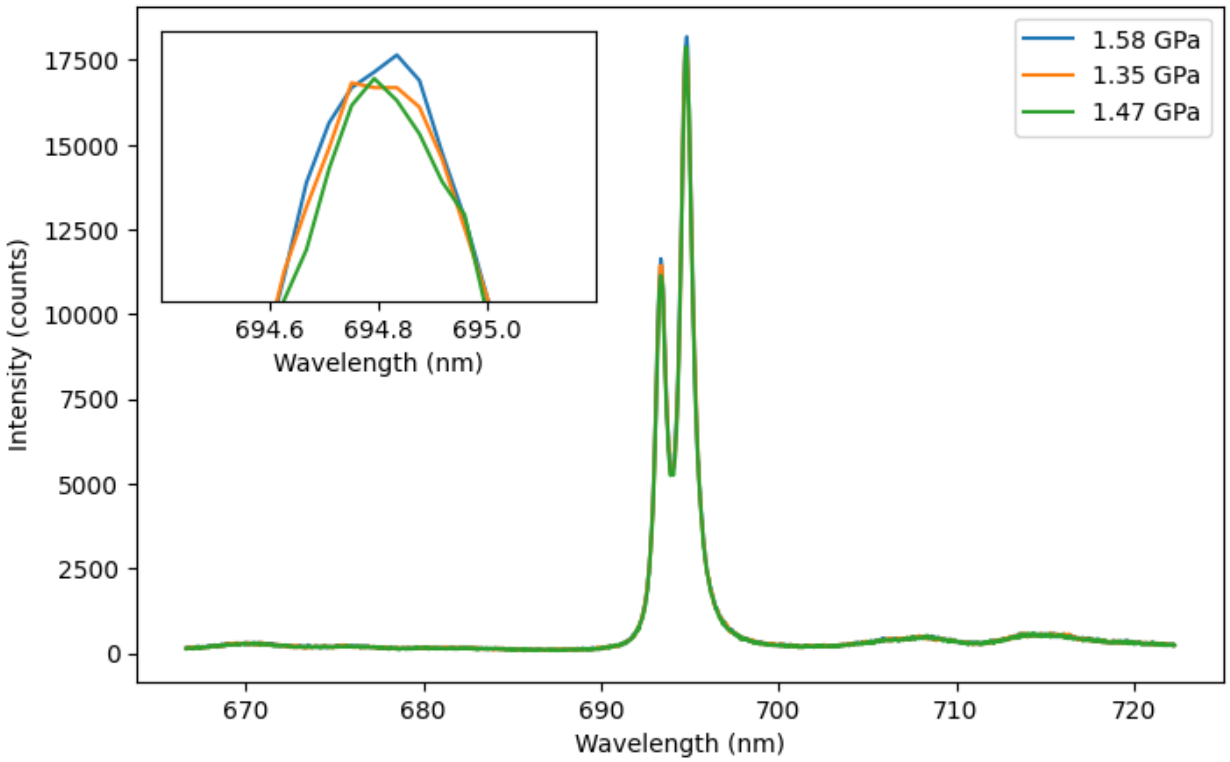

Figure 2.11: Sample pressures determined from a single ruby sphere, in triplicate. Pressures are calculated using the wavelength of highest intensity. These spectra were collected at room temperature. The ambient R1 line was assigned to 694.25 nm.

using raw spectra produced under identical conditions at room temperature, in triplicate—is shown in Figure 2.11. Upon examining the data, a few trends are apparent. While the spectra were collected at the exact same location on a single ruby sphere, there are slight variations in the shape of the uppermost part of the R1 peak (Figure 2.11, inset). Due to the resolution of the spectrometer, the highest-intensity wavelength also fluctuates. In tandem—considering the sensitivity of the ruby pressure gauge—using this wavelength as a proxy for the R1 line introduces an uncertainty of at least ± 100 MPa to the pressure calibration. In Chapter 3, pressure is used to verify that assays are run under similar conditions. The range of sample pressures exceeds the confidence interval for the measurement, and so an approximation of pressure (like in Figure 2.11) is reasonable.

To increase the accuracy of the pressure calibration, raw spectra are fit to two Pearson VII distributions—one for each of the peaks of the ruby fluorescence doublet—with a 3$^{\text{rd}}$-order polynomial background. The Pearson VII function was originally developed to model x-ray diffraction peaks, and is a valid approximation for general spectroscopic data [49]. It is particularly useful when peaks are sharp and their shape cannot be fully represented by either a Lorentzian, Gaussian, or Voigt distribution, as is the case for ruby fluorescence lines at high pressures and low temperatures [50, 51]. The Pearson VII function is expressed as:

$$f(x, h, x_0, \Gamma, m) = h * (1 + [\frac{(x - x_0)^2}{m * \Gamma^2}])^{-m} \tag{2.4}$$

where x is some measure of energy—in this case, wavelength (λ)—h is the peak amplitude, x_0 is the center of the peak, Γ is the full width at half maximum (FWHM), and m is the shape parameter. The shape parameter takes values over the range [1, ∞] and controls whether the function is closer to a Lorentzian ($m = 1$) or a Gaussian ($m \to \infty$) or somewhere in between [52].

Figure 2.12 is a printout of the ruby PL fitting software developed during this work, using the same data presented in Figure 2.11 (blue spectrum). The center wavelength of the Pearson VII function associated with the R1 line provides the true shift for the pressure calibration. The residuals show the difference between the raw data points and the curve estimated by the model. Smaller residuals are indicative of a better fit, and fluctuations around the center of the R1 line are expected and within a satisfactory margin [52]. The model is adjusted iteratively to provide an acceptable coefficient of determination (R-squared > 0.99).

The combined results of the Pearson VII fitting model for the example ruby PL spectra (Figure 2.11), and the updated pressure determination, are provided in Figure 2.13. The variance around the center of the peak is corrected and all R1 lines converge on 694.82 nm, reducing the uncertainty of the calibration by an order of magnitude, down to $\pm$10 MPa. This is the same upper limit of the precision achievable when temperature is known

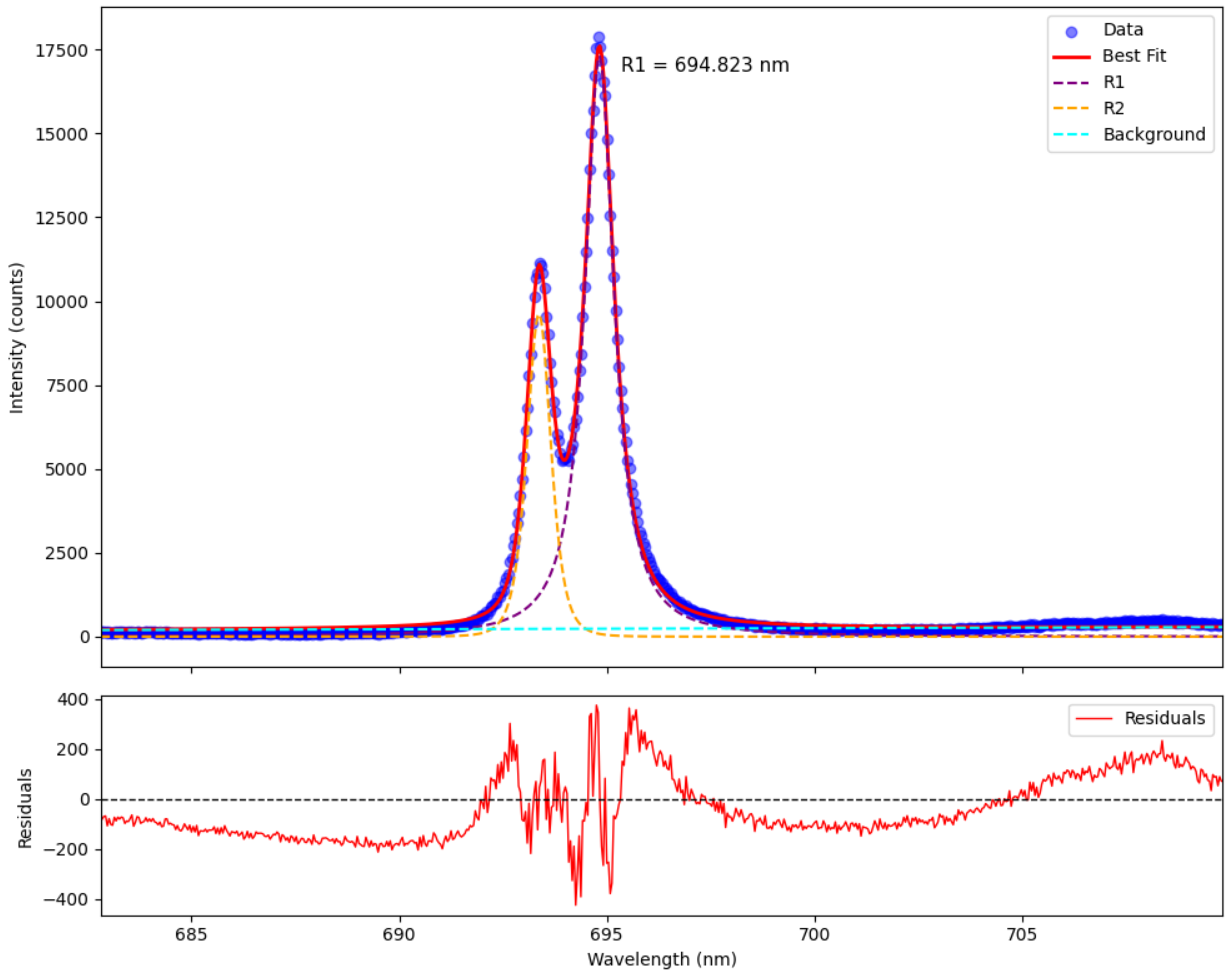

Figure 2.12: The ruby fluorescence doublet (raw spectrum, blue data points) plotted against two Pearson VII functions, modeling the R1 (purple, dashed line) and R2 (orange, dashed line) peaks. A flat background is included as 3rd-order polynomial (cyan, dashed line). The overall fit—the sum of the R1 and R2 lines—matches the raw data (red, solid line). Residuals are the difference between the best fit curve and the input spectrum.

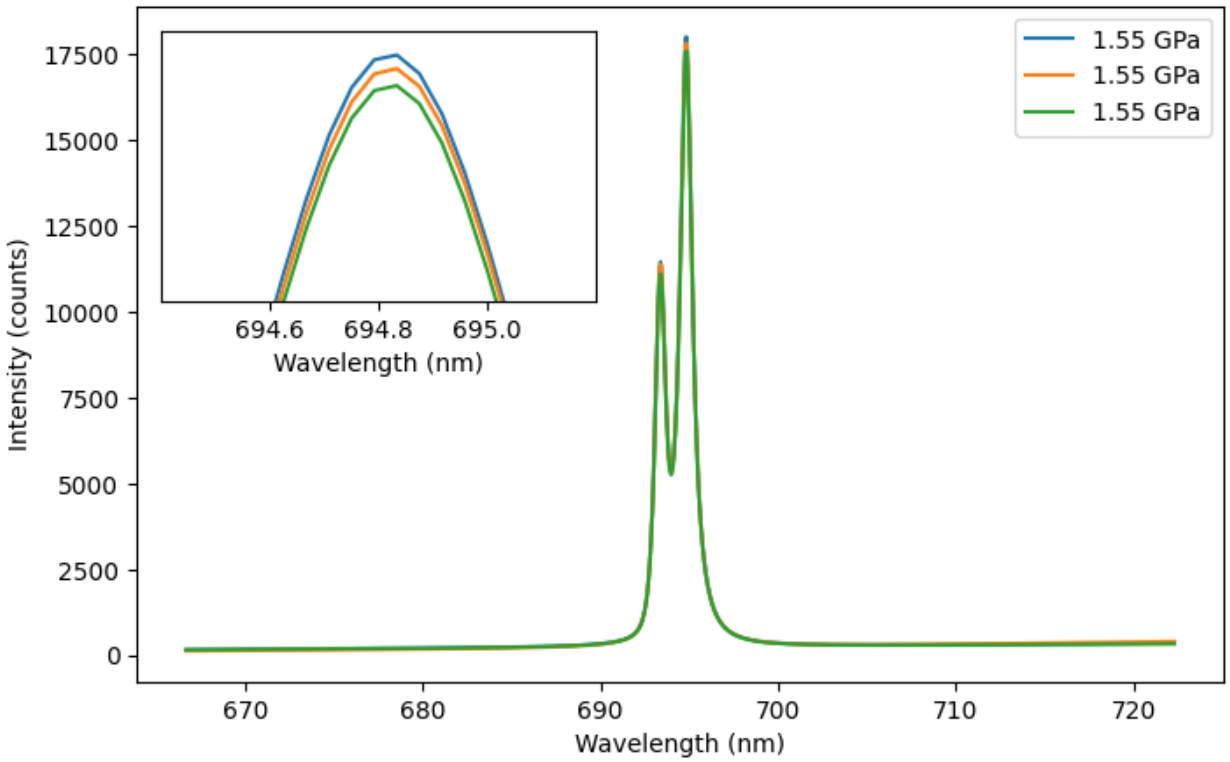

Figure 2.13: Fits of the triplicate of ruby spectra showed previously after modeling the raw data from Figure 2.11 using two Pearson VII functions. Pressures are calculated using the center wavelength of the R1 shift relative to 694.25 nm.

and pressures are relatively low (∼1 GPa) [53, 54]. There are a number of ways in which such precision could be viewed as coincidental, as the gauge—while well documented—is dependent on factors including the analytical fitting method [28].

At room temperature, the R1 line is predetermined at 694.25 nm; when performing experiments at low temperatures—like in Chapter 4—the literature value cannot be used and reference spectra must be collected to ensure the ruby pressure gauge is internally consistent. In this case, the precision of the fitting process is determined via a box plot, where each reference spectra is compared to the shifted spectra at high pressure. For a set of data in triplicate, this produces nine separate calibrations (Figure 2.14). If the uncertainty due to the fitting model itself is known for all sets of reference and high-pressure spectra, it

is propagated and included as error bars, expressed by the standard error propagation for functions of multiple variables:

$$\sigma_P = \sqrt{\sigma_{\lambda_0}^2 * (\frac{\partial P}{\partial \lambda_0})^2 + \sigma_\lambda^2 * (\frac{\partial P}{\partial \lambda})^2} \tag{2.5}$$

where σ_{λ_0} and σ_λ are the uncertainties associated with the fitting of the R1 lines for the reference and high-pressure spectra, and $\partial P/\partial \lambda_0$ and $\partial P/\partial \lambda$ are the partial derivatives of pressure with respect to λ_0 and λ as defined by (2.2), respectively [55]. Conservatively, the sample pressure is assigned to the median calibration ± the length of the longest whisker, as in Figure 2.14. Including outliers, the distribution is always within a ± 10 MPa range. This is the same degree of precision for the example calibration performed at room temperature fitting only high-pressure spectra (Figure 2.13).

Calibrations related to pressure measurements are dependent on spectrometer parameters, fitting conventions, and external DAC equipments. This can seem daunting in the face of efforts to increase the accuracy and precision of experimental data. Independent of the implications on and immediate relevance of pressure calibrations to preliminary findings, every experimental pipeline in the high-pressure field should implement this kind of analysis.

2.2.2 Temperature Determination

Similar to the assessment of pressure calibrations, the temperature of each measurement should also be checked for accuracy and precision. For deionized (DI) water—the solvent of choice for the salt solutions in Chapter 4—melting curves at variable pressures and temperatures for ice Ih and ice VI are experimentally traced and compared to those provided in the literature [23, 56]. Error introduced by raw temperature values from either the thermocouple (Figure 2.9, 6) or the temperature reader is accounted for by a 2^{nd}-order polynomial model given in Figure 2.15. The difference between the recorded temperature and the true temperature of the melting points along the liquid-Ih and liquid-VI transitions of water from 0.1 to roughly 1000 MPa are calculated and plotted based on the response of the tempera-

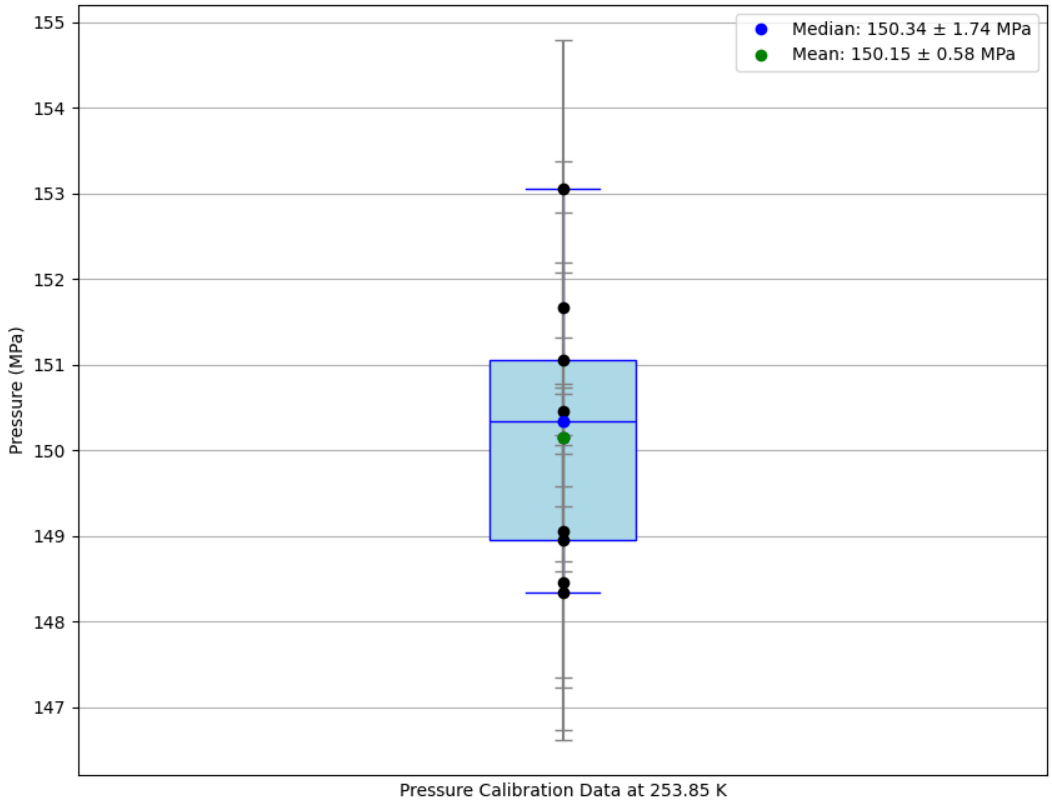

Figure 2.14: A box plot comparing pressure calibrations matching reference spectra and high-pressure spectra collected in triplicate and processed using the Pearson VII fitting model. The plot shows the variance in the calibration (data points) as it relates to precision and the uncertainty from the fitting model (error bars for single data points). The pressure of this sample—a point on the melting curve of ice Ih at low temperature—is 150.3 ± 5 MPa.

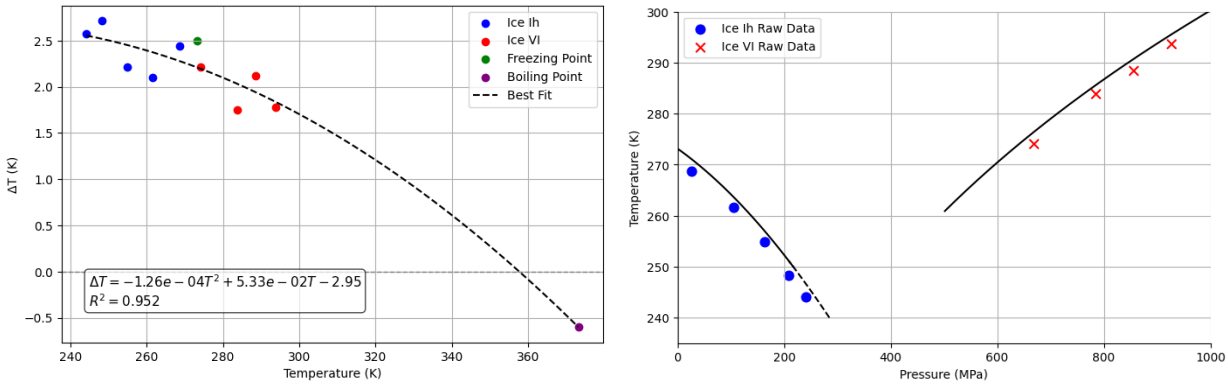

Figure 2.15: Left: A comparison of temperatures experimentally determined for the melting curves of pure water and the literature of the known phase transition. ΔT is the difference between these two points at any given pressure for ice Ih (blue) and ice VI (red), including the freezing (green) and boiling (purple) points measured from an ice bath and beaker of boiling water, respectively. Right: the raw ice Ih (blue) and ice VI (red) liquidus points compared to the melting curves of pure water from Wagner et al. (2011) [57]. The difference in temperature is attributed to the combined response of the thermocouple and temperature reader.

ture reader, independent of pressure. A reasonable fit is determined and used to correct the melting curve measurements, along with a confidence interval of ± 0.6 K, corresponding to the distance of the furthest point away from the curve.

2.2.3 Melting Point Determination

An additional, potential source of error for pressure determinations specific to melting curve data collection (Chapter 4) is related to the grain size of ice crystals at equivalent temperatures. In theory, for a pure system at constant temperature, an ice crystal in equilibrium with the liquid should be at a single pressure. In practice, the sensitivity of temperature measurements inside of a cryostat can mask effects due to crystal size—changing the size of a crystal via pressure, e.g., tightening the screws of a DAC, should in turn adjust the temperature to remain along the melting curve.

The calibration for the cryostat system discussed in Section 2.1.4 as related to pressure and ice grain size at a constant temperature is shown in Figure 2.16. Maps of grain size

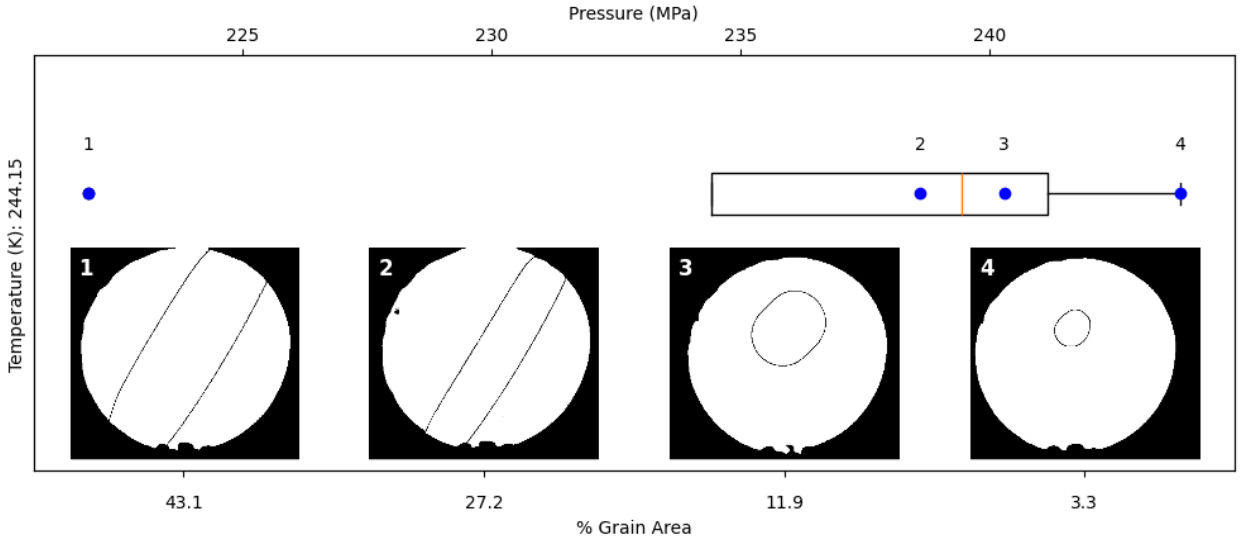

Figure 2.16: A box plot quantifying the impact of ice crystal grain size on sample pressure, at a single observable temperature. Maps of grain size are included for reference. Both the sample and pressure transmitting medium are deionized water.

as a percentage of grain area are produced using the interactive watershed program in Fiji (ImageJ) [58]. Pressure is calculated as per the protocol described in this chapter. There is a 6 MPa range associated with moderate fluctuations in grain sizes and up to a 10 MPa range including the pressure assigned to size four (Figure 2.16). Treating this plot in the same manner as that for the pressure calibrations (Figure 2.14), an estimation of uncertainty of up to $\pm$ 10 MPa remains reasonable. Importantly, Figure 2.16 demonstrates melting pressure fluctuations at a constant temperature for deionized water; the experiments for Chapter 4 with aqueous salt solutions always have minimized ice crystal sizes to report uniform data, as is discussed in the following subsection.

2.2.4 Concentration Determination

The exact concentration of sample solutions used to determine melting curves of inorganic salt binaries (Chapter 4) is also calibrated after loading. Because of evaporation due to the small volume of loaded samples, the concentration of prepared solutions tends to increase

between being placed atop and trapped within the pressure chamber [59]. To properly estimate the concentration of solutions of interest, the ice Ih freezing point close to 1 bar is determined after loading. To achieve this, screw tightness is decreased until a small air bubble forms inside the sample chamber, confirming the solid-liquid equilibrium at ambient pressure. The cell is either allowed to warm naturally or removed from the cryostat and gently heated, and the melting temperature of either species is recorded. This is compared to the known phase diagram of the corresponding aqueous system at one bar (Appendix B contains the temperature-concentration phase diagrams for the salt-water binaries of $MgSO_4$, Na_2SO_4, and $MgCl_2$).

When determining points along the melting curve for binary solutions, ice crystal sizes are minimized to prevent increasing the concentration of the solution due to factional crystallization of pure ice. As compared to the distribution of ice grains monitored for the temperature calibration (Figure 2.16), grain size is consistently smaller ($< 3\%$ grain area) and is akin to the size of an individual ruby sphere (estimated to be about 50 µm on the top end). This ensures that the melting point measurements is representative of ice in equilibrium with a solution as close as possible to the loaded concentration. This is also a way to approach the true definition of the liquidus, which is the the last point at which ice remains stable in a solution of given concentration.

2.3 Resource Availability

The fitting protocol for pressure calibrations using the ruby gauge (Section 2.2.1) is available as a simple, python-based graphical user interface (GUI) for real-time data analysis (GitHub repository: `https://github.com/cwoodburnphd/Ruby-PL-Pressure-Calibration-GUI`). At least one reference and one high-pressure spectra of the ruby fluorescence doublet are required. The GUI also has the capability to correct temperature measurements based on experimentally-determined two-point calibrations or hard-coded polynomial equations (Section 2.2.2).

In total, a significant amount of time and effort went into the exploration of metrology

for traditional DAC experiments and high-pressure experiments at low temperatures. The culmination of these efforts are the pressure, temperature, and concentration calibrations discussed in this chapter, which have led to the provision of some of the most accurate and precise thermodynamic data to date at elevated pressures. Sharing these methods with the high-pressure community is a great way to attempt to increase the quality and reproducibility of future data.

References

1. Kantor, I. *et al.* BX90: A new diamond anvil cell design for X-ray diffraction and optical measurements. *Rev. Sci. Instrum.* **83,** 125102 (2012).
2. Challener, W. A. & Thompson, J. D. Far-Infrared Spectroscopy in Diamond Anvil Cells. *Appl. Spectrosc.* **40,** 298–303 (1986).
3. Kurnosov, A., Criniti, G., Boffa Ballaran, T., Marquardt, H. & Frost, D. J. High pressure and high temperature Brillouin scattering measurements of pyrope single crystals using flexible CO_2 laser heating systems. *Phys. Chem. Miner.* **51,** 38 (2024).
4. Journaux, B. *et al.* On the identification of hyperhydrated sodium chloride hydrates, stable at icy moon conditions. *PNAS* **120,** e2217125120 (2023).
5. Upadhyay, A., Rajput, P. & Sinha, A. K. A XANES measurement set-up using Diamond Anvil Cell at BL-09, Indus-2 and demonstrative experiments. *AIP Conf. Proc.* **2265,** 030210 (2020).
6. Wang, Z., McPherson, C., Kadado, R., Casey, W. H. & Curro, N. *Chapter Eight - Optically detected NMR in a diamond-anvil cell for geochemistry* in *Advances in Inorganic Chemistry* (eds Hubbard, C. D. & van Eldik, R.) **78** (Academic Press, 2021), 269–287.
7. Matsumoto, R. *et al.* Novel Diamond Anvil Cell for Electrical Measurements using Boron-doped Metallic Diamond Electrodes. *Rev. Sci. Instrum.* **87,** 076103 (2016).
8. Wang, M. *et al.* Imaging magnetic transition of magnetite to megabar pressures using quantum sensors in diamond anvil cell. *Nat. Commun.* **15,** 8843 (2024).
9. Sato-Sorensen, Y. in *High-Pressure Research in Mineral Physics: A Volume in Honor of Syun-iti Akimoto* 53–59 (American Geophysical Union (AGU), 1987).
10. Decremps, F. *et al.* Sound velocity of iron up to 152 GPa by picosecond acoustics in diamond anvil cell. *Geophys. Res. Lett.* **41,** 1459–1464 (2014).
11. Giancoli, D. *Physics: Principles with Applications (7th Edition)* (Pearson, 2014).

12. Tomkinson, G. R. *et al.* International norms for adult handgrip strength: A systematic review of data on 2.4 million adults aged 20 to 100+ years from 69 countries and regions. *J. Sport Health Sci.* **14,** 101014 (2025).

13. Eremets, M. I. *et al.* The strength of diamond. *Appl. Phys. Lett.* **87,** 141902 (2014).

14. Yang, H., Ma, Y. & Dai, Y. Progress of structural and electronic properties of diamond: a mini review. *Funct. Diamond* **1,** 150–159 (2022).

15. Dubrovinsky, L., Dubrovinskaia, N., Prakapenka, V. B. & Abakumov, A. M. Implementation of micro-ball nanodiamond anvils for high-pressure studies above 6 Mbar. *Nat. Commun.* **3,** 1163 (2012).

16. Walker, J. Optical absorption and luminescence in diamond. *Rep. Prog. Phys.* **42,** 1605–1659 (1979).

17. Davies, G., Hamer, M. F. & Price, W. C. Optical studies of the 1.945 eV vibronic band in diamond. *Proc. R. Soc. Lond. A* **348,** 285–298 (1997).

18. Collins, A. T., Connor, A., Ly, C.-H., Shareef, A. & Spear, P. M. High-temperature annealing of optical centers in type-I diamond. *J. Appl. Phycol.* **97,** 083517 (2005).

19. Smith, C. P. *et al.* GE POL Diamonds: Before and After. *Gems Gemol.* **36,** 192–215 (2000).

20. Jelezko, F. *et al.* Spectroscopy of Single N-V Centers in Diamond. *Single Molecules* **2,** 255–260 (2001).

21. Hamilton, A. & Menzies, R. I. Raman spectra of mirabilite, $Na_2SO_4{\cdot}10H_2O$ and the rediscovered metastable heptahydrate, $Na_2SO_4{\cdot}7H_2O$. *J. Raman Spectrosc.* **41,** 1014–1020 (2010).

22. O'Bannon, E. F., Jenei, Z., Cynn, H., Lipp, M. J. & Jeffries, J. R. Contributed Review: Culet diameter and the achievable pressure of a diamond anvil cell: Implications for the upper pressure limit of a diamond anvil cell. *Rev. Sci. Instrum.* **89,** 111501 (2018).

23. Fletcher, N. H. *The Chemical Physics of Ice* (Cambridge University Press, 1970).

24. Takemura, K. Hydrostaticity in high pressure experiments: some general observations and guidelines for high pressure experimenters. *High Pressure Res.* **41,** 155–174 (2021).

25. Merrill, L. & Bassett, W. A. Miniature diamond anvil pressure cell for single crystal x-ray diffraction studies. *Rev. Sci. Instrum.* **45,** 290–294 (1974).

26. Mao, H. K., Xu, J. & Bell, P. M. Calibration of the ruby pressure gauge to 800 kbar under quasi-hydrostatic conditions. *J. Geophys. Res.: Solid Earth* **91,** 4673–4676 (1986).

27. Silvera, I. F., Chijioke, A. D., Nellis, W. J., Soldatov, A. & Tempere, J. Calibration of the ruby pressure scale to 150 GPa. *Phys. Status Solidi B* **244,** 460–467 (2007).

28. Shen, G. *et al.* Toward an international practical pressure scale: A proposal for an IPPS ruby gauge (IPPS-Ruby2020). *High Pressure Res.* **40,** 299–314 (2020).

29. Kraus, R. G. *et al.* Dynamic compression of copper to over 450 GPa: A high-pressure standard. *Phys. Rev. B* **93,** 134105 (2016).

30. Fratanduono, D. E. *et al.* Establishing gold and platinum standards to 1 terapascal using shockless compression. *Science* **372,** 1063–1068 (2021).

31. Chervin, J. C., Power, C. & Polian, A. Quartz as a pressure sensor in the infrared. *High Pressure Res.* **25,** 97–105 (2005).

32. Akahama, Y. & Kawamura, H. Pressure calibration of diamond anvil Raman gauge to 310 GPa. *J. Appl. Phys.* **100,** 043516 (2006).

33. Trots, D. M. *et al.* The Sm:YAG primary fluorescence pressure scale. *J. Geophys. Res.: Solid Earth* **118,** 5805–5813 (2013).

34. Eremets, M. I. *et al.* Universal diamond edge Raman scale to 0.5 terapascal and implications for the metallization of hydrogen. *Nat. Commun.* **14,** 907 (2023).

35. Eremets, M. I. Megabar high-pressure cells for Raman measurements. *J. Raman Spectrosc.* **34,** 515–518 (2003).

36. Forman, R. A., Piermarini, G. J., Barnett, J. D. & Block, S. Pressure Measurement Made by the Utilization of Ruby Sharp-Line Luminescence. *Science* **176,** 284–285 (1972).

37. Mao, H. K., Bell, P. M., Shaner, J. W. & Steinberg, D. J. Specific volume measurements of Cu, Mo, Pd, and Ag and calibration of the ruby R1 fluorescence pressure gauge from 0.06 to 1 Mbar. *J. Appl. Phys.* **49,** 3276–3283 (1978).

38. Piermarini, G. J., Block, S., Barnett, J. D. & Forman, R. A. Calibration of the pressure dependence of the R1 ruby fluorescence line to 195 kbar. *J. Appl. Phys.* **46,** 2774–2780 (1975).

39. Kunc, K., Loa, I. & Syassen, B. Equation of state and phonon frequency calculations of diamond at high pressures. *Phys. Rev. B* **68,** 094107 (2003).

40. Shu-Jie, Y., Liang-Chen, C. & Chang-Qing, J. Hydrostaticity of Pressure Media in Diamond Anvil Cells. *Chin. Phys. Lett.* **26,** 096202 (2009).

41. Piermarini, G. J., Block, S. & Barnett, J. Hydrostatic limits in liquids and solids to 100 kbar. *J. Appl. Phys.* **44,** 5377–5382 (1973).

42. Klotz, S., Chervin, J. C., Munsch, P. & Le Marchand, G. Hydrostatic limits of 11 pressure transmitting media. *J. Phys. D: Appl. Phys.* **42,** 075413 (2009).

43. Wang, Z., Pakoulev, A., Pang, Y. & Dlott, D. D. Vibrational substructure in the OH stretching band of water. *Chem. Phys. Lett.* **378,** 281–288 (2003).

44. Bernal, J. D. & Fowler, R. H. A Theory of Water and Ionic Solution, with Particular Reference to Hydrogen and Hydroxyl Ions. *J. Chem. Phys.* **1,** 515–548 (1933).

45. Đuričković, I. *et al.* Water–ice phase transition probed by Raman spectroscopy. *J. Raman Spectrosc.* **42,** 1408–1412 (2011).

46. Ghosh, N., Roy, S., Bandyopadhyay, A. & Mondal, J. A. Vibrational Raman Spectroscopy of the Hydration Shell of Ions. *Liquids* **3,** 19–39 (2023).

47. Minceva-Sukarova, B., Sherman, W. F. & Wilkinson, G. R. The Raman spectra of ice (Ih, II, III, V, VI and IX) as functions of pressure and temperature. *J. Phys. C: Solid State Phys.* **17,** 5833–5850 (1984).

48. Noguchi, N. & Okuchi, T. A Peltier cooling diamond anvil cell for low-temperature Raman spectroscopic measurements. *Rev. Sci. Instrum.* **87,** 125107 (2016).

49. Üstün, B., Melssen, W. J. & Buydens, L. M. C. Facilitating the application of Support Vector Regression by using a universal Pearson VII function based kernel. *Chemom. Intell. Lab. Syst.* **81,** 29–40 (2006).

50. Gupta, S. K. Peak Decomposition using Pearson Type VII Function. *J. Appl. Crystallogr.* **31,** 474–476 (1998).

51. Nakano, K., Akahama, Y., Ohishi, Y. & Kawamura, H. Ruby Scale at Low Temperatures Calibrated by the NaCl Gauge: Wavelength Shift of Ruby R1 Fluorescence Line at High pressure and Low Temperature. *Jpn. J. Appl. Phys.* **39,** 1249 (2000).

52. Hall Jr., M. M., Veeraraghavan, V. G., Rubin, H. & Winchell, P. G. The approximation of symmetric X-ray peaks by Pearson type VII distributions. *J. Appl. Crystallogr.* **10,** 66–68 (1977).

53. Syassen, K. Ruby under pressure. *High Pressure Res.* **28,** 75–126 (2008).

54. Grasset, O. Calibration of the R ruby fluorescence lines in the pressure range [0-1 GPa] and the temperature range [250-300 K]. *High Pressure Res.* **21,** 139–157 (2001).

55. Fantner, G. *A brief introduction to error analysis and propagation* 2011.

56. Journaux, B. *et al.* Holistic Approach for Studying Planetary Hydrospheres: Gibbs Representation of Ices Thermodynamics, Elasticity, and the Water Phase Diagram to 2,300 MPa. *J. Geophys. Res. E: Planets* **125,** e2019JE006176 (2020).

57. Wagner, W., Riethmann, T., Feistel, R. & Harvey, A. H. New Equations for the Sublimation Pressure and Melting Pressure of H_2O Ice Ih. *J. Phys. Chem. Ref. Data* **40,** 043103 (2011).

58. Vincent, L. & Soille, P. Watersheds in digital spaces: an efficient algorithm based on immersion simulations. *IEEE Trans. Pattern Anal. Mach. Intell.* **13,** 583–598 (1991).

59. Silberberg, M. *Chemistry: The Molecular Nature of Matter and Change* (McGraw-Hill Science/Engineering/Math, 2006).

Chapter 3

INHIBITION OF ICE RECRYSTALLIZATION BY A PEPTIDE AT GIGAPASCAL PRESSURES: A FUNCTIONAL AND DETECTABLE BIOSIGNATURE FOR ICY MOONS

Subsurface oceans in icy moons such as Ganymede, Callisto, and Titan are bound by high-pressure polymorphs of ice, including ice VI at depths where pressures exceed ten thousand atmospheres.[1] Any putative life in their hydrosphere would need to survive in close contact with ice phases over that entire range. Strategies used by life on Earth's cryosphere ecosystems rely on antifreeze proteins (AFPs) and glycoproteins (AFGPs), which are known to inhibit ice recrystallization under cold conditions. However, large and complex organic molecules typically lose their functionality at extreme pressures. Here, we demonstrate for the first time ice recrystallization inhibition (IRI) activity against a high-pressure ice polymorph (ice VI) using a minimalistic peptide, IBP 8 (KCCTKNCDSTAHCT), under conditions relevant to the interiors of large icy moons. Using a novel high-pressure adaptation of the splat assay—termed the "squeeze assay"—we show that IBP 8 dramatically limits ice VI grain growth, reducing grain size by $\sim 70\%$ relative to controls. IBP 8 also outperforms canonical type III AFP, which is inactive at these pressures. To assess the detectability

[1]This chapter is a pre-submission manuscript draft that contains collaborative work, formatted for inclusion in this dissertation. The author designed, planned, and performed all novel "squeeze assay" experiments and analysis presented herein, with the assistance of Baptiste Journaux, Chaman Gupta and Andy Feng. Laser desorption mass spectrometry measurements and analysis (affiliated with NASA Goddard) were performed by M. Joseph Pasterski under the supervision of Melissa Trainer and Xiang Li, with additional support from Desmond A. Kaplan, Friso van Amerom, Marco E. Castillo, Jacob Graham, Ryan M. Danell, William B. Brinckerhoff, and Andrej Grubisic. Impact ionization mass spectrometry measurements and analysis (affiliated with NASA JPL) were performed by K. Marshall Seaton and Sankhabrata Chandra under the supervision of Bryana L. Henderson and Morgan Cable. Protein materials shared and validated by Tobias Weidner. The author created the first draft of the full manuscript with M. Joseph Pasterski and K. Marshall Seaton responsible for the text and figures of their respective sections. Edits by the author, Morgan Cable and Baptiste Journaux. Additional consideration of edits by William B. Brinckerhoff, Tobias Weidner, Xiang Li, and Bryana L. Henderson.

of such peptides as potential biosignatures, we analyze IBP 8 using two spaceflight-relevant mass spectrometry techniques: laser desorption mass spectrometry (LDMS), as implemented on the Dragonfly mission to Titan, and hypervelocity impact ionization mass spectrometry, analogous to the SUDA instrument on Europa Clipper. IBP 8 yields distinct molecular and fragment ion signatures across both platforms, including degradation markers correlated with loss of IRI activity. These findings suggest that small, pressure-resilient ice-binding peptides could represent a new subtype of functional biosignatures, tailored to cryogenic high-pressure environments and detectable by current instrumentation. The biochemical plausibility and detectablility of antifreeze peptides supports their inclusion as a new type of environment-specific molecular biosignatures to target in current and future ocean world missions.

3.1 Introduction

Water is considered a "universal solvent" capable of dissolving more substances than any other liquid; it also can remain in the liquid phase over a wide range of temperatures and pressures [1]. These properties are essential for maintaining biomolecular and cellular structures and important in a medium suitable for propagation of microorganisms [2]. Ice-rich planetary bodies of the outer solar system, like Titan, Enceladus, Ganymede, Europa, and Callisto, all contain liquid water reserves under frozen, inhospitable surfaces. Large icy moons—Ganymede, Callisto, and Titan—possibly hide a thick ocean between an upper crust of hexagonal ice (Ih) and a lower crust of high-pressure ices. These include ice III, ice V and tetragonal ice VI, as hydrospheric pressures increase to a maximum of 1.8 gigapascals (GPa) [3–5]. Among the possible chemical compositions of subsurface oceans, NaCl-H_2O is expected based on a combination of space probe magnetic field observations, *in situ* analysis of grain chemistry, and geochemical modeling [6].

Icy ocean worlds have become prime astrobiological targets [7]. They may provide the ingredients necessary to sustain the development of extremophilic life [8–12]. However, much uncertainty remains regarding the types of biosignatures detectable on icy worlds, either

through remote sensing or *in situ* analysis. Of the techniques available for spaceflight exploration (see, e.g., Seaton et al., 2022), mass spectrometry (MS) offers distinct advantages [13]. It permits the analysis of a broad range of complex materials, providing detailed information on structure and functionality through fly-by, orbital, and/or lander architectures [14, 15]. The Europa Clipper mission, which is slated to arrive at the Jovian system in 2030, will examine the surface and exospheric composition of Europa and investigate any organic compounds present via time-of-flight MS (with both the SUrface Dust Analyzer, SUDA, and the Mass Spectrometer for Planetary Exploration/Europa, MASPEX), among other techniques [16, 17]. The NASA Dragonfly mission will use laser desorption MS—one of many analytical capabilities of the Dragonfly Mass Spectrometer (DraMS) system—to aid in the characterization of complex organics, potentially relevant prebiotic chemistry, or biological activity on Titan [11, 18, 19]. And a future mission concept such as the Enceladus Orbilander may carry one or more MS-based instruments to characterize the organic chemical inventory of plume materials, identify and quantify biomolecules, and search for enantiomeric enrichment [20]. However, the exact types of target molecules that would constitute a biosignature (on icy worlds or elsewhere) remain uncertain; there is an immense diversity of both environments and instrumentation involved in the exploration of our solar system and beyond [21]. In that context, identifying environment-specific signatures (i.e. cryo-environments, possibly at elevated pressures) is one strategy to help focus investigations on a much more limited set of parameters and hypotheses. In the case of icy moons, it is reasonable to expect putative life to rely on substances enhancing survivability in close contact with ices and at elevated pressure.

Cold-adapted organisms in Earth's cryosphere have evolved antifreeze proteins (AFPs) and antifreeze glycoproteins (AFGPs) to delay ice crystal nucleation and inhibit ice recrystallization [22]. Without antifreeze mechanisms, ice growth inside cells causes them to rupture, resulting in frostbite and eventually the death of the organism. Each type of AFP and AFGP exhibits site-specific binding and varying degrees of thermal hysteresis (TH) and ice recrystallization inhibition (IRI) activity. This depends on the configuration of their ice-binding

site, the prevalence of repeat amino acid sequences, and their secondary and tertiary structure [23–25]. Native AFPs have been isolated primarily from fish that survive temperatures as low as -1.9 °C [23]. Atlantic cod venture to great depths, as far as 365 meters underwater, experiencing external pressures up to 3.8 megapascals (MPa). Yet, such pressures pale in comparison to those at the interface of icy planetary bodies; the bottom of Ganymede's hydrosphere is about 1.8 GPa for sea water [4].

Life on Earth has been observed to tolerate—at least temporarily—pressures in excess of one GPa [26]. Even so, studies indicate that pressure impedes protein function. Approaching and exceeding 800 MPa, water molecules penetrate protein interiors, resulting in swollen, globular structures that tend to unfold [27]. At above one GPa, proteins in solution start to unfold irreversibly. Lyophilized proteins exposed to very high pressures (8 GPa) can also exhibit cleavage of molecular bonds [28]. The long-term survival of organisms deep within icy moons and in close proximity to high-pressure ices would necessitate strategies akin to those that have evolved in cryo-environments on Earth (e.g. AFPs and AFGPs). These strategies must therefore be compatible with the extreme pressures found in the hydrospheres of icy worlds. This raises an intriguing question: could the growth and recrystallization of exotic ice polymorphs be limited at extreme pressures, bypassing the physical constraints of proteins by using a different type of organic material?

Peptides can provide similar activity to proteins on a much smaller scale. And while most extraterrestrial environments are too dry for proteins to survive, basic peptides can still form in space and on icy worlds [29–31]. In particular, Titan and Europa have both cold surface regions and high-pressure regimes that are thermodynamically favorable for the polymerization of amino acids [31–33]. Such studies are promising when contemplating the potential for life within exobiological habitats. Evidence of a high-pressure IRI mechanism would expand the range for putative extremophile life significantly deeper into the hydrospheres of icy worlds.

Recently, a minimalistic ice-binding peptide (IBP 8, sequence KCCTKNCDSTAHCT) was identified via phage display and found to have IRI activity that mimics AFPs [34]. The

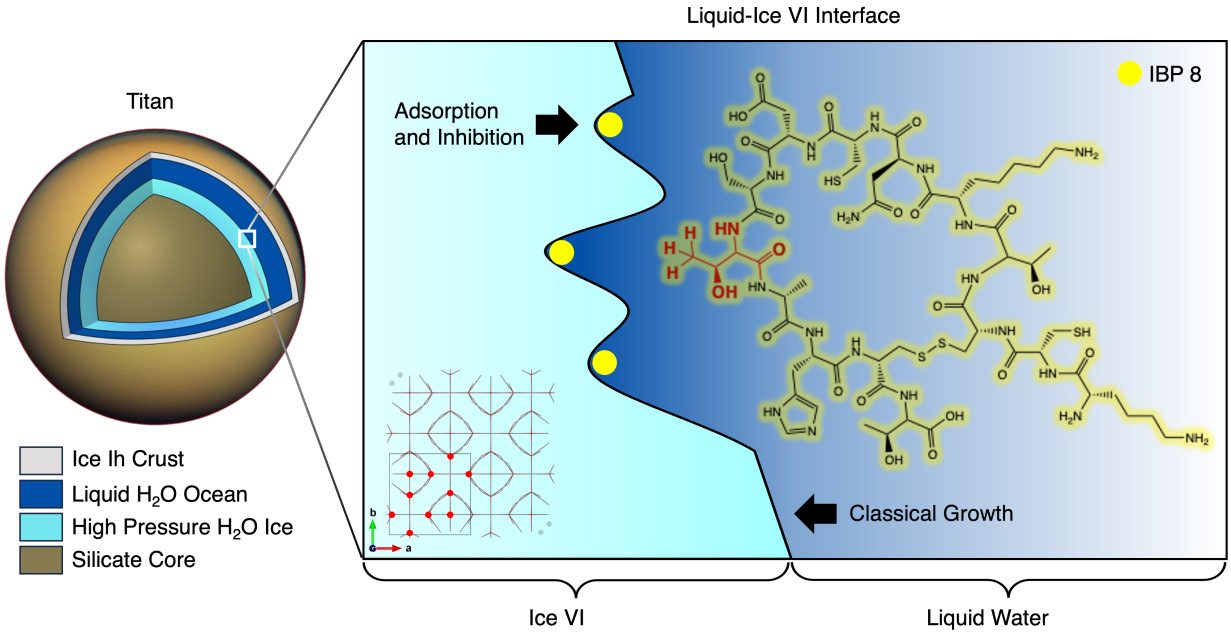

Figure 3.1: A diagram including: the structure of IBP 8, a schematic of IBP 8 binding to and inhibiting the growth of ice VI, and the typical location of ice VI on an icy moon, Titan. The tetrahedral crystal structure of ice VI is given (unit cell oxygen atoms denoted; hydrogen atoms in wire-frame coordination). The primary binding residue of IBP 8 (Thr10) is enlarged for clarity and highlighted in bold red. As opposed to an AFP, IBP 8 is functional with high-pressure ices; this is the upper-limit of sustainability, and the model is equally appropriate under conditions that promote the formation of lower pressure polymorphs, including ice Ih.

mechanism by which IBP 8 impacts crystal growth is foremost reliant on the adsorption of a methyl group from a threonine residue (Thr10) on and into pockets of the primary prismatic ice front [34]. The binding process of IBP 8 is strengthened by torsion around its disulfide bond, changing the conformational space that IBP 8 can occupy. Disulfide bonds are particularly robust and can also tolerate GPa-level pressures, though with some impact on bond distance and torsional angle [35]. IBP 8 is a flexible and resilient candidate for analysis with high-pressure ices (Figure 3.1).

Here, we present a novel series of adapted splat assays at high pressure—nicknamed "squeeze assays"—used to evaluate the impact of IBP 8 on ice VI crystal growth. Ice VI is the highest-pressure water ice polymorph expected on icy worlds within our solar system,

Table 3.1: Sample Information for Squeeze Assays

Sample Name	Solute(s)	Solvent	Pressure (GPa)
0.5 m NaCl	0.5 m NaCl	H_2O	1.1-1.4
Non-ice-binding Peptide	1 mg/mL peptide , 0.5 m NaCl		1.1-1.3
Type III AFP	0.1 mg/mL Type III AFP, 0.5 m NaCl		1.1-1.4
IBP 8	1 mg/mL IBP 8, 0.5 m NaCl		1.2-1.5

and is therefore an appropriate end member for IRI effects in deep hydrospheres [4]. To our knowledge, this is the first-ever investigation of IRI activity against an exotic ice phase and can serve as a template for future evaluations of other materials at high pressures. We also characterize these active ice-binders via multiple high-fidelity MS techniques directly relevant to NASA missions to icy worlds in order to determine both their detectability and potential utility as a new class of molecular biosignature.

3.2 Results

3.2.1 Identification of High-pressure IRI Materials

To identify materials with ice-binding and IRI properties at high pressure, a novel method adapting the splat assay for high-pressure apparatus was developed. The details of and justification for the squeeze assay are provided in the methods section (3.5.1, 3.5.2, 3.5.3).

Evaluation of IRI Activity

Example results of squeeze assays for each solution (table 3.1) are given in Figure 3.2. Squeeze assays, just like splat assays, offer quick and qualitative insights into the ice-binding character of various materials (Figure 3.2). Two types of controls are tested: a pure 0.5 m NaCl solution (positive control) and a 0.5 m NaCl solution with 1 mg/mL non-ice-binding peptide (negative control). Then, two sample solutions are tested: one of 0.1 mg/mL type III AFP, and one of 1 mg/mL IBP 8. Both also contain 0.5 m NaCl. The importance of including a salt or buffer in all samples is crucial, as these prevent false positives for IRI

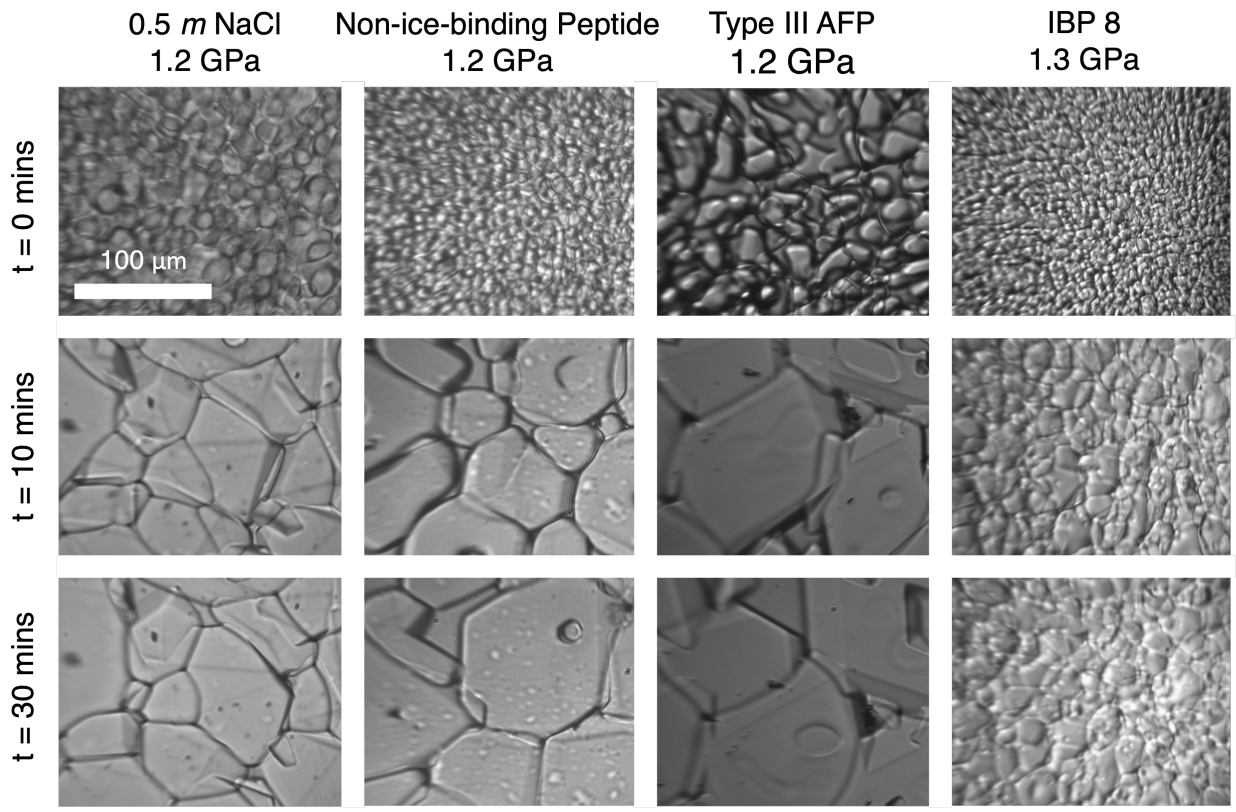

Figure 3.2: Micrographs of squeeze assays for selected experiments up to 30 minutes of ice VI growth. All samples are prepared in chambers of equivalent dimensions to minimize grain boundary overlap and held under static pressure following the onset of crystal growth. Scale bar (top left) is 100 µm and consistent for all micrographs. Sample concentrations are as listed in table 3.1.

assays [36]. Indeed, in dilute solutions, small particles can reside along ice grain boundaries and act as physical blockers for boundary migration. In salt solution, these particles remain trapped within the intercrystalline liquid, and only those with specific IRI character can bind to ice [36]. A concentration of NaCl ten times greater than that of other materials guarantees this effect while appropriately representing the salinity of the oceans on icy worlds [37, 38].

Optical micrographs are reported in Figure 3.2. As expected, ice nucleation occurs heterogeneously at 295 K for all samples upon pressurization just above 1 GPa with grains visually under ∼20 µm. Grain size is then allowed to increase gradually at constant pressure and temperature while in equilibrium with the fluid. Solutions of 0.5 m NaCl, non-ice-binding peptide, and type III AFP seem to evolve in a similar manner (Figure 3.2, three left panels), with grains growing to sizes larger than ∼ 50 µm. Uninhibited recrystallization results in the conglomeration of larger ice VI crystals over time for these three samples (Figure 3.2, top to bottom). Experiments with 0.5 m NaCl provide the baseline grain size for ice VI up to 30 minutes by squeeze assay. Similar growth at each time interval suggests the absence of IRI activity. In direct contrast, solutions of IBP 8 markedly appear to inhibit grain growth with size remaining below ∼ 25 µm after 30 minutes (figure 3.2, right panel).

Grain Segmentation Analysis

Segmentation analysis was performed for all squeeze assays as shown in Figure 3.3. The effect of each material on ice VI recrystallization can be quantified by leveraging the high quality images typical of splat and squeeze assays. Samples were tested in triplicate and evaluated independently for mean largest grain size (MLGS), which is the most common unit when quantifying IRI activity [39]. It is defined as the average length of the longest axis (Feret diameter) of the 10 largest ice grains. The maximum length of every grain identified via segmentation was averaged for each sample and is denoted as mean grain length to provide a secondary mode of analysis.

Grain segmentation was performed using an interactive watershed tool in Fiji (ImageJ) [40]. Since manual corrections are operator-dependent, all analyses have been performed by

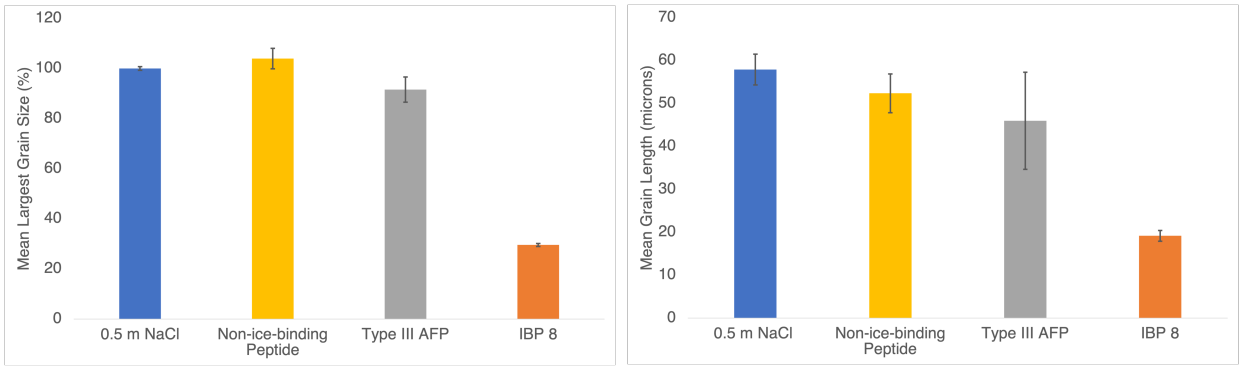

(a)

(b)

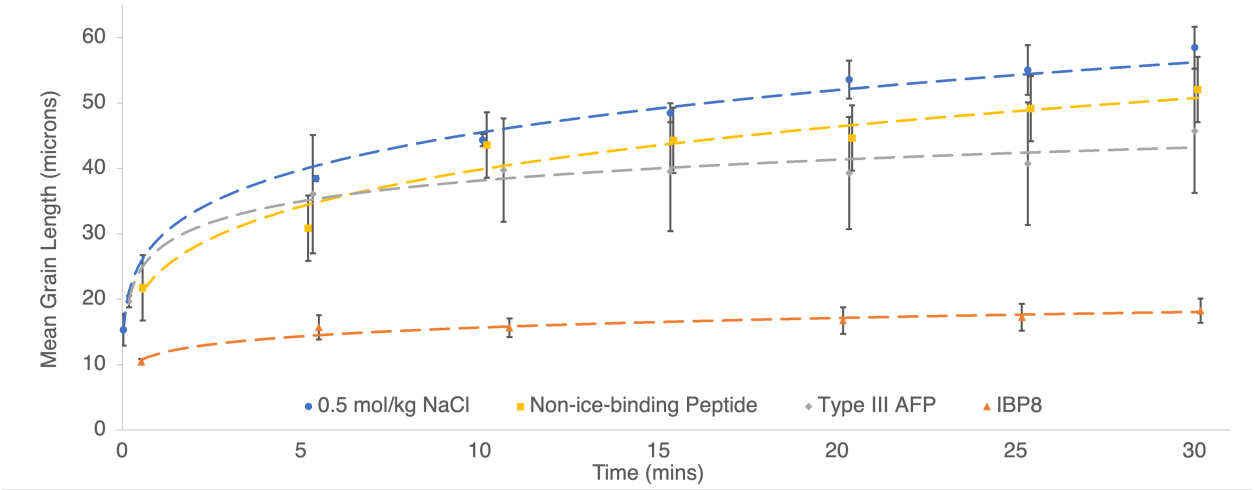

(c)

Figure 3.3: Plots tracking ice VI grains for the panel of samples presented in Figure 3.2 as: (a) mean largest grain size after 30 minutes, reported as a percentage relative to the NaCl control (b) mean grain length after 30 minutes, and (c) mean grain length over time. Error bars denote standard error between experiments in triplicate.

the first author for consistency and to adhere as closely as possible to the standard practices in other studies [39, 41, 42]. The generated segmentation maps are provided in Section A.2.3 as a rough estimate of grain size.

The average MLGS of 0.5 m NaCl solutions after 30 minutes is 114.1 ± 0.9 µm (Figure 3.3, a). This MLGS is the benchmark to which all other solutions are compared. Potent IRI agents are expected to return a MLGS equal to or less than 30% the original value, whereas solutes with negligible IRI activity remain within 80% or the standard error for the control solution [39]. In the case of non-ice-binding peptide and type III AFP, the MLGS is 118.6 ± 4.7 µm and 104.5 ± 5.7 µm, respectively. As both lie well above 80% of the control, the ice VI growth across these solutions is indistinguishable. IBP 8 has a MLGS of 33.7 ± 0.6 µm. This is a 70% reduction in MLGS versus 0.5 m NaCl. The same trend was investigated by mean grain length. Across the squeeze assay panel, mean grain length is 57.9 ± 3.6 µm, 52.4 ± 4.5 µm, 46.0 ± 11.3 µm, and 19.2 ± 1.2 µm from left to right (Figure 3.3, b). Yet again, the impact of non-ice-binding peptide and type III AFP on ice VI growth is insignificant. Whereas, IBP 8 presents a mean grain length of close to 30% of the control value, which is in agreement with the MLGS analysis. Conservatively, IBP 8 is a near-potent or potent recrystallization inhibitor of ice VI.

3.2.2 Characterization of Materials for Biosignature Detection

To characterize IBP 8 as a potential biosignature, mass spectrometry was performed using techniques applicable to the Dragonfly and Europa Clipper missions. Both DraMS-like laser desorption mass spectrometry (LDMS) and Europa Clipper-relevant impact ionization mass spectrometry were used. Analyses were conducted by members of the teams for each instrument at NASA Goddard Space Flight Center and NASA Jet Propulsion Laboratory, respectively. Between both mission-critical modes of analysis, IBP 8 represents—to the best of our knowledge—the largest individual material to produce an MS signal using flight instruments to date.

Laser Desorption Mass Spectrometry

The Dragonfly Mass Spectrometer (DraMS) will be the primary instrument for *in situ* chemical composition analysis on Titan using both laser desorption mass spectrometry (LDMS) and pyrolysis/derivatization-gas chromatography mass spectrometry (pyr/der-GCMS) modes [43, 44]. DraMS-LDMS is a direct sampling technique requiring no sample preparation that can determine the composition of non-volatile organics [44]. LDMS will be the initial measurement mode applied to all samples collected for DraMS chemical analysis [43].

To study the ability of DraMS to detect IBP 8, solutions were analyzed using multiple commercial laser desorption techniques including matrix-assisted laser desorption/ionization mass spectrometry (MALDI-MS), tandem mass spectrometry (MS/MS), and matrix-less LDMS, all performed on a Bruker Autoflex maX time-of-flight MS (ToF MS) system. IBP 8 also underwent controlled degradation at ambient temperature and pressure until a loss of ice binding function was observed (Sections A.1.5, A.2.4, A.2.5). For commercial MS analysis, both fresh IBP 8 and degraded IBP 8 were tested. After commercial MS analysis, fresh IBP 8 was characterized on a DraMS breadboard to determine if any observed chemical structures were common between both techniques. For all MS analysis, initial IBP 8 solutions were prepared by dissolving 1 mg/mL IBP 8 in 0.5 m NaCl to match those tested via squeeze assay (table 3.1).

Analysis of IBP 8 on the commercial LDMS system reveals that IBP 8 is detectable with and without a MALDI matrix (Figure 3.4). Further, a clear difference is observable between fresh and degraded IBP 8 (Figure A.18). Fresh IBP 8 shows some hydrogen incorporation as indicated by the prominent adducts at m/z 1512.5 and m/z 1514.5 (Figure 3.4). The hydrogen and sodium adducts of the molecular ion are detectable via MALDI and LDMS for fresh IBP 8. The ions m/z 1512.4, m/z 1514.5, m/z 1534.5, and m/z 1536.5 were selected from fresh IBP 8 for MS/MS spectra collection to elucidate structural information.

The MS/MS spectrum of target ion m/z 1512.4 is shown in Figure 3.5. Fresh IBP 8 contains many fragment ions consistent with the known peptide sequence (Figure 3.4, table

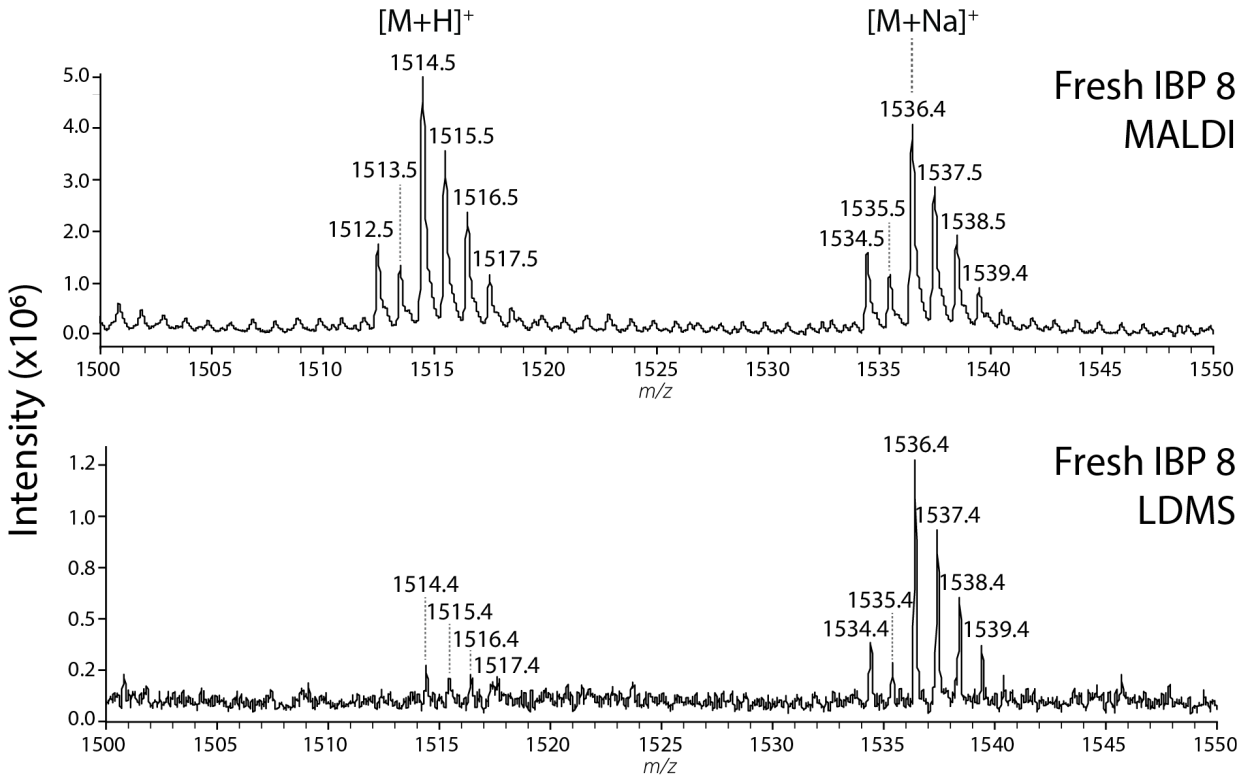

Figure 3.4: Molecular ion adducts of fresh IBP 8 produced with CHCA (MALDI-MS) and without CHCA (LDMS) on a Bruker Autoflex maX. Data indicates that IBP 8 is detectable without a MALDI matrix via LDMS. Hydrogen adducts $[M+H]^+$ and sodium adducts$[M+Na]^+$ of the molecular ion are indicated.

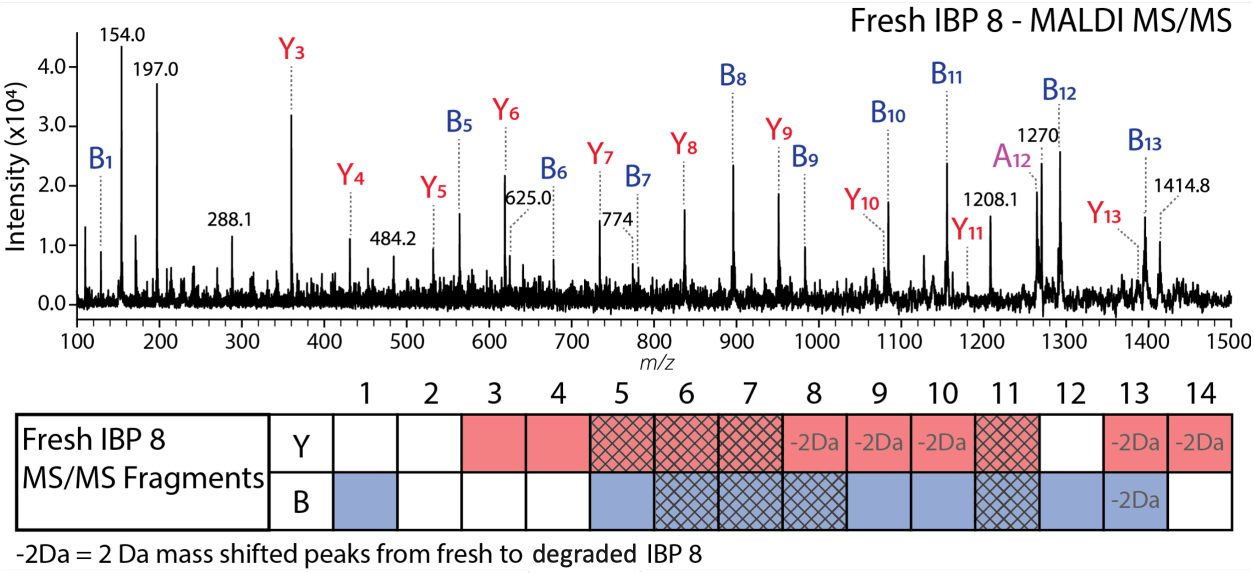

Figure 3.5: Top: MS/MS spectra of fresh IBP 8 collected with a MALDI matrix on m/z 1512.4. B and Y fragment ions are labeled in blue and red, respectively. The A_{12} fragment was also detectable in the fresh spectra (purple). High intensity unidentified ions are also marked for reference. Bottom: B and Y fragment ions observed across all IBP 8 MS/MS analyses. B and Y fragments detectable in fresh IBP 8 are indicated with filled boxes. Fragment ions not detectable in the degraded sample are denoted with hashed boxes. Ions that contain a -2 Da mass shift from the fresh to the degraded sample are also indicated.

A.1). Some but not all fragment ions observable in fresh IBP 8 MS/MS spectra are also detectable with the degraded sample (Figure 3.5). Sodiated and non-sodiated fragment ions are common among both samples (Figure A.19). Of these, many have a -2 Da shift from fresh to degraded IBP 8 (Figure 3.5).

LDMS was conducted using fresh samples on the DraMS LDMS breadboard in order to simulate—as closely as possible—mission-like conditions (see Methods 3.5.4). Notably, IBP 8 fragment ions Y_7 and A_{11} were consistently detectable across multiple analyses (Figure 3.6). Although no molecular ion signal was observed, the presence of these fragment ions indicate that structural information is still available via DraMS-like LDMS analysis.

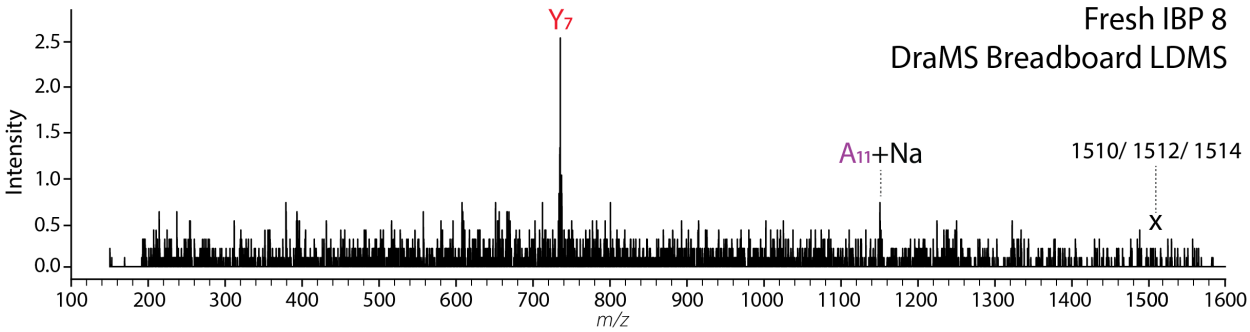

Figure 3.6: DraMS-Like LDMS of fresh IBP 8 drop cast onto a stainless-steel sample stub produce a detectable signal of peptide fragments. Spectrum is an 11 spectra average. Peptide fragment ions Y_7 and A_{11} were detectable across multiple analysis. No molecular ion signal was detectable.

Impact Ionization Mass Spectrometry

To examine the detectability of IBP 8 using a spaceborne dust analyzer—like Cassini's Cosmic Dust Analyzer (CDA) or the SUrface Dust Analyzer (SUDA) on Europa Clipper—IPB 8 was analyzed using a high-fidelity laboratory ice impact ionization MS system approximating ice grain sampling during an ocean world flyby at 4 km/s (Figure 3.7). These conditions fall within the planned encounter velocities for Europa Clipper and other mission concepts proposed for sampling ice grains at ocean worlds [45–48]. To the authors' knowledge, this work represents the first reported impact ionization mass spectrum of an oligopeptide. Several low-mass fragments characteristic of individual amino acid fragmentation patterns are observed, including NH_4^+, CO^+, $CH_2NH_2^+$, CO_2^+, $C_3H_6N^+$, $C_4H_8N^+$, $C_5H_{10}N^+$, $C_2H_{4\text{-}6}NS^+$, and $C_5H_8N_3^+$. Interestingly, the mass spectrum is dominated by immonium ions from lysine and histidine fragmentation ($C_3H_6N^+$, $C_4H_8N^+$, and $C_5H_{10}N^+$, and $C_5H_8N_3^+$, respectively) [49, 50]. This suggests that lysine and histidine side chains may be more prone to impact-induced fragmentation and/or that terminal amino acid residues may be more susceptible to impact-induced fragmentation. However, further work is needed to better elucidate the relationship between amino acid fragmentation and peptide sequence in impact-induced ionization mass spectrometry systems.

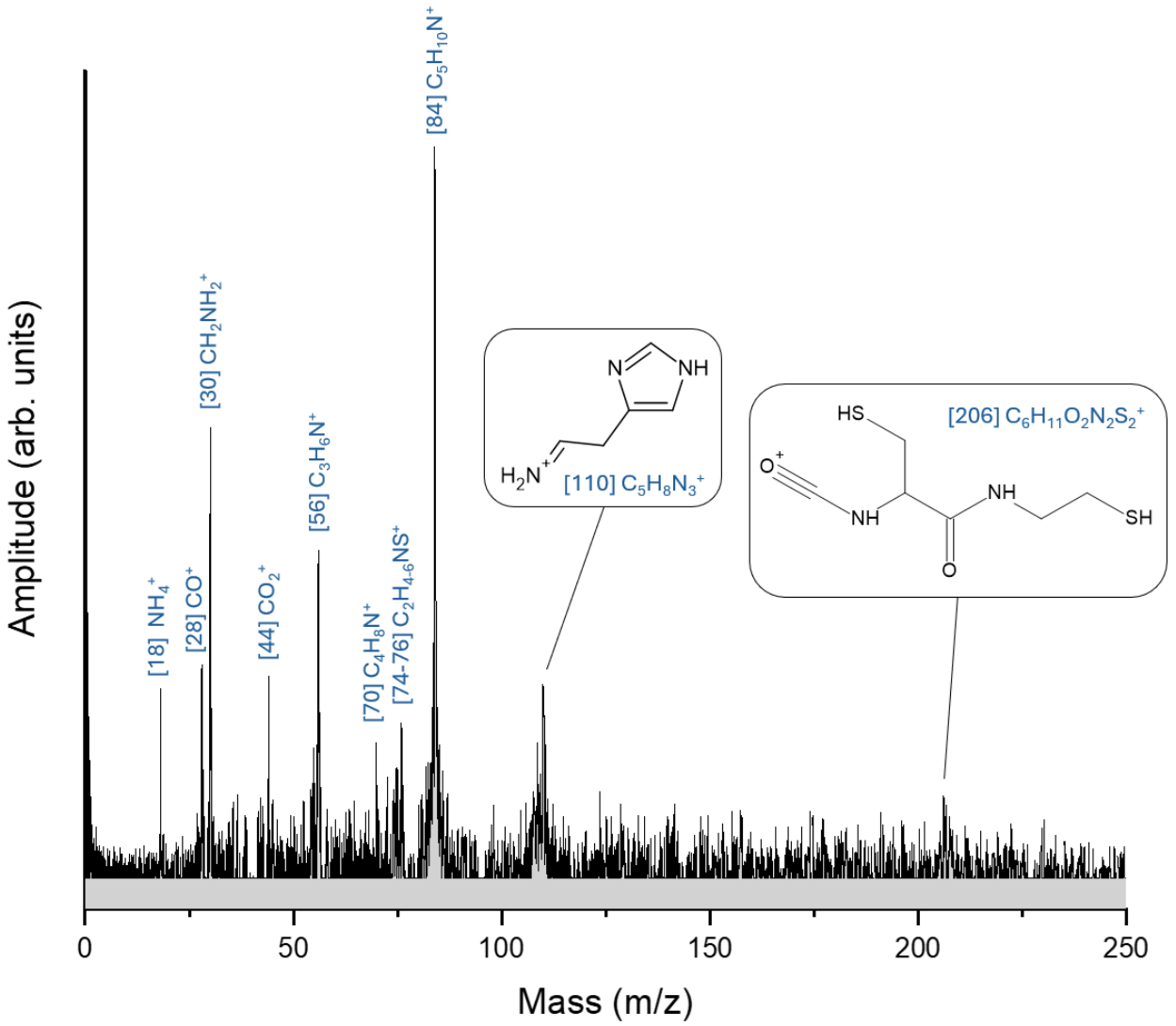

Figure 3.7: Hypervelocity impacts of ice grains containing IBP 8 generate detectable molecular ions that can be sourced to oligopeptide structure and functionality. These data show that molecular ions with information about parent ion molecular structure, even for large organic molecules, may be detectable during an ocean world flyby using a spaceborne impact ionization mass spectrometer. To control for any background contaminant peaks and sodiated/protonated water cluster series present, background subtraction was performed using ice grains generated from an aqueous 10 mM solution at an impact velocity of 4 km/s (raw mass spectra are shown in Figure A.20). Negative data points resulting from subtraction are not shown. IBP 8 mass spectra were collected from the impacts of ice grains generated using an aqueous 30 mM IBP 8 solution at an impact velocity of 4 km/s in cation mode.

In addition to individual amino acid fragments, an IBP 8-specific peptide fragment was observed at 206 m/z. This ion is attributed to the simultaneous fragmentation of the intra-peptide disulfide bond linkage and *b*-type cleavage of the adjacent C-C bond within the cysteine residue on the lysine-terminal side chain. Hypervelocity sampling of ice grains during planetary flybys at > 4 km/s therefore appears sufficient to break the intramolecular disulfide linkages of small peptides and other disulfide-bearing compounds as well. While the relative prominence of low-mass organic fragments (Figure 3.7) is expected due to the high-energy fragmentation resulting from 4 km/s impacts, higher-mass organic fragments may not have been observable due to inherent limitations in the Hypervelocity Ice grain Impact Validation Experiment (HIIVE) instrument sensitivity and mass resolution (see Methods 3.5.5). We note that the SUDA instrument on Europa Clipper is capable of detecting a diverse range of compounds including organics over a concentration range from percent to parts per million (ppm) [16].

3.3 Discussion

3.3.1 Squeeze Assay Implications

The findings via squeeze assay (Figures 3.2 and 3.3) demonstrate the strong ice recrystallization inhibition potency of IBP 8 on ice VI at pressures expected in icy moons like Ganymede, Callisto, and Titan. We also clearly observe a loss of IRI activity for type III AFP at those extreme conditions. The interpretation of these results is discussed hereafter.

Grain size for both control solutions is the same (Figure 3.2, left-half columns). Since type III AFP displays equally large grains, it is not an active ice binder at those conditions (Figure 3.2, right-middle column). While the mechanism of type III AFP at ambient pressure is well known, without performing molecular dynamics (MD) simulations at novel isothermal-isobaric (NpT) ensembles, it is difficult to comment on the exact effect of GPa-level pressures on its ice-binding site [51]. The site is a mostly hydrophobic, flat surface that denatures easily when stressed [52, 53]. In any case, evaluation via squeeze assay confirms that type

III AFP, as a proxy for relatively large macromolecules, does not function under the extreme conditions found on icy worlds. IBP 8, on the other hand, shows a clear reduction in ice VI grain size, both at the onset of crystal growth and over time (Figure 3.2, right-most column). Compared to the protein, IBP 8 is a smaller molecule with a simpler ice-binding mechanism. In tandem, these factors—a cyclic, compact structure that twists to bind with cavities on the ice surface—contribute to its high-pressure viability. IBP 8 remains an active and potent IRI agent against non-hexagonal phases of ice. It is reasonable to expect other pairs of large, life-supporting organics and small, biomimetic counterparts might behave in this manner.

3.3.2 Mass Spectrometry Implications for Peptide Detection

We find that peptides/oligopeptides such as IBP 8 are detectable by commercial MALDI MS, commercial LDMS and DraMS-like LDMS analyses (Figures 3.4, 3.5, and 3.6). IBP 8 molecular ion adducts are present for fresh samples in commercial MALDI and commercial LDMS spectra. Multiple degrees of hydrogenation are also observable in all commercial spectra of fresh IBP 8 as indicated by the presence of the ion series starting at both m/z 1512.5 and m/z 1514.5 (Figure 3.4). The hydrogenation pattern is also observable in IBP 8 sodium adducts (Figure 3.4). These results suggest that mid-sized oligopeptides analyzed on another planetary body via LDMS could produce a distinct ion signal. This signal could be used to help select that ion for MS/MS analysis, a capability of DraMS and potentially other, future spaceflight mass spectrometers [44]. Further, the loss of IBP 8 ice-binding function correlates to differences in MS spectra and MS/MS spectra (Figure 3.5). Many IBP 8 fragment ions from the fresh IBP 8 spectra are also observable in the MS/MS spectra of degraded IBP 8 with a -2 Da mass shift (Figure 3.5) consistent with hydrogen loss.

Because fragment ions of IBP 8 are detectable using DraMS-like LDMS analysis, like materials could be detected via *in situ* LDMS analysis on Titan with the Dragonfly mission, and potentially on other ocean worlds with similar instrumentation. While only IBP 8 fragment ions were detected on the DraMS-LDMS breadboard, IBP 8 molecular ion adducts were ubiquitous using the increased laser fluence available on the commercial LDMS system

($\sim$ 31.83 J/cm^2 on the Bruker system vs. $\sim$ 0.19 J/cm^2 on the DraMS-LDMS breadboard; see Methods 3.5.4). This indicates that an increase in laser power, as is planned for the DraMS flight-LDMS system (up to 0.7 J/cm^2; Mullin et al., 2024 [54]) may produce a higher molecular ion yield of the parent ion that could then be detectable via flight-DraMS LDMS. If detected, the distinct ion patterns observed here for IBP 8 via commercial LDMS could be an indication of a potentially active peptide that could then be targeted for MS/MS analysis for structural determination via *in situ* LDMS (see Li et al., 2017 [55] and Castillo et al., 2023 [56]).

It is also possible that fragmentation of IBP 8 is induced by the LDMS process and would therefore occur on Titan (e.g., Ni et al., 2023 [57]). Peptides can fragment via multiple pathways in LDMS analysis that correlate to different locations along the peptide chain. Controlled peptide fragmentation can be conducted through post-source decay (PSD) and laser induced dissociation (LID) primarily producing *b/y* fragmentation patterns, as observed in the commercial MS/MS spectra (Figure 3.5). Peptide fragmentation can also occur via ultraviolet photodissociation (UVPD; *a/x* fragmentation), collision induced dissociation (CID; *a/b/y* fragmentation), and electron transfer/capture dissociation (ETD/ECD; *c/z* fragmentation). From Figure 3.6 and table A.1, fragment ions Y_{11} and A_{11} are observable in the DraMS-like LDMS spectra. These results are consistent with PSD, LID, UVPD, and CID. Ionization for this analysis on the DraMS-LDMS breadboard is achieved using a 266 nm UV laser irradiation at 30 to 35 Torr. Ions are then directed through a 6 cm long inlet tube through an aperture valve into an ion trap MS for mass analysis and detection [44]. This experimental scheme implies that PSD, LID, UVPD, and CID fragmentation pathways are all plausible. By extension, some degree of peptide fragmentation could also be likely on Titan. The fragmentation patterns observed here do not necessarily eliminate the possibility of a detectable parent ion on Titan. In fact, the relatively high mass of the peptide fragment ions observable via DraMS-like LDMS here would be conducive to MS/MS analysis, providing valuable information on the structure of the peptide. Future work could optimize DraMS-like LDMS analysis with the sole intent to detect and characterize peptides.

Regarding the impact ionization MS results, we show that fragments representing the structure and molecular functionalities of oligopeptides like IBP 8 would also be detectable at flyby speeds planned for future missions to ocean worlds using a spaceborne impact ionization mass spectrometer [16, 45–47]. Although previous work suggests organic molecules may survive hypervelocity impacts at velocities of approximately 4 km/s, the IBP 8 parent ion is currently outside the nominal mass range of laboratory impact ionization mass spectrometers [58, 59]. Therefore, while the IBP 8 parent ion and other potentially large organic fragments may have been formed through impact ionization, these species are not detected. This is likely due to insufficient instrument sensitivity and/or mass resolution, as the ability to detect low-abundance, higher-mass ions is also limited by line broadening effects via the expansion of impact plasma produced during sampling [60]. Modern, high-resolution impact mass spectrometers currently in development for future missions to ocean worlds may circumvent this issue [61], enabling both parent ion characterization and analysis of fragmentation products to better elucidate molecular structure and functionality.

We also find that the spectra generated by impact ionization MS differ from those obtained through LDMS measurements. Many of the ions detected here have been observed previously for individual amino acids, such as NH_4^+, CO_2^+, and immonium fragments of varying chain lengths. This suggests that the deconvolution of signals arising from the fragmentation of peptides and individual amino acids during hypervelocity ice grain sampling may be difficult, though variation of parameters such as flyby velocity may help disambiguate the contributions of fragmentation. Our results do provide evidence that peptide side chain functionality may play a role in molecular fragmentation patterns. However, it is important to note that the impact-induced fragmentation of large organic molecules (including oligopeptides) is currently not well-understood due to the relative novelty of laboratory impact ionization MS systems. Fully understanding the identification of impact-induced organic fragmentation, and how this may relate to overall molecular structure, is a subject of ongoing work and will require further study.

3.3.3 Planetary and Astrobiology Implications

The results presented here provide the first evidence for pressure-tolerant ice recrystallization inhibition (IRI) activity against an exotic high-pressure ice phase. In particular, the growth of ice VI over time is moderated by the oligopeptide IBP 8. This finding holds direct implications for astrobiology and the search for biosignatures on icy ocean worlds. Biosignature frameworks such as the Ladder of Life Detection (Neveu et al., 2018 [62]) and the Confidence of Life Detection (CoLD) scale (Green et al., 2021 [63]) emphasize a progression in confidence of life detection as a function of type and number of biosignature measurements. While environmental conditions in these frameworks are provided to contextualize the survivability and detectability of biosignatures (e.g., degradation or chemical alteration), they do not explicitly include biosignatures that are environment-specific. This may be a significant oversight, as organisms necessarily will evolve adaptations to their unique habitats. Targeting biomolecules or other biologically-generated compounds that modify an environment to confer adaptability to extreme conditions—such as inhibition of ice recrystallization—could provide convincing evidence for the presence of life. And, since the adaptation would be unique to that environment, such a biosignature would also be more robust against questions regarding contamination, especially in conjunction with the detection of a consistent variety of potential cellular materials.

To wit, we argue that a new subtype of biosignature along the Ladder of Life Detection should be defined, one that is environment-specific, reflecting the physicochemical constraints of icy moons [62]. As posited, these biosignatures must be detectable using available or planned spacecraft instrumentation, and in this case represent "molecules and structures conferring function" [62]. IRI peptides like IBP 8 satisfy both requirements. First, its detectability is demonstrated using techniques that are already in flight or in active development for missions such as Dragonfly (LDMS) and Europa Clipper (modeled via impact ionization MS). Second, its role as a compact, structurally resilient IRI agent for both high-pressure and ambient-pressure ice polymorphs offers a realistic survival strategy for life within

high-pressure, ice-dominated environments. It mimics the antifreeze strategies of terrestrial extremophiles while exhibiting resilience under GPa-level pressures well beyond the known functional limits of most proteins. With this study, our knowledge of these antifreeze biosignatures remain limited to one particular oligopeptide. Using the squeeze assay, additional small-to-medium size ($\leq$ 2 kDa) IRI organics could be identified in future work. These ice-binders—following their characterization via mission-relevant MS techniques—could build a library of new potential biosignatures, providing insights into common, structural motifs (such as repeat sequences of threonine or alanine binding residues, or the ideal chain length of polymers) that may differentiate them from materials of similar size but without IRI potency.

3.4 Conclusion

We report the first instance of the peptide IBP 8's IRI activity on a non-hexagonal ice phase at elevated pressures. A novel method for performing high-pressure "squeeze" assays is provided. Results indicate that some ice recrystallization inhibition (IRI) agents are still functional under the extreme conditions of exobiological habitats, opening the door for further research on the potential for pressure-tolerant life-preserving mechanisms elsewhere in the Universe.

To the best of our knowledge, the fragment ions of IBP 8 observed here are the largest peptide signatures containing chemical structural information produced from flight-like or flight-ready LDMS analyses to date. The ability to detect such high-mass peptide ions on the DraMS-LDMS breadboard strongly suggests that peptide signatures could be detectable on Titan, if present at sufficient concentrations. Further, if such relatively high-mass fragment ions or molecular ions were detected on Titan, MS/MS could be used to constrain aspects of chemical structures associated with the potential peptide, such as N- and C-terminal amino acids. Structural information from MS/MS analysis of a peptide signal alone would be strong evidence for the presence of life. Given that the loss of IBP 8 function is observable via mass spectrometry, aging experiments to measure for a potential loss of function of putative peptides within samples collected *in situ* could be envisioned for other planetary

bodies. Such experiments could be monitored with current space flight capabilities including DraMS-like LDMS. Chemical changes consistent with a loss of function observed on another planetary body for a plausible peptide with a known chemical structure, as determined via *in situ* MS/MS, would be another indicator of extant life.

IBP 8 is also the first oligopeptide characterized by impact ionization MS and reported in this manner. While the parent ion was not observed due to instrument limitations, several low-mass fragments were present, including a relatively high-mass fragment attributed specifically to IBP 8. The identification of a unique molecular fragment represents a crucial step forward in our understanding of hypervelocity ice grain sampling at ocean worlds and the feasibility of biosignature detection using flyby architectures. Together, the successful analysis of IBP 8 via MS techniques underscores the importance of multidimensional characterization. Ionization by way of LDMS is relatively soft and permits the detection of large organic fragments including adducts of parent ions. In contrast, impact ionization MS provides detailed structural information through fragments of individual amino acid residues and lower-mass fragments of the peptide chain itself. This is a powerful pathfinder for selecting coordinated and/or follow-up analyses of samples that are challenging to identify with a single methodology. Measurements by different instruments in a payload are helpful for identifying complex organics, and can be particularly useful when considering mid-sized oligopeptides and similar biomolecules.

These findings suggest that simple peptides capable of modifying ice behavior under pressure may serve as plausible, functional biosignatures for subsurface life in ocean worlds. Unlike metabolic byproducts that may diffuse or degrade, ice-binding peptides are expected to adsorb and concentrate at ice grain boundaries, where recrystallization activity is most critical. This natural enrichment at grain boundaries not only enhances their biological function but also increases the likelihood of detection—particularly in expelled or entrained ice grains sampled during plume flybys or surface mixing. As such, their physicochemical behavior under planetary conditions directly supports their habitability relevance.

Defining biosignatures through the lens of planetary environmental constraints not only

improves the specificity of life detection efforts but also broadens the conceptual framework of habitability. By focusing on traits that enhance survival and adaptation in planetary contexts (such as ice modulation under pressure) we can more effectively target molecules that are both accessible to spacecraft-based analysis and grounded in plausible evolutionary pressures. Future biosignature searches should also consider incorporating physico-functional markers such as IRI activity as complementary indicators of habitability and biological adaptation in cryogenic high-pressure environments.

3.5 Methods

3.5.1 Squeeze Assay Sample Information

Relevant sample information is provided in table 3.1. All solutions were prepared by first dissolving NaCl (Certified ACS, Fisher Chemical) into ultra-pure water (Barnstead GenPure xCAD Plus) at 0.5 mol/kg (0.5 m). Secondary lyophilized solutes were chosen to elucidate IRI activity [64]. Type III AFP (A/F Protein Inc., Batch: GOP034-RP0706) was added at 0.1 mg/mL. The chemical purity of the sample was checked by determination of the molar extinction coefficient at 280 nm (1473±27 M^{-1} cm^{-1}, $E_{0.1\%}$ = 0.209±0.004 mg mL^{-1} cm^{-1}) and via circular dichroism (CD) in the far and near ultraviolet (Figures A.1, A.2). Both non-ice-binding oligopeptide (sequence SENEKRIIELMLEMLKHML) and IBP 8 (greater than 50% full sequence, Pierce Custom Peptides) were added at 1 mg/mL. Non-ice-binding peptide was included in the sample panel as a negative control for particles of similar size.

3.5.2 Justification for the Squeeze Assay

Splat assays are typical for probing the IRI activity of various materials [36, 65, 66]. Normally, a 10 µL aliquot of water solution is frozen as a 10 mm by 50 µm ice disc via release onto a chilled (-80 °C) aluminum brick from a height of roughly 2 meters [65]. The disc is then annealed at subzero temperatures to evaluate ice crystal growth over time. As high-pressure experiments take place inside a diamond anvil cell (DAC), the splat assay method is adapted.

The outlined procedure—albeit constrained by the equipment available—adheres to the same general principles. Water droplet size is still uniform, though significantly smaller, limited by the installed culet diameter (circa 400 µm). Rather than being flash-frozen on a cold surface, the sample is squeezed under hydrostatic pressure and crystallized directly into the appropriate phase. Growth is monitored optically following ice formation; though, the annealing pressure varies depending on chamber volume and sample composition (table 3.1). Despite these differences, the growth of fine ice grains is observable, and smaller ice crystal sizes can still be used to quantify IRI activity. The resulting squeeze assay methodology is standardized, easily reproducible, and consistent across all experiments of equivalent design.

3.5.3 Squeeze Assay and Grain Analysis

Squeeze assays were performed in a Merrill Bassett-style diamond anvil cell (MDAC) with 700 µm diameter, type IIas culets. Rhenium gaskets were dimpled to a minimum thickness of 55 µm. A high-pressure chamber was formed by drilling a 400 µm diameter hole centered above the dimpled area using a Micro EDM from Hylozoic Products. Ruby chips were placed into the chamber and were used as pressure sensors [67, 68]. Otherwise, sample pressure was determined via diamond Raman scattering [69]. Aqueous samples were quickly loaded and sealed to avoid evaporation, and solutions were not observed to react with the gasket material. The pressure was manually increased at ambient temperature until the rapid onset of ice VI crystal growth. Once crystal growth was observed, the pressure was held constant for the remainder of the experiment.

Images, photoluminesence (PL), and Raman spectra accompanying squeeze assays were collected on a locally-built optical setup. See Section A.1.1 for more details. Sample alignment and visualization was achieved using a 10X Mitutoyo Plan Apochromat long-working distance objective lens (0.28 NA), an integrated IDS Imaging Color CMOS camera, and a white fiber light source. Images were captured at minute-long time intervals up to 30 minutes for every experiment. Image analysis was performed in Fiji (ImageJ) using the Interactive-H-Watershed plugin. Watershed is an efficient tool for segmentation [40]. A pixel to distance

ratio calibration was performed individually for each image. Backgrounds were carefully removed to minimize the detection of false grains during the segmentation process. Mapping was done manually for all images. Following segmentation, data sets for each image were generated in Fiji (ImageJ), and grain size was estimated via Feret's diameter (max caliper). Values for mean grain length were averaged for each sample solution in triplicate. MLGS calculations were performed by hand for each image.

3.5.4 Laser Desorption/Ionization Mass Spectrometry

For all laser desorption MS analysis, previously produced IBP 8 solutions were used (1 mg/mL IBP 8 in 0.5 M NaCl). Fresh IBP 8 samples were frozen at -20 °C prior to MS analysis. Information on controlled degradation can be found in Sections A.1.5 and A.2.4. For MS analysis, samples were melted, vortexed for one minute, and then 1-4 µL of solution was spotted onto analytical substrates and dried for one hour prior to analysis. For MALDI analysis of both fresh and degraded IBP 8, IBP 8 solutions were mixed with the matrix α-Cyano-4-hydroxycinnamic acid (CHCA) at a 1:1 (v/v) ratio prior to deposition. Cleaned MALDI sample plates (3x sequential rinse in acetone, isopropyl alcohol, and methanol) were used as analytical substrates for MALDI and commercial LDI analysis. For DraMS-like LDMS, custom stainless-steel substrates were washed in lab detergent, sonicated for three hours in DI water, and then sonicated for 10 minutes each in acetone, isopropyl alcohol, and methanol before being vacuum-baled at 250 °C for 12 hours. Additionally, a cleaned wire mesh (washed in lab detergent, triple-rinsed in DI water, and then ashed at 500 °C for 12 hours) was used with the DraMS-like LDMS substrates to maintain sample heterogeneity across the substrate.

IBP 8 was analyzed via commercial MALDI-MS analysis, MALDI-MS/MS, and matrix-less LDMS on a Bruker Autoflex maX MALDI-ToFMS system. The Bruker Autoflex maX induces ionization with the Bruker Smartbeam-II, a 355 nm Nd:YAG laser that operates at up to 2000 Hz (200 Hz in ToF/ToF mode). The maximum laser fluence of the Bruker Autoflex maX laser is $\sim$ 31.83 J/cm^2 (Bruker Daltonik, internal communication). All commercial

MALDI and LDMS spectra were collected in positive ion mode scanning 0 to 2000 Da. MS/MS spectra were collected for IBP 8 molecular ions including m/z 1510, m/z 1512, m/z 1514, m/z 1532, m/z 1534, m/z 1536 when observable. For commercial MS analysis, five replicates of each sample were spotted onto MALDI plates and at least 3 locations in each spot were analyzed and averaged to create each mass spectrum.

LDMS analysis conducted on the DraMS-LDMS breadboard were designed to closely simulate flight-like DraMS LDMS analysis. Laser desorption and ionization would be achieved using a 266 nm Nd:YAG laser with a $\sim$ 2 ns pulse duration and a focal spot size of $\sim$ 50 $\times$ 100 µm [44]. DraMS-type LDMS analysis induces minimal damage to material outside of the laser focal spot enabling repeated analyses on the same sample [70]. As previously optimized, laser desorption was performed using 30 µJ per pulse (fluence of $\sim$ 0.19 J/cm^2) and 5 laser pulses per spectrum at 30 Torr established by a gas mixture matching the atmospheric composition of Titan (95% N_2, 5% CH_4). Ions produced via LDMS were directed into an ion trap mass spectrometer (ITMS) [44]. The DraMS breadboard ITMS was operated in positive ion polarity mode with two separate scanned mass ranges of 80 to 1000 Da and $\sim$ 140 to 1600 Da. For DraMS-like LDMS, three sample stubs were spotted with IBP 8 and more than five locations were analyzed across each substrate.

3.5.5 Impact Ionization Mass Spectrometry

Fresh IBP 8 samples were frozen at -20 °C and dissolved at a 30 mM concentration in water. Water was purified to an 18.2 MΩ-cm resistivity using a Milli-Q IQ 7005 Ultrapure and Pure Water Purification System (MilliporeSigma). Samples were analyzed directly using impact MS without further processing. Cation impact mass spectra were collected using the Hypervelocity Ice grain Impact Validation Experiment (HIIVE), a laboratory hypervelocity ice grain impact mass spectrometer that approximates the flyby sampling of ocean world ice grains by a spaceborne dust analyzer. The experimental method is described in brief (and in more detail in Seaton et al., 2025 [59]); water droplets traveling at a distribution of speeds as high as 4.5 km/s are generated through the laser-induced dispersion (Opolette HE 2940

nm, Opotek; 20 Hz, 5-7 ns pulse length) of a micron-sized water jet (Advanced Microfluidic Systems GmbH) in vacuum. These droplets freeze under high vacuum conditions, forming ice grains. The ice grains then impact a metal target, producing an impact plasma containing ions and molecular fragments which are analyzed directly using an orthogonal reflectron time-of-flight mass spectrometer (Jordan TOF Products, Inc.) akin to Cassini's CDA or the Clipper's SUDA, in either cation or anion mode. For the analysis, 1 mL of sample was injected through a syringe filter (pore size 0.45 µm) using a Luer Lock syringe. The resulting waveforms were exported as raw .csv files and processed using Origin 2020b software. Mass calibration was performed empirically using well-known Na^+ cluster sequences generated from aqueous 0.1 M NaCl solutions. Background subtraction was performed with mass spectra collected using ice grains generated from an aqueous 10 mM NaCl solution. All impact mass spectra represent an average of 512 individual spectra collected under identical conditions in cation mode. Each averaged mass spectrum was treated with a Savitzky-Golay filter and baseline corrected.

3.6 Acknowledgments and Supplementary Information

A portion of this research was carried out at the Jet Propulsion Laboratory, California Institute of Technology, under a contract with the National Aeronautics and Space Administration (80NM0018D0004).

M. Joseph Pasterski's (or M.J.P.'s) research was supported by an appointment to the NASA Postdoctoral Program at the Goddard Space Flight Center, administered by Oak Ridge Associated Universities under contract with NASA. The authors wish to thank the NASA New Frontiers Program and Dragonfly Mission for funding. The Dragonfly Mission is managed by the Johns Hopkins Applied Physics Laboratory under contract to the Planetary Missions Program Office at Marshall Space Flight Center (MSFC) under contract NNN06AA01C. The authors would also like to thank Volker Sauerland and Thilani Anthony at Bruker Daltonics for their guidance in developing methods for MALDI analysis.

C.E.W. (the author) acknowledges that part of this work was completed using instruments

offered by the Spectroscopic and Analytical Instrumentation Facility at the UW Department of Chemistry, with the generous assistance of Brandon Bol and Martin Sadilek, PhD. These instruments are funded partially by the UW student technology fee. C.E.W. also thanks Amijai Saragovi, post doctoral scholar in the Baker Lab at the UW Institute of Protein Design, for sharing non-ice-binding peptide materials.

The idea of testing antifreeze proteins for their effects on high-pressure ice growth was initially proposed by Prof. Peter Pauzauskie (P.J.P.). He also contributed to the early conceptualization of the high-pressure splat assay, namely examining the impact of IBP 8 and non-ice-binding peptide on the recrystallization of cubic ice VII. P.J.P. coordinated the initial collaboration with Prof. Tobias Weidner.

Preliminary development not presented in this dissertation—done by C.E.W. and advised by P.J.P.—had the financial support of P.J.P. vis-à-vis the U.S. Department of Energy, Office of Science (DOE) Basic Energy Sciences (BES) Synthesis and Processing Science, FWP 67554. Additional experimental and materials funding from P.J.P. at that time is acknowledged from the National Science Foundation Materials Research Science & Engineering Center (DMR-1719797), the University of Washington's Molecular Engineering & Sciences Institute, and Institute for Nano-Engineered Systems.

C.E.W. acknowledges Prof. Baptiste Journaux (B.J.) for his support, provision of chemical materials and laboratory resources, and guidance during the redesign of the preliminary high-pressure splat assay since June 2024. All squeeze assay data presented herein were collected under the day-to-day supervision of B.J. and were gathered and analyzed with financial support from the UW Chemistry department and the UW Earth and Space Science department. C.E.W. also acknowledges support from the NASA Astrobiology Institute through the Titan and Beyond node (17-NAI82–17) and the NASA Precursor Science Investigations for Europa grant (22-PSIE22_2–0024) awarded to Baptiste Journaux.

Supplementary information can be found in Appendix A.

References

1. Fletcher, N. H. *The Chemical Physics of Ice* (Cambridge University Press, 1970).
2. Des Marais, D. J. *et al.* Remote Sensing of Planetary Properties and Biosignatures on Extrasolar Terrestrial Planets. *Astrobiology* **2,** 153–181 (2004).
3. Vance, S. D. *et al.* Geophysical Investigations of Habitability in Ice-Covered Ocean Worlds. *J. Geophys. Res. E: Planets* **123,** 180–205 (2018).
4. Journaux, B. *et al.* Large Ocean Worlds with High-Pressure Ices. *Space Sci. Rev.* **216,** 7 (2020).
5. Styczinski, M. J., Vance, S. D. & Melwani Daswani, M. PlanetProfile: Self-Consistent Interior Structure Modeling for Ocean Worlds and Rocky Dwarf Planets in Python. *Earth Space Sci.* **10,** e2022EA002748 (2023).
6. Nimmo, F. & Pappalardo, R. T. Ocean worlds in the outer solar system. *J. Geophys. Res. E: Planets* **121,** 1378–1399 (2016).
7. National Academies of Sciences, Engineering, and Medicine. *Origins, Worlds, and Life: Planetary Science and Astrobiology in the Next Decade* (The National Academies Press, 2023).
8. Lammer, H. *et al.* What makes a planet habitable? *Astron. Astrophys. Rev.* **17,** 181–249 (2009).
9. McKay, C. P., Anbar, A. D., Porco, C. & Tsou, P. Follow the Plume: The Habitability of Enceladus. *Astrobiology* **14,** 352–355 (2014).
10. Cable, M. L. *et al.* The Science Case for a Return to Enceladus. *Planet. Sci. J.* **2,** 132 (2021).
11. Vance, S. D. *et al.* Investigating Europa's Habitability with the Europa Clipper. *Space Sci. Rev.* **219,** 81 (2023).

12. Lunine, J. I., Cable, M. L., Hörst, S. M., Rahm, M. & Dotson, R. in *Planetary Astrobiology* (eds Meadows, V. S., Arney, G. N., Schmidt, B. E. & Des Marais, D. J.) 247–266 (University of Arizona Press, 2020).

13. Seaton, K. M., Cable, M. L. & Stockton, A. M. Analytical Chemistry Throughout This Solar System. *Annu. Rev. Anal. Chem.* **15,** 197–219 (2022).

14. Marshall, S. M. *et al.* Identifying molecules as biosignatures with assembly theory and mass spectrometry. *Nat. Commun.* **12,** 3033 (2021).

15. Chou, L. *et al.* Planetary Mass Spectrometry for Agnostic Life Detection in the Solar System. *Front. Astron. Space Sci.* **8** (2021).

16. Kempf, S. *et al.* SUDA: A SUrface Dust Analyser for Compositional Mapping of the Galilean Moon Europa. *Space Sci. Rev.* **221,** 10 (2025).

17. Becker, T. M. *et al.* Exploring the Composition of Europa with the Upcoming Europa Clipper Mission. *Space Sci. Rev.* **220,** 49 (2024).

18. Lorenz, R. D. *et al.* Selection and Characteristics of the Dragonfly Landing Site near Selk Crater, Titan. *Planet. Sci. J.* **2,** 24 (2021).

19. Barnes, J. W. *et al.* Science Goals and Objectives for the Dragonfly Titan Rotorcraft Relocatable Lander. *Planet. Sci. J.* **2,** 130 (2021).

20. MacKenzie, S. M. *et al.* Science Objectives for Flagship-Class Mission Concepts for the Search for Evidence of Life at Enceladus. *Astrobiology* **22,** 685–712 (2022).

21. Malaterre, C. *et al.* Is There Such a Thing as a Biosignature? *Astrobiology* **23,** 1213–1227 (2023).

22. Sun, S., Ding, H., Wang, D. & Han, S. Identifying Antifreeze Proteins Based on Key Evolutionary Information. *Front. Bioeng. Biotechnol.* **8** (2020).

23. Voets, I. K. From ice-binding proteins to bio-inspired antifreeze materials. *Soft Matter* **13,** 4808–4823 (2017).

24. Oude Vrielink, A. S., Aloi, A., Olijve, L. L. C. & Voets, I. K. Interaction of ice binding proteins with ice, water and ions. *Biointerphases* **11,** 018906 (2016).

25. Olijve, L. L. C. *et al.* Blocking rapid ice crystal growth through nonbasal plane adsorption of antifreeze proteins. *PNAS* **113,** 3740–3745 (2016).

26. Sharma, A. *et al.* Microbial Activity at Gigapascal Pressures. *Science* **295,** 1514–1516 (2002).

27. Meersman, F. *et al.* High-Pressure Biochemistry and Biophysics. *Rev. Mineral. Geochem.* **75,** 607–648 (2013).

28. Chen, W.-Q. *et al.* Effects of Gigapascal Level Pressure on Protein Structure and Function. *J. Phys. Chem. B* **116,** 1100–1110 (2012).

29. Seddon, G. M. & Bywater, R. P. The fate of proteins in outer space. *Int. J. Astrobiol.* **16,** 19–27 (2010).

30. Krasnokutski, S. A. *et al.* Formation of extraterrestrial peptides and their derivatives. *Sci. Adv.* **10,** eadj7179 (2024).

31. Kimura, J. & Kitadai, N. Polymerization of Building Blocks of Life on Europa and Other Icy Moons. *Astrobiology* **15,** 430–441 (2015).

32. Vance, S. *et al.* Hydrothermal systems in small ocean planets. *Astrobiology* **7,** 987–1005 (2007).

33. Ying, J. *et al.* Effect of high hydrostatic pressure on prebiotic peptide synthesis. *Chin. Chem. Lett.* **30,** 367–370 (2019).

34. Stevens, C. A. *et al.* A minimalistic cyclic ice-binding peptide from phage display. *Nat. Commun.* **12** (2021).

35. Moggach, S. A., Allan, D. R., Parsons, S., Sawyer, L. & Warren, J. E. The effect of pressure on the crystal structure of hexagonal l-cystine. *J. Synchrotron Radiat.* **12,** 598–607 (2005).

36. Knight, C. A., Wen, D. & Laursen, R. A. Nonequilibrium Antifreeze Peptides and the Recrystallization of Ice. *Cryobiology* **32,** 23–34 (1995).

37. Journaux, B., Daniel, I., Caracas, R., Montagnac, G. & Cardon, H. Influence of NaCl on ice VI and ice VII melting curves up to 6 GPa, implications for large icy moons. *Icarus* **226,** 355–363 (2013).

38. Frank, M. R., Aarestad, E., Scott, H. P. & Prakapenka, V. B. A comparison of ice VII formed in the H_2O, NaCl–H_2O, and CH_3OH–H_2O systems: Implications for H_2O-rich planets. *Phys. Earth Planet. Inter.* **215,** 12–20 (2013).

39. Delesky, E. A. & Srubar, W. V. Ice-binding proteins and bioinspired synthetic mimics in non-physiological environments. *iScience* **25** (2022).

40. Vincent, L. & Soille, P. Watersheds in digital spaces: an efficient algorithm based on immersion simulations. *IEEE Trans. Pattern Anal. Mach. Intell.* **13,** 583–598 (1991).

41. Journaux, B. *et al.* Recrystallization processes, microstructure and crystallographic preferred orientation evolution in polycrystalline ice during high-temperature simple shear. *The Cryosphere* **13,** 1495–1511 (2019).

42. Mitchell, D. E., Lovett, J. R., Armes, S. P. & Gibson, M. I. Combining Biomimetic Block Copolymer Worms with an Ice-Inhibiting Polymer for the Solvent-Free Cryopreservation of Red Blood Cells. *Angew. Chem. Int. Ed.* **55,** 2801–2804 (2016).

43. Trainer, M. G. *et al. Dragonfly: Investigating the Surface Composition of Titan* 2018.

44. Grubisic, A. *et al.* Laser Desorption Mass Spectrometry at Saturn's moon Titan. *Int. J. Mass Spectrom.* **470,** 116707 (2021).

45. Seaton, K. M. *et al.* Astrobiology eXploration at Enceladus (AXE): A New Frontiers Mission Concept Study. *Planet. Sci. J.* **4,** 116 (2023).

46. Campagnola, S. *et al.* Tour Design Techniques for the Europa Clipper Mission. *J. Guid. Control Dyn.* **42,** 2615–2626 (2019).

47. Reh, K. *et al. Enceladus Life Finder: The search for life in a habitable Moon* 2016.

48. Cangahuala, L. A. *et al.* Europa Clipper Mission Design, Mission Plan, and Navigation. *Space Sci. Rev.* **221,** 22 (2025).

49. Meißner, R. *et al.* Positive and negative ions of the amino acid histidine formed in low-energy electron collisions. *J. Mass Spectrom.* **54,** 802–816 (2019).

50. Xue, G., Liu, Z., Wang, L. & Zu, L. The role of basic residues in the fragmentation process of the lysine rich cell-penetrating peptide TP10. *J. Mass Spectrom.* **50,** 220–227 (2015).

51. Verreault, D. *et al.* Ice-binding site of surface-bound type III antifreeze protein partially decoupled from water. *Phys. Chem. Chem. Phys.* **20,** 26926–26933 (2018).

52. Sönnichsen, F. D., DeLuca, C. I., Davies, P. L. & Sykes, B. D. Refined solution structure of type III antifreeze protein: hydrophobic groups may be involved in the energetics of the protein–ice interaction. *Structure* **4,** 1325–1337 (1996).

53. Kundu, S. & Roy, D. Temperature-induced unfolding pathway of a type III antifreeze protein: Insight from molecular dynamics simulation. *J. Mol. Graphics Modell.* **27,** 88–94 (2008).

54. Mullin, M. W. *et al. Performance of the dragonfly mass spectrometer (DraMS) programmable UV laser source engineering test unit (ETU)* in *Solid State Lasers XXXIII: Technology and Devices* (eds Clarkson, W. A. & Shori, R. K.) **12864** (SPIE, 2024), 1286409.

55. Li, X. *et al.* Mars Organic Molecule Analyzer (MOMA) laser desorption/ionization source design and performance characterization. *Int. J. Mass Spectrom.* **422,** 177–187 (2017).

56. Castillo, M. *et al.* Linear Ion Trap Mass Spectrometer (LITMS) Instrument Field and Laboratory Tests as Part of the ARADS Field Campaigns. *Astrobiology* **23,** 1337–1347 (2023).

57. Ni, Z. *et al.* Detection of Short Peptides as Putative Biosignatures of Psychrophiles via Laser Desorption Mass Spectrometry. *Astrobiology* **23,** 657–669 (2023).

58. Burke, S. E., Auvil, Z. A., Hanold, K. A. & Continetti, R. E. Detection of intact amino acids with a hypervelocity ice grain impact mass spectrometer. *PNAS* **120,** e2313447120 (2023).

59. Seaton, K. M. *et al. Replicating the flyby sampling of salty ocean world ice grains using impact ionization mass spectrometry* 2025. arXiv: `2508.10169 [astro-ph.EP]`. `https://arxiv.org/abs/2508.10169`.

60. Mocker, A. *Comparison of impact ionisation plasma with laser ionisation* PhD thesis (Ruprecht Karl University of Heidelberg, 2010).

61. Kempf, S. *et al. Sniffing the Enceladus Plume: The High Ice Flux Instrument (HIFI) Compositional Analyzer* 2025.

62. Neveu, M., Hays, L. E., Voytek, M. A., New, M. H. & Schulte, M. D. The Ladder of Life Detection. *Astrobiology* **18,** 1375–1402 (2018).

63. Green, J. *et al.* Call for a framework for reporting evidence for life beyond Earth. *Nature* **598,** 575–579 (2021).

64. Biggs, C. I. *et al.* Mimicking the Ice Recrystallization Activity of Biological Antifreezes. When is a New Polymer "Active"? *Macromol. Biosci.* **19,** e1900082 (2019).

65. Knight, C. A., Hallett, J. & DeVries, A. L. Solute effects on ice recrystallization: An assessment technique. *Cryobiology* **25,** 55–60 (1988).

66. Capicciotti, C. J., Doshi, M. & Ben, R. N. *Ice Recrystallization Inhibitors: From Biological Antifreezes to Small Molecules* (IntechOpen, 2013).

67. Shen, G. *et al.* Toward an international practical pressure scale: A proposal for an IPPS ruby gauge (IPPS-Ruby2020). *High Pressure Res.* **40,** 299–314 (2020).

68. Datchi, F. *et al.* Optical pressure sensors for high-pressure–high-temperature studies in a diamond anvil cell. *High Pressure Res.* **27,** 447–463 (2007).

69. Akahama, Y. & Kawamura, H. Pressure calibration of diamond anvil Raman gauge to 310 GPa. *J. Appl. Phys.* **100,** 043516 (2006).

70. Li, X. *et al.* Detection of Trace Organics in Mars Analog Samples Containing Perchlorate by Laser Desorption/Ionization Mass Spectrometry. *Astrobiology* **15,** 104–110 (2015).

Chapter 4

ON THE MELTING CURVES OF WATER AT PRESSURE AND IN THE PRESENCE OF SALTS EXPECTED IN ICY WORLDS

The icy, ocean worlds of the outer solar system are exciting astrobiological targets, some of which will be explored by launched and planned space missions of the upcoming decade.[1] The hydrospheres of these large moons host oceans in equilibrium with ice polymorphs at pressures significantly greater than those similarly found on Earth. They also are expected to contain fractions of dissolved inorganic salts and organic volatiles, including NaCl, $MgSO_4$, Na_2SO_4, and $MgCl_2$. This presents unique challenges for modeling the interiors of icy worlds. While the phase diagram of water is well known, the broad impact of solutes on the melting curves of water at high pressures remains a topic of interest—the majority of salt-water phase diagrams are limited in scope, quantifying freezing-point depressions and eutectics at atmospheric pressures only. Some aqueous salt systems at unique pressure-temperature conditions have already been characterized; however, there are significant gaps in the current literature. Here, the melting curves of ordinary ice Ih and tetragonal ice VI with respect to $MgSO_4$, Na_2SO_4, and $MgCl_2$ are investigated from 230 to 320 K and up to 1400 megapascals (MPa). These data are used to extrapolate surfaces representing the liquidus of ice VI at any applicable pressure, temperature, and concentration of these common salts to three molal (mol/kg, m). The liquidus of ice Ih versus $MgCl_2$ is also mapped. Individual melting curves are compared to an ideal solution model, by which the upper limit of ideal or near-ideal behavior at high pressure is reported, with implications on the estimation of freezing point depressions in the presence of simple solutes. This work is a major advancement in the provision of fundamental thermodynamic data for aqueous salt equilibria.

[1]This chapter is the author's original experimental work, with conceptual planning, guidance, and assistance from Prof. Baptiste Journaux.

To clarify: the following contains enough data to constitute a full-length publication. While we plan on submitting such a publication in the near future, this chapter is the first attempt at presenting the project and is within the scope of experiments performed by the author exclusively at UW, without any external collaboration.

4.1 Introduction

The determination of melting curves and the thermodynamics of solutions has a storied history tracing back to the lauded chemists and physicists of the late-18th to mid-19th centuries [1]. In 1788, Sir Charles Blagden was the first to scientifically document the freezing point depression of dissolved and bulk solids on water. His experiments, inspired by the solidification of quicksilver—what is now called mercury—at low temperatures, involved the dissolution of snow, common salt, and mud in water either distilled or freshly sourced from pumps and waterways in the London area [2]. Nearly a full century later, in 1882, François-Marie Raoult expanded greatly upon these findings. After evaluating over 60 mineral species in water and five other organic solvents, a "general law of freezing" was determined: for every one mole of solute dissolved in 100 moles of solvent, the freezing point is depressed by about 0.62 °C [3]. Raoult, unable to explain the multiplicative effects of salts in water, instead reduced their impact by three to match the law for organics—coincidentally, three times 0.62 °C is 1.86 °C, the same value for the empirical molal freezing-point constant of water [4]. His research was further clarified by Svante Arrhenius in 1883, and its impact has persisted to the present day [1, 5]. Solutions conforming to Raoult's law, whereby changes in their properties are directly and exclusively proportional to the number of molecules of dissolved materials, are considered ideal.

In thermodynamic terms, the ideal behavior of solutions assumes that there is no molecular interaction between components (i.e. no solvation) in solution. As such, the enthalpy of mixing $\Delta_{\text{mix}}H$ is zero. Combining substances always increases disorder, and so the change

in entropy of a two-component system is:

$$\Delta_{\text{mix}}S = -nR(x_A \ln x_A + x_B \ln x_B) \tag{4.1}$$

where n is the total number of moles, R is the ideal gas constant (8.314 J/mol·K), and x_A and x_A are the mole fractions of components A and B, respectively, which always sum to one [4]. The ideality, or rather the lack thereof, at increasing concentrations of various aqueous inorganic salts has already been abundantly documented at one bar. More specifically, the freezing point depression of salts—a colligative property for dilute solutions—is given based on parts of their binary system phase diagrams (see Appendix B for temperature-concentration phase diagrams of relevant salt solutions). These can be compared to the expected depression for ideal solutions at the same concentrations of salt (Figure 4.1). Deviations from the ideal line occur almost immediately, and opposite trends are observed for sulfates and chlorides. This is not entirely unexpected, as solvation effects are omitted from the derivation of the freezing point depression from the ideal model:

$$\Delta T_f = K' x_B \quad \text{and} \quad K' = \frac{RT^{*2}}{\Delta_{\text{fus}}H} \tag{4.2}$$

where x_B is the mole fraction of the solute B, R is the gas constant, and T^* and $\Delta_{\text{fus}}H$ are the freezing temperature (K) and enthalpy of fusion of the pure solvent, respectively [4]. While the identity of the solvent has a direct impact on the freezing point depression in (4.1), the identity of the solute does not. The assumption—that solute and solvent molecules have no meaningful, energetic interactions with one another—fails, particularly as the concentration of solute increases. In general, higher effective concentrations of ions disproportionately affect the formation of ice crystal lattices, requiring lower temperatures to nucleate the same amount of ice as compared to pure water. Sulfates tend to be less soluble than chlorides and have a correspondingly weaker impact on the melting curve. This is partially due to ion-pairing interactions between sulfate anions ($SO_4{}^{2-}$) and cations that reduce the percentage

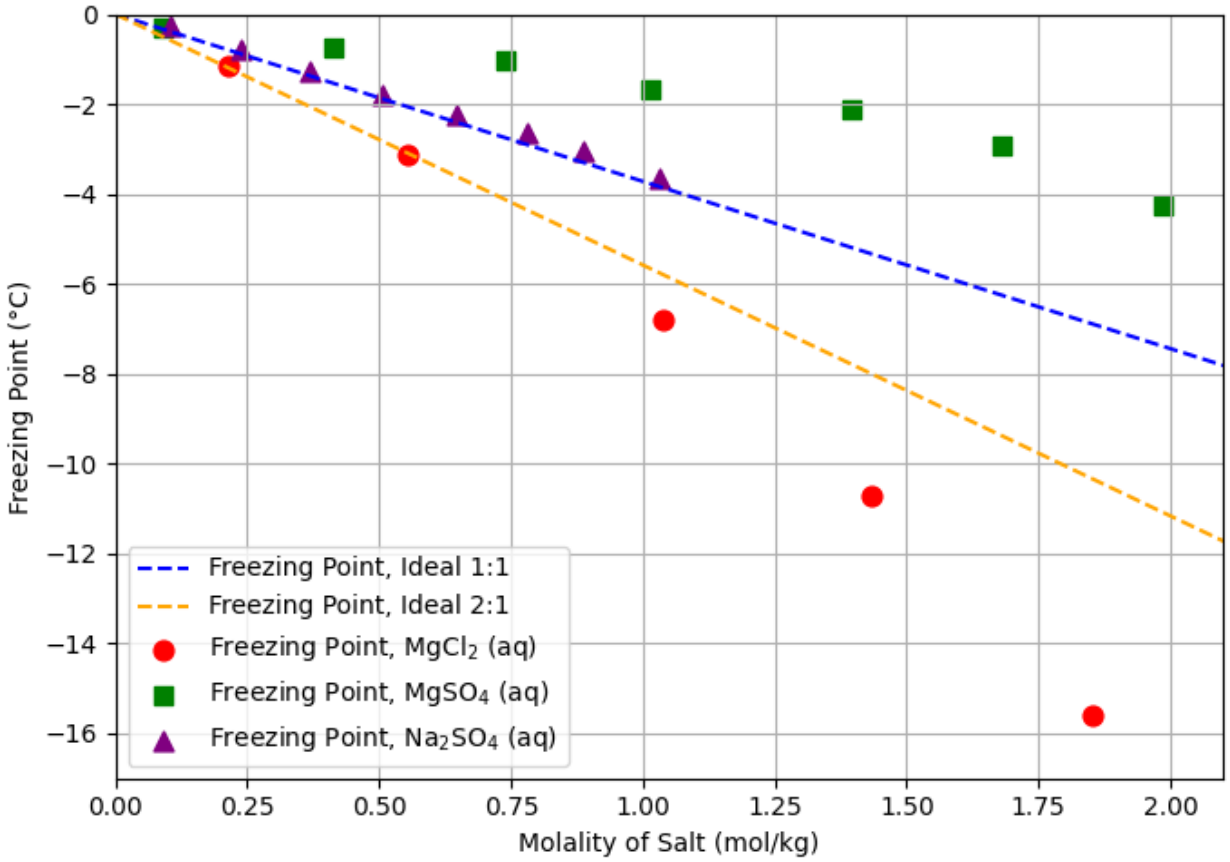

Figure 4.1: Freezing point depressions of aqueous salt solutions of interest and of ideal solutions at atmospheric pressure. The lines representing ideal behavior are controlled by the empirical freezing point depression constant for water, 1.86 K·kg/mol of ions, as per (4.1). $MgSO_4$ should be compared to the 1:1 line, whereas $MgCl_2$ and Na_2SO_4 should be compared to the 2:1 line. The data for $MgCl_2$ is reported in Haghighi et al. (2008) [6]. The data for $MgSO_4$ is reproduced from Pillay et al. (2005) and Denson et al. (2007) [7, 8]. The data for Na_2SO_4 is discussed in Brand et al. (2009) and Dougherty et al. (2013) [9, 10]. The y-axis, freezing point, can either be interpreted as the freezing temperature of the binary solution at the given concentration or the change in the freezing temperature relative to 273.15 K.

of free ions in solution [11]. The overall extent to which common salts effectively dissociate in water is captured by their activity coefficients (γ), which have been studied extensively at atmospheric pressure [6, 11–13].

There is considerably less data regarding the behavior of salt-water binary systems at high pressures. The high-pressure eutectics of common salts have been of interest to the scientific community and are characterized in the gigapascal regime at 25 °C for ices VI and VII with NaCl and ice VI with $MgSO_4$ [14–16]. The eutectics at elevated pressures and low temperatures for ice Ih have also been examined for NaCl, $MgSO_4$, and Na_2SO_4 [17–19]. Most recently, in 2024, a novel thermodynamic invariant point—the **cenotectic**, defined as "*the invariant point occurring at the lowest temperature at which the liquid phase, for any value of concentration, pressure, or other thermodynamic forces acting on the system, remains in stable equilibrium*"—was discovered and investigated for eight different binaries, including NaCl, $MgSO_4$, Na_2SO_4, and $MgCl_2$, at cold temperatures and pressures to 250 megapascals (MPa) [20]. The cenotectic data is in agreement with the previous studies referenced above, and has direct applications in planetary sciences concerning the geophysical structure evolution of icy worlds as well as their internal composition and surface features [10, 17, 18]. Figure 4.2 is a visual representation of the regions mapped within this work and their relation to the cenotectic κ.

To date, anticipated internal structures of the medium and large, ice-covered ocean worlds of the outer solar system (Figure 1.6) have been interpreted primarily through the phase diagram of pure water [21]. Regions of interest related to choice icy worlds are shown in Figure 4.3. Some studies have incorporated the sparse available thermodynamic data related to melting curves of common salts and their eutectics at pressure, but these are few and usually rely on extrapolated melting curves, rather than actual measurements [22]. Among the salts of interest to this work, $MgSO_4$ has been heavily scrutinized, estimated to comprise a large fraction of the solutes within Ganymede's hydrosphere and shown to exist on the surface of Europa [15, 23–26]. Other sulfur-bearing species including Na_2SO_4 are expected on the Galilean satellites and are either native or originate from volcanic activity on the neighboring

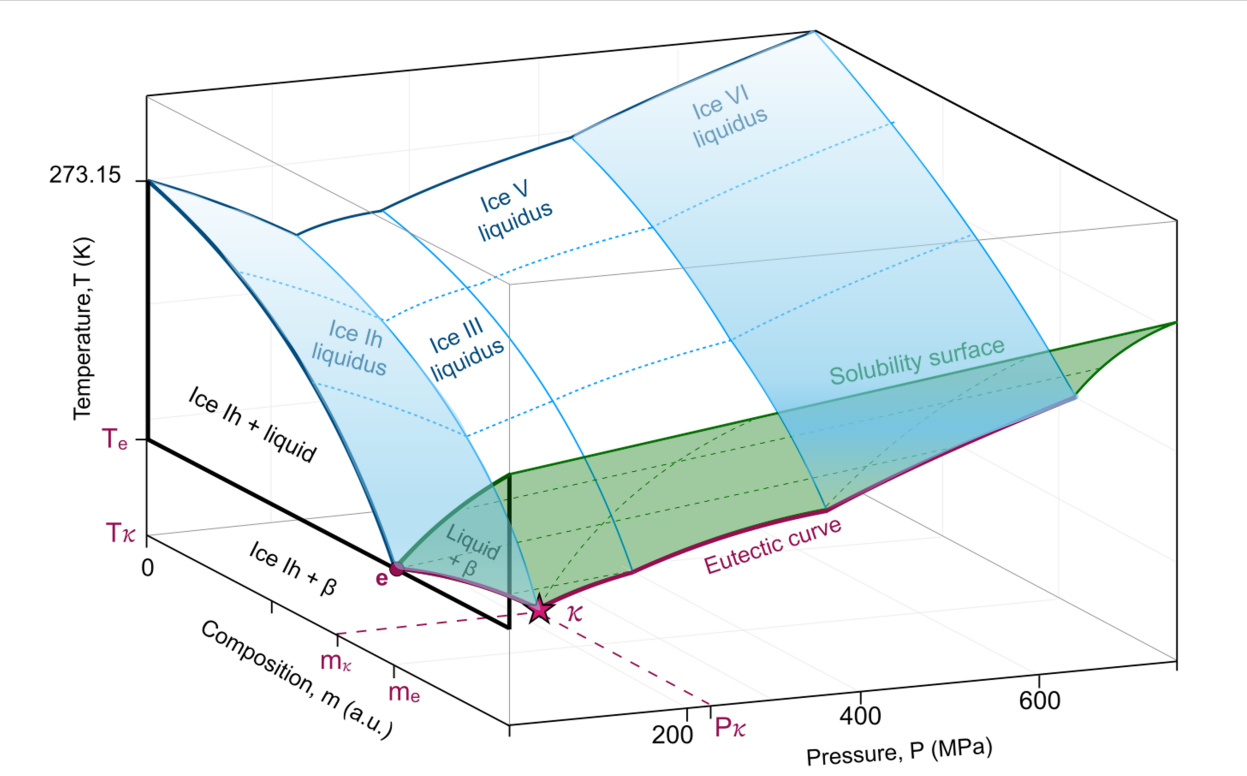

Figure 4.2: A phase diagram for a generalized salt-water binary in three dimensions, accounting for pressure, temperature and concentration of solute. The diagram assumes only one solute-bearing solid phase, e.g., a hydrate, for simplicity. The eutectic point at ambient pressure e is shifted to the cenotectic κ at higher pressure. The cenotectic is identified experimentally as the discontinuity of the slope of the melting curve at a eutectic concentration m_e. Blue, shaded regions are the melting surfaces of ice Ih and ice VI, evaluated in this work for simple binary systems of $MgSO_4$, Na_2SO_4, and $MgCl_2$. Adapted from Zarriz et al. (2024) [20].

moon Io—neutral, sulfur-containing compounds erupt from Io, are ionized and trapped in Jupiter's magnetosphere, and then are delivered to the other moons [27–29]. To a lesser extent, $MgCl_2$ should add to the composition of Ganymede [30]. Combinations of $MgSO_4$, Na_2SO_4, and $MgCl_2$, and certainly combinations of their respective cations and anions, can be accounted for via geochemical modeling based on expected pH, oxygen fugacity, relative solubilities, mineral leaching, radiogenic heating, and tidal energies, etc. [24, 31]. As is the case for all common, inorganic salts—regardless of their direct analytical detection—understanding their contributions to the geophysical processes and subsurface structure of large, icy worlds remains essential to the cutting edge of thermodynamic and space science research [32].

Experiments have previously used high-pressure sound speed measurements to look at the effects of common salts on the thermodynamics of aqueous solutions, but have fell short of measuring phase diagrams coordinates in those regimes, except for aqueous NaCl [16, 32, 38]. The salts NaCl, $MgSO_4$, Na_2SO_4, and $MgCl_2$ share cations and anions, and their relationship to one another can be visualized by a quaternary plot in three dimensions (Figure 4.4). This work (ongoing) attempts to quantify the melting curves for ice Ih and ice VI in the presence of $MgSO_4$, Na_2SO_4, and $MgCl_2$, with the intent of evaluating ternary and quaternary systems in the pressure, temperature, and concentration space. By choosing concentrations that are consistent between all three systems, their impact on the melting curves of water can further be investigated by linear sums of the end members and how much the predicted model may deviate from ideality. The NaCl-H_2O binary has already been accurately described for ice VI and ice VII from room temperature to nearly 600 K and one to six gigapascals [16].

Currently, no direct melting curve data exists for $MgSO_4$, Na_2SO_4, and $MgCl_2$ at low temperatures and within the range of pressures expected in icy worlds ($\leq$ 1.8 gigapascals, i.e., the upper limit of pressure estimated for the hydrosphere of Ganymede) [33, 39, 40]. Here, the melting curves of $MgCl_2$-H_2O from 230 K to room temperature and from 0.1 MPa (1 bar) to 250 MPa, and the melting curves of the $MgSO_4$, Na_2SO_4, and $MgCl_2$ binaries in water from 230 to 320 K and 400 to 1400 MPa, are presented up to concentrations of 3

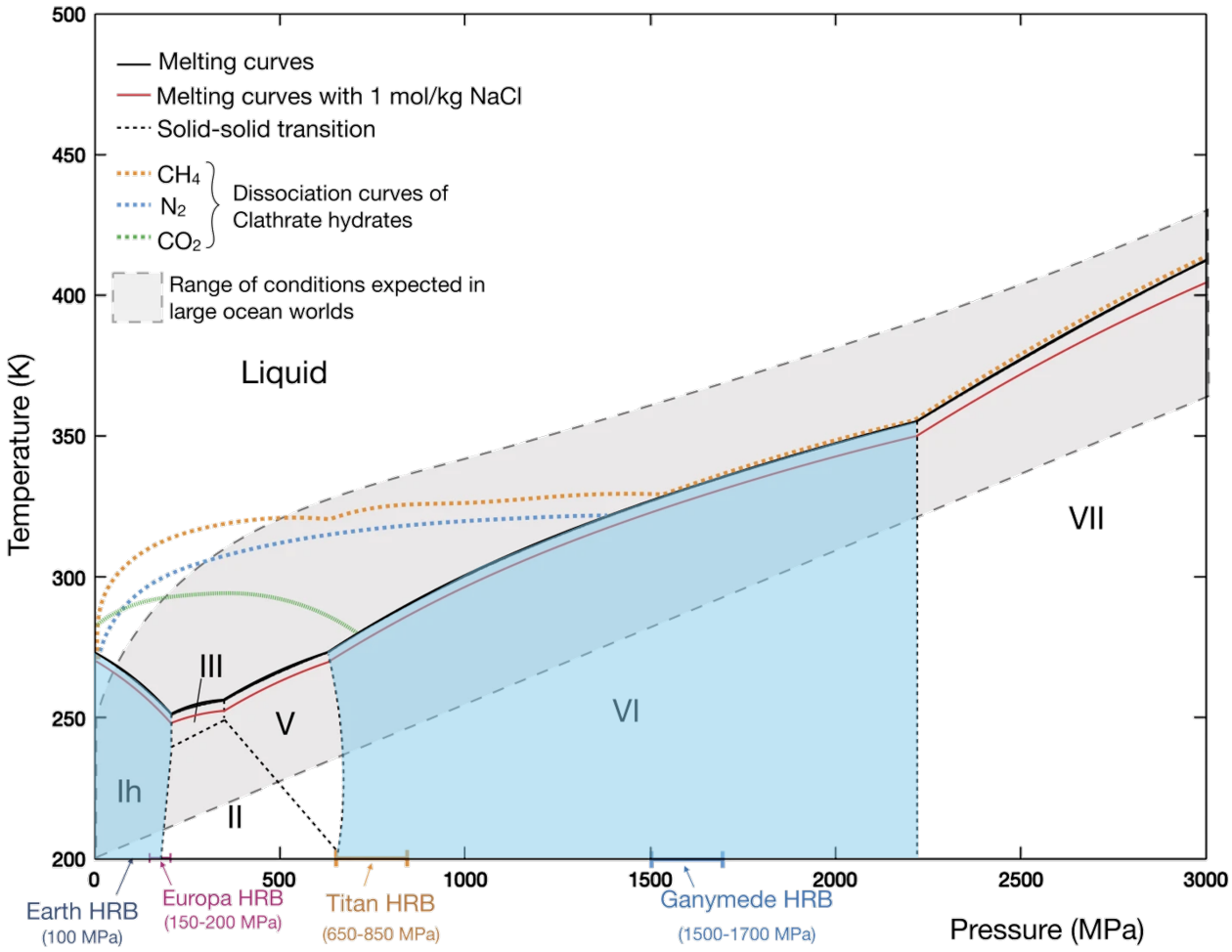

Figure 4.3: A phase diagram of pure water and previously investigated species, adapted from Journaux et al. (2020) [32]. Blue shaded areas represent regions of interest to this study. As noted in the source publication, melting curves and solid-solid phase transitions from ice Ih to ice VI are provided by SeaFreeze [33]. The melting curve of 1 m NaCl solution is incorporated in SeaFreeze and determined by Journaux et al. (2013) [16]. The ice VII liquidus is from Wagner et al. (2011) [34]. The solid-solid transition between ices VI and VII is from Bridgman (1937) [35]. The gray area is the range of conditions expected in icy worlds. Dissociation curves of clathrate hydrates are based on data from Sohl et al. (2010) [36] and Bollengier et al (2013) [37]. HRB stands for hydrosphere-rock boundary—the area of highest pressure at the bottom of the hydrosphere for the icy worlds provided. Callisto's hydrosphere is somewhat poorly constrained and not included in the original figure [32].

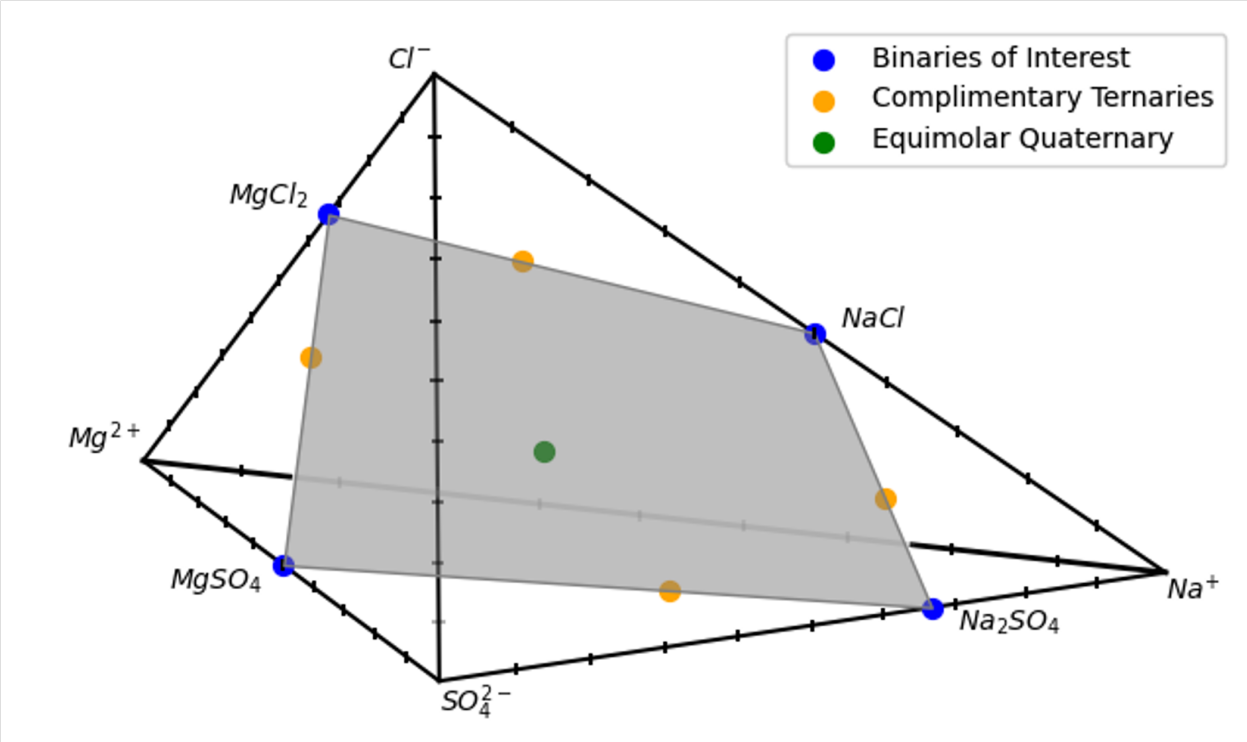

Figure 4.4: A quaternary plot visualizing the congruent combination of inorganic salts with common ions for binary systems (blue), ternary systems (yellow), and a mixture of all cations and anions (green). Ratios of ions for ternaries and the quaternary are 0.5 m with respect to ions. Along the axes, the ratio of cation and anions with respect to each salt is denoted.

molal (m). The individual pressure-temperature points comprising these curves are of an unprecedented precision, within ± 10 MPa and ± 0.6 K, based on calibration metrology developed in-house. The resulting melting curves are used to make surfaces quantifying the liquidus of applicable high-pressure ice polymorphs following the representation of local basis functions for thermodynamic data as per Brown (2018) [41]. The curves are matched to the surfaces to ensure proper representation. Importantly, they are also compared to a novel, pressure-dependent ideal mixing model—leveraging the capabilities of the SeaFreeze package (Journaux et al., 2020 [33])—to offer an upper-limit for the estimation of the generalized, aqueous melting curves of simple inorganic and organic solutes. This provides not only fundamental thermodynamic data on the behavior of binary salt-water systems of immediate relevance to the physical chemistry and Earth and space science communities, but also presents a model for predicting the impact of yet-to-be-investigated solutes on the melting curves of pure water.

4.2 Methods

The derivation of melting curves at high pressure presents a unique challenge from an experimental design standpoint. Uncertainty related to data collection has been an ongoing point of concern in the high-pressure community. Some studies do not even attempt to quantify the uncertainty of pressure and temperature measurements [42]. Others take a rigorous approach, with a high degree of precision approaching 30 MPa [16]. The methodologies of high-pressure liquidus determination are herein improved, as per the pressure calibration protocol described in Section 2.2.1, and are on-par with prior studies with respect to temperature [16].

Also, as a suite of thermodynamic information on pure water is readily available via the SeaFreeze package, there are a number of immediate applications for novel experimental data [33]. These include but are not limited to the exploration of the ideality of salt-water solutions at elevated pressures and in equilibrium with other polymorphs of water ice such as ice III, V and VI. The change in the melting temperature of aqueous solutions based on

pressure and the ideal mixing of simple salts in water is derived. This is used to approximate regions where data agree with an ideal model within the three-dimensional phase diagrams for salt-water binaries.

4.2.1 Experimental Methods

Experiments were performed using a BX90 diamond anvil cell (design optimized for Brillouin and scattering–x-ray diffraction with a 90° opening angle) equipped with ultra-low fluorescence diamond anvils (type IIas, Almax easyLab) of 700 µm culet diameter. Gaskets were made of Inconel® 718 (corrosion resistant nickel-chromium alloy). No reactions were observed between aqueous sample solutions and the gasket material during the experiments. Sample chambers were initially prepared to an average thickness of 150 µm and a diameter of 400 µm. The DAC was externally cooled by a Peltier module cooled cryostat presented in Section 2.1.4. Sample temperatures were monitored and recorded using a commercially calibrated K-type thermocouple in direct contact with the either the gasket or the diamond anvils. Temperature was calibrated using the melting and boiling point of pure water at 1 bar, and ice Ih and ice VI melting curve measurements in equilibrium with pure water, for which the coordinates are well known [33]. The pure water melting curves in the pressure and temperature range of interest were traced, and the response of the thermocouple and temperature reader system was documented. The uncertainty of the temperature calibration is ± 0.6 K as provided in Section 2.2.2.

Cr^{3+}-doped ruby spheres (Al_2O_3:Cr^{3+}) were included in the sample chamber and served as a pressure gauge based on the shift of the R1 line of the ruby fluorescence doublet circa 694 nm [43]. Spectra were produced using low laser powers (circa 100 µW to 2 mW) and from ruby spheres exclusively in the fluid fraction of the sample chamber to mitigate potential stresses and reduce error. At least one other ruby was placed on the backside of a diamond anvil to provide an *in situ* measurement of the ambient pressure R1 line at the same temperature of the sample chamber. Ambient and pressurized spectra were collected in triplicate for each data point and processed via the comprehensive ruby PL fitting package described

in detail in Section 2.2.1. The uncertainty of the pressure calibration never exceeds 10 total MPa around the median melting pressure.

Aqueous sample solutions were prepared by dissolving $MgSO_4 \cdot 7H_2O$, Na_2SO_4, and $MgCl_2$ salts ($\geq$ 99%, Sigma-Aldrich) in deionized water. Solutions were quickly loaded via syringe into the DAC sample chamber to minimize evaporation. The concentration of each sample solution was confirmed experimentally via observation of the melting temperature of either ice Ih or salt-specific hydrates at atmospheric pressure when a small air bubble was present in the sample chamber. The importance of an accurate concentration calibration is discussed in Section 2.2.4.

For each experiment mapping the ice VI melting curves of a unique salt-water binary, pressure was first increased at ambient temperature until the rapid onset of ice VI crystal growth. Upon a gentle reduction in pressure, the high-pressure phase was melted to select a single crystal. This crystal was kept in the sample chamber at all times during the experiment, and its size was minimized ($<$ 3% sample chamber volume) in equilibrium with the fluid before pressure and temperature data collection. The overall experimental pathway is visualized in Figure 4.5. Such small crystal sizes ensure that the concentration of the sample solution remains as close to its calibrated value as possible. For ice VI, upon cooling of the sample, the crystal first grows in size, and then pressure is manually lowered to shrink the crystal and return to an equilibrium characteristic of the liquidus—the last point of ice stability in equilibrium with the liquid. Density inversions were recorded when applicable (see Figure 1.7 for an example of the density inversion of ice VI in solutions of greater concentration). Ice VI tends to be metastable in the ice V regime due to a high degree of supercooling (15 to 35 K) based on DAC sample volumes. Thus the resulting curves extend below the pressures and temperatures associated with the solid-solid phase transition for pure water.

This process was repeated to determine the melting curves of ice Ih (Figure 4.5). Depending on the concentrations of sample solutions and their eutectic boundaries at low temperatures and pressures nearing one bar, ice Ih was at times unable to be isolated. Rather, hydrates formed preferentially, and their melting temperatures were used for concentration

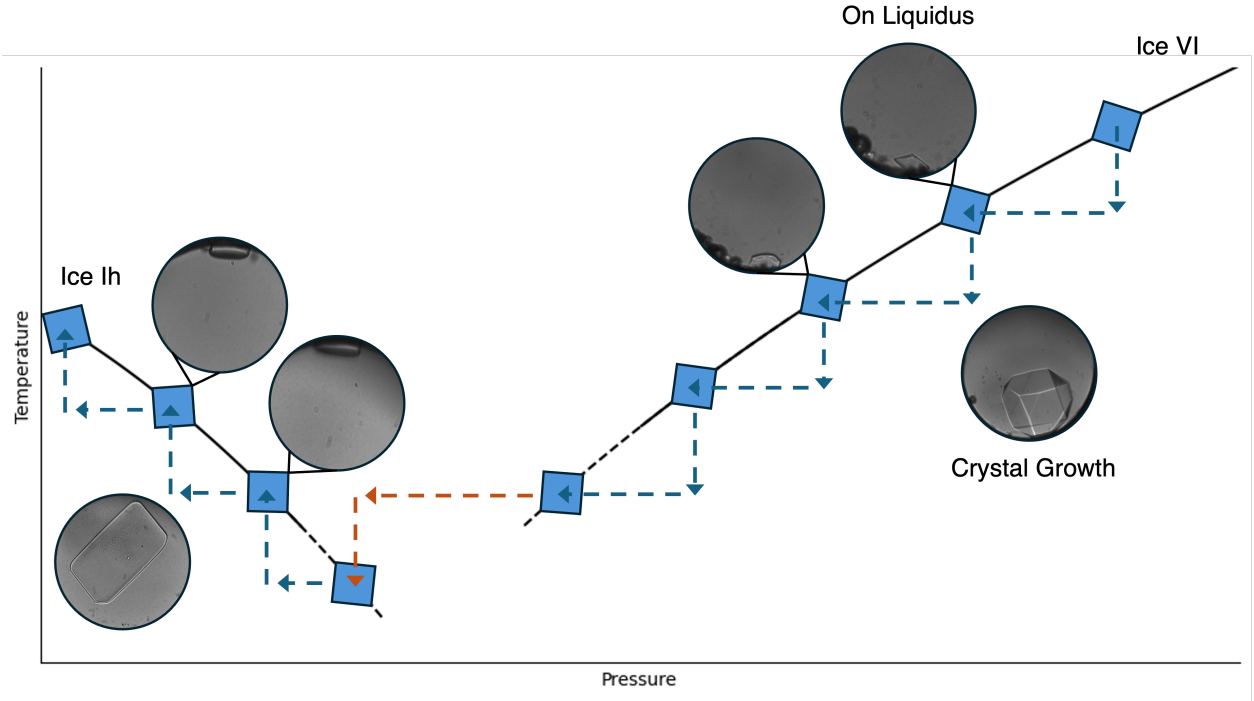

Figure 4.5: An example experimental pathway for the determination of ice VI and ice Ih melting curves at pressure. In general, ice VI is crystallized at or near room temperature and a single crystal is selected. Then, the cell is cooled and the crystal grows. Depressurization moves back to the ice VI liquidus, and another data point is collected. Once the ice VI curve has been mapped, the sample is further depressurized and cooled to isolate ice Ih. A single crystal is selected (again), and the process is repeated by cycles of depressurization and warming. Here, both ice VI and ice Ih curves are traced; however, if hydrates form upon movement into the ice Ih regime, the cell is warmed and the concentration is determined without stepwise movement along the ice Ih liquidus. Images on liquidus are of 1.5 m and 1 m $MgCl_2$ solution, from right to left, respectively. Crystal growth images are of ultra-pure and DI water.

calibrations only. For the salt-water binary in which ice Ih was observed at all sample concentrations ($MgCl_2$), the DAC was first cooled at or close to ambient pressure until the bulk crystallization of ice Ih. Pressure was then increased to melt the low density phase and yet again select a single crystal in equilibrium with the fluid. Pressure and temperature were decreased stepwise to remain along the melting curve.

Ice phases were confirmed via optical microscopy (for ice VI) and Raman spectroscopy (for ice VI and ice Ih). Selected Raman spectra for sample solutions are provided in Figure 4.6. All data was collected on the same optical set up as previously described in Section 3.5.3. In brief, all images and spectra were collected on a locally-built optical setup. Sample alignment and visualization was achieved using a 10X Mitutoyo Plan Apochromat long-working distance objective lens (0.28 NA), an integrated IDS Imaging Color CMOS camera, and a white fiber light source. Samples were excited using a 532 nm single-mode Coherent laser (Sapphire 532 SF NX). See Section A.1.1 for more details. Some example water Raman spectra produced here have already been presented in Figure 2.8 for the liquid, ice Ih and ice VI phases. Figure 4.7 (left) is a micrograph showcasing the classic structure of ice VI. This structure is typically observed during the fluctuation of the crystal with decreasing temperature and increasing pressure. When reducing the size of the crystal to return to the liquidus, the morphology changes and the ice loses these distinctive, visual qualities (Figure 4.7, right), being in a state of simultaneous growth and melt.

4.2.2 Ideal Model Methods

Consideration of colligative properties, e.g. freezing point depression, for a two-component (solvent A and solute B) system relies on a couple of assumptions: (i) the solute is not volatile and (ii) the solute does not dissolve in the solid phase of the solvent [4]. The first assumption ensures that vapor phase thermodynamic principles apply to the liquid, and is true particularly for high-pressure experiments in which the sample volume is sealed. The second assumption is well verified for ice Ih, but also realistic for ice polymorphs stable below 2.2 gigapascals (GPa). Indeed, inorganic salts have been shown to penetrate ice VII crystal

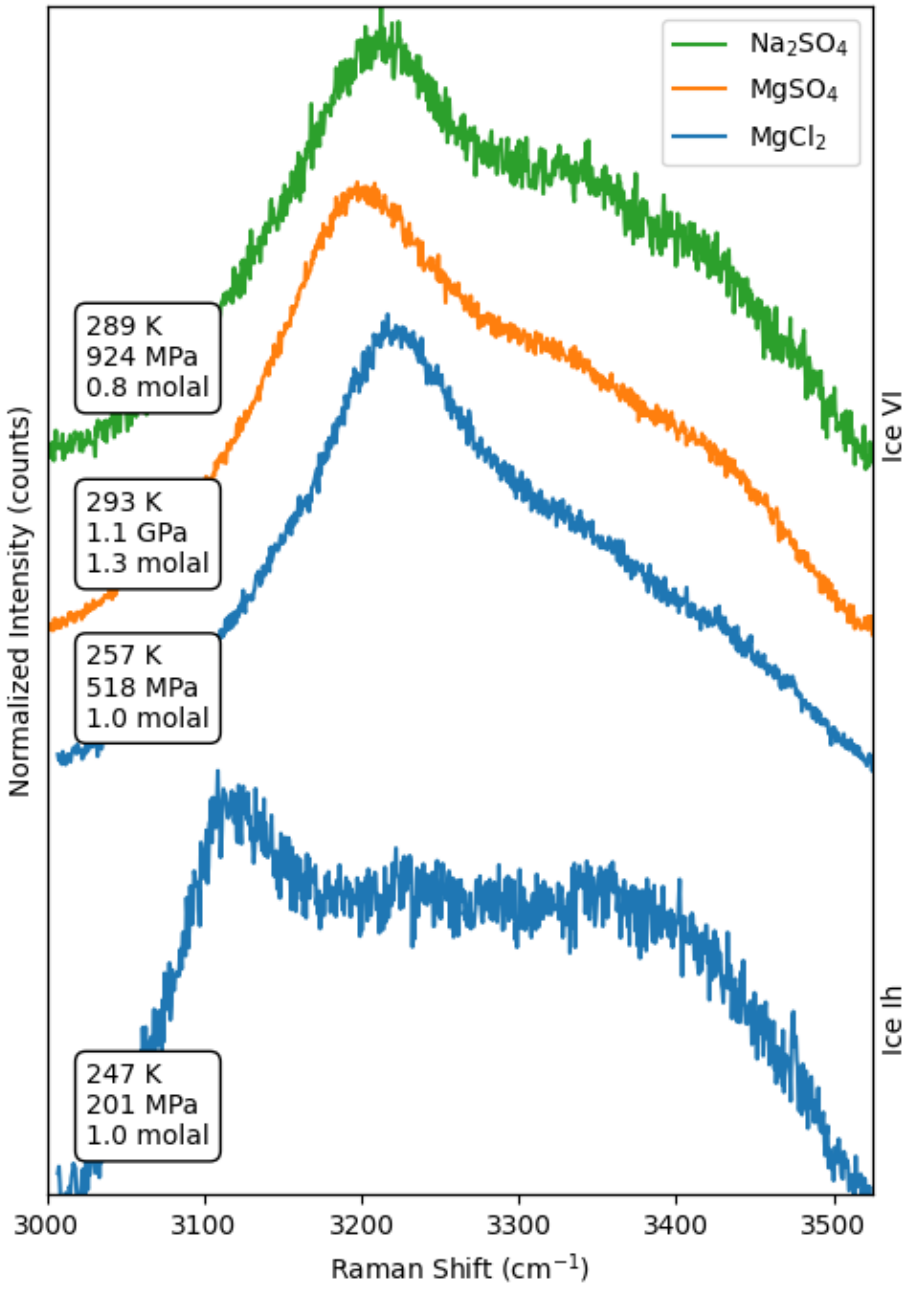

Figure 4.6: Example Raman spectra for ice Ih and ice VI with the applicable sample solutions. Sample temperature, pressure, and concentration are specified. Raman spectra are of the OH stretching region.

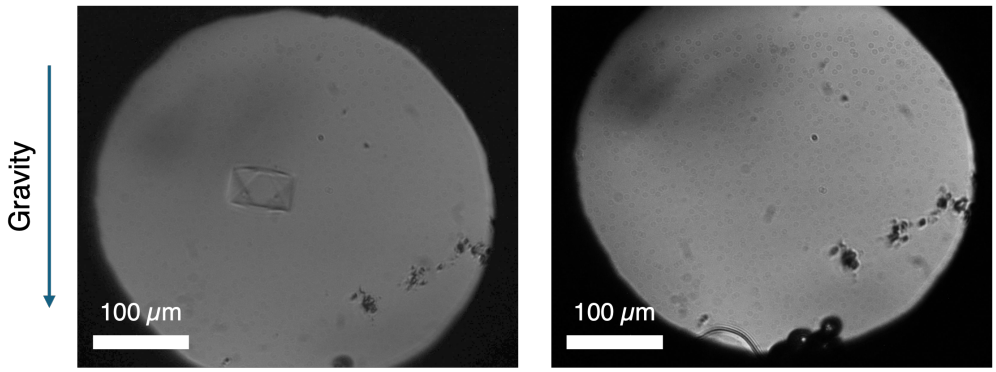

Figure 4.7: A micrograph of a single crystal of ice VI with classical morphology (left) and of the same crystal at a point along a melting curve (right), for reference. Scale bars are 100 µm.

lattices (the cubic phase of ice stable above 2.2 GPa), but remain quite incompatible with ice VI [44] and also likely with lower pressure polymorphs. As is the case for solutions at ambient pressures (Figure 4.1), deviations from ideality are expected to occur, particularly at higher solute concentrations.

Freezing point depressions are based on the reduction of the chemical potential of the solvent upon addition of solute. The equilibrium between solvent A and solute B at the freezing temperature T (K) of the solution is:

$$\mu_A{}^\star(s) = \mu_A{}^\star(l) + RT \ln x_A \tag{4.3}$$

where $\mu_A{}^\star(s)$ and $\mu_A{}^\star(l)$ are the chemical potentials (J/mol) of the pure solid and pure liquid phases of A, respectively, R is the ideal gas constant (8.314 J/mol·K), and x_A is the mole fraction of the solvent [4]. As the mole fraction of the solvent is always less than one in solution, the term $RT \ln x_A$ is negative. Rearranging (4.3) relates the change in chemical potential to Gibbs free energy:

$$\ln x_A = \frac{\mu_A{}^\star(s) - \mu_A{}^\star(l)}{RT} = \frac{-\Delta_{\text{fus}}G}{RT} \tag{4.4}$$

where $\Delta_{\text{fus}}G$ is the molar Gibbs energy (J/mol) of fusion. Because the the solid and liquid

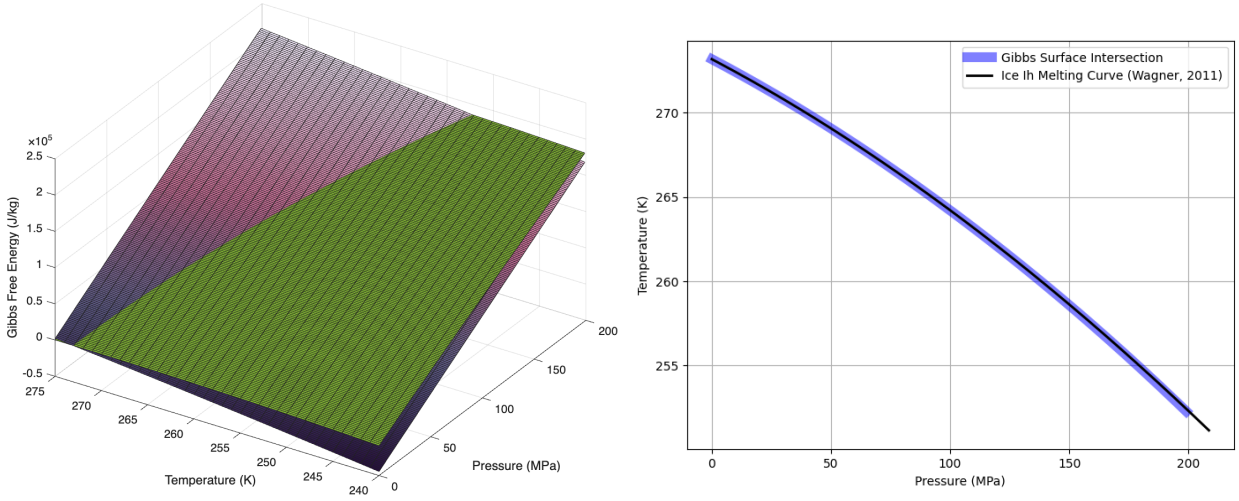

(a) (b)

Figure 4.8: Left: Gibbs energy surfaces for ice Ih (magenta color map) and liquid water (green) from SeaFreeze, plotted on the same axis. The intersection of the surfaces is visible, and defines the melting curve of ice Ih for pure water. Right: the output from the subtraction of the Gibbs energy surfaces at equivalence (blue bar), overlaid with the melting curve for ice Ih as per Wagner (2011) [34]. The curves are in agreement as a proof of the determination of melting curves via this method. Color map courtesy of Crameri et al. [45].

phases are at equilibrium at the freezing point, the change in Gibbs free energy is zero.

While (4.3) and (4.4) are fundamental, pressure is usually ignored as colligative properties are commonly reported only at 1 atmosphere. This can be circumvented. In the pressure-temperature space, the Gibbs free energy of pure water is modeled as a surface in three dimensions, represented for each phase using SeaFreeze [33]. The intersection of Gibbs energy surfaces for solid phases (ice Ih and ice VI) and the liquid derive the melting curve of water as a function of pressure and temperature. Figure 4.8 is a demonstration of this process using SeaFreeze for ice Ih. The output from the intersection of Gibbs energy surfaces—where the change in Gibbs energy between ice Ih and the liquid is zero—is in direct agreement with the melting curve for ice Ih based on equations of state.

The ideal freezing point depression (4.3) at any pressure and temperature is considered using Gibbs energy surfaces. Specifically, the chemical potential μ of a pure substance is

defined as the molar Gibbs free energy:

$$\mu \stackrel{\text{def}}{=} G_m = \frac{G}{n} \tag{4.5}$$

where n is moles. Given the differential of total Gibbs energy ∂G for a specific amount of pure substance in one phase, i.e. $\partial G = -S\partial T + V\partial p$, the differential of the chemical potential $\partial\mu$ is:

$$\partial\mu = -S_m\partial T + V_m\partial p \tag{4.6}$$

with temperature T and pressure p as independent variables [46]. The coefficients can be rewritten as:

$$(\frac{\partial\mu}{\partial T})_p = -S_m \quad \text{and} \quad (\frac{\partial\mu}{\partial p})_T = V_m \tag{4.7}$$

where S_m is the molar entropy and V_m is the molar volume [4]. Since the molar volume is positive, chemical potential increases with pressure along an isotherm, as demonstrated for the Gibbs free energy of water in Figure 4.8. In order to use (4.3), the chemical potential of water for each phase at variable pressures and temperatures is first computed using SeaFreeze [33, 47]. The change in entropy due to the reduction in mole fraction of solvent $R\ln x_A$ is then calculated for discrete temperatures over the entire surface for the pure liquid at their respective pressure coordinates. This modified surface is subtracted from that of the pure solid phase, and the new melting curve at the given concentration of solute ions is extracted.

4.3 Results

Here, the liquidus points for ice Ih and ice VI in the salt-water binary systems of $MgSO_4$, Na_2SO_4, and $MgCl_2$ are presented. A range of concentrations allows for the construction of surfaces representing the liquidus in three dimensions: pressure, temperature, and concentration. The median pressure (P_m), divergence of the lower (ΔP_{min}) and upper (ΔP_{max}) whiskers of the pressure calibration and temperature (T_m) for the melting points of each

phase are given. ΔP_{min} and ΔP_{max} are included to help interpret data dispersion in the absence of a uniform standard deviation of pressure around the median melting point.

4.3.1 Magnesium Chloride Results

The pressure and temperature coordinates for the liquidus of ice Ih and ice VI in the presence of $MgCl_2$ are reported in table 4.1 and table 4.2, respectively. The difference in minimum and maximum pressures (ΔP_{min} and ΔP_{max}) associated with the pressure calibration for each data point show a variance of less than 10 MPa in total around the median point assigned to the melting pressure (P_m).

The melting surfaces representing the liquidus of ice Ih and ice VI over the applicable pressure and temperature range are shown in Figure 4.9 and Figure 4.10, respectively. These surfaces are generated by the fitting of B-splines using the thermodynamic surface representation framework from Brown (2018) [41] to the pressure coordinates of the isomolal data, with temperature as the dependent variable. B-splines are local basis polynomials with matching derivatives at the boundaries of evenly spaced, arbitrary intervals. The parameters governing the fit, i.e., smoothing, spline order, and derivative minimization, are adjusted manually in order to produce a surface with minimal residual error while providing a reasonable behavior in extrapolated regions. For all surfaces, the second derivative of the fit with respect to pressure and the third derivative of the fit with respect to concentration are minimized.

The surfaces are anchored by a fourth data set—the melting curve of the corresponding ice phase for pure water—obtained from the SeaFreeze package [33]. The concentration of this curve with respect to the solute is assigned 0.01 m. This concentration is very dilute, and as such has a negligible effect on the liquidus, demonstrated for NaCl at high pressures and temperatures for ices VI and VII [16]. Including an anchor is another good way to evaluate the fit of the surface, as the residual temperatures with respect to the literature data should be zero.

The matching curves are plotted against the experimental data to ensure an appropriate fit (Figure 4.11). Provided that the output along isomolal curves from the surfaces is

Table 4.1: Experimental melting curve points of ice Ih for three different concentrations of $MgCl_2$

T_m (K)[1]	P_m (MPa)	ΔP_{min} (MPa)	ΔP_{max} (MPa)
1.0 mol/kg			
268.6	0.1		
266.5	17	-5	4
261.8	65	-1	2
256.1	129	-1	3
251.2	178	-3	1
247.4	201	-2	2
1.2 mol/kg			
266.5	0.1		
264.5	27	-2	1
259.6	69	-3	4
255.3	110	-2	1
252.7	129	-3	3
247.0	188	-2	4
245.0	206	-1	1
2.0 mol/kg			
257.2	0.1		
252.4	39	-2	3
246.5	101	-1	2
241.9	139	-2	4
237.4	183	-1	2

[1] Uncertainty related to temperature is ± 0.6 K for all measurements as given by the temperature calibration in Section 2.2.2.

Table 4.2: Experimental melting curve points of ice VI for three different concentrations of $MgCl_2$

T_m (K)[1]	P_m (MPa)	ΔP_{min} (MPa)	ΔP_{max} (MPa)
1.0 mol/kg			
286.2	894	-3	4
281.1	812	-2	3
277.1	764	-4	3
272.1	694	-4	3
267.3	640	-1	1
262.2	575	-4	5
257.2	518	-3	3
1.5 mol/kg			
296.1	1177	-3	5
290.9	1087	-2	2
285.5	1015	0	3
280.3	958	-4	2
275.7	863	-1	3
270.4	783	-2	1
2.0 mol/kg			
286.2	1195	-3	2
281.0	1095	-1	1
275.8	997	-5	2
270.6	922	-1	1
263.9	788	-3	3
258.0	712	0	3

[1] Uncertainty related to temperature is ± 0.6 K for all measurements as given by the temperature calibration in Section 2.2.2.

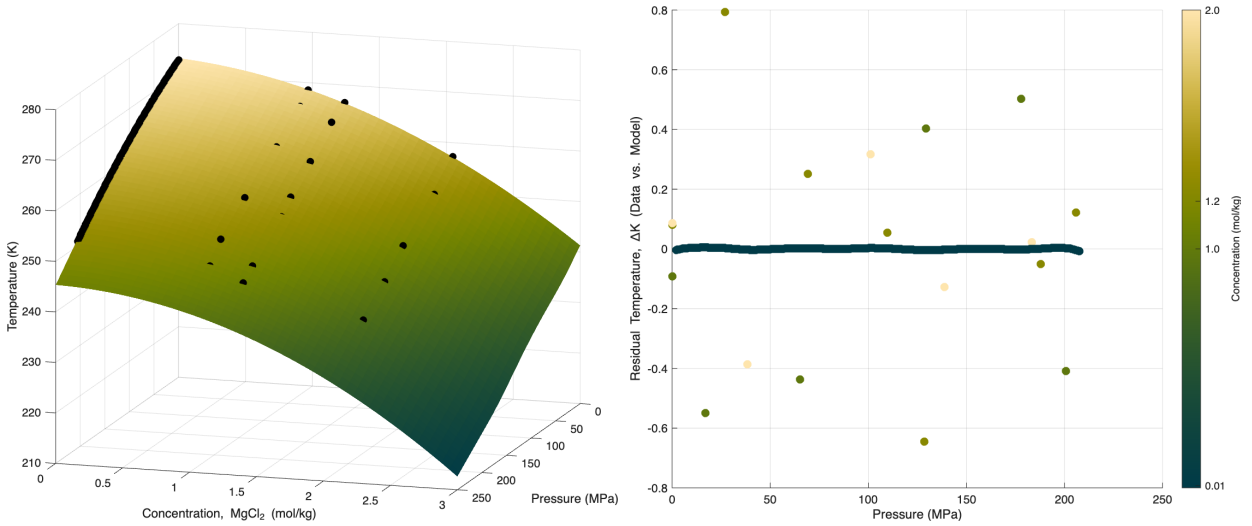

Figure 4.9: Left: the surface constructed from the isomolal melting curves of ice Ih in the $MgCl_2$-H_2O binary up to 3 m. Pressures and temperatures range from 0.1 to 250 MPa and 273.15 to 220 K, respectively. Data points (black) are listed in table 4.1. Right: residual plot of the fit of the data. Concentrations are color coded and specified. Color map courtesy of Crameri et al. [45].

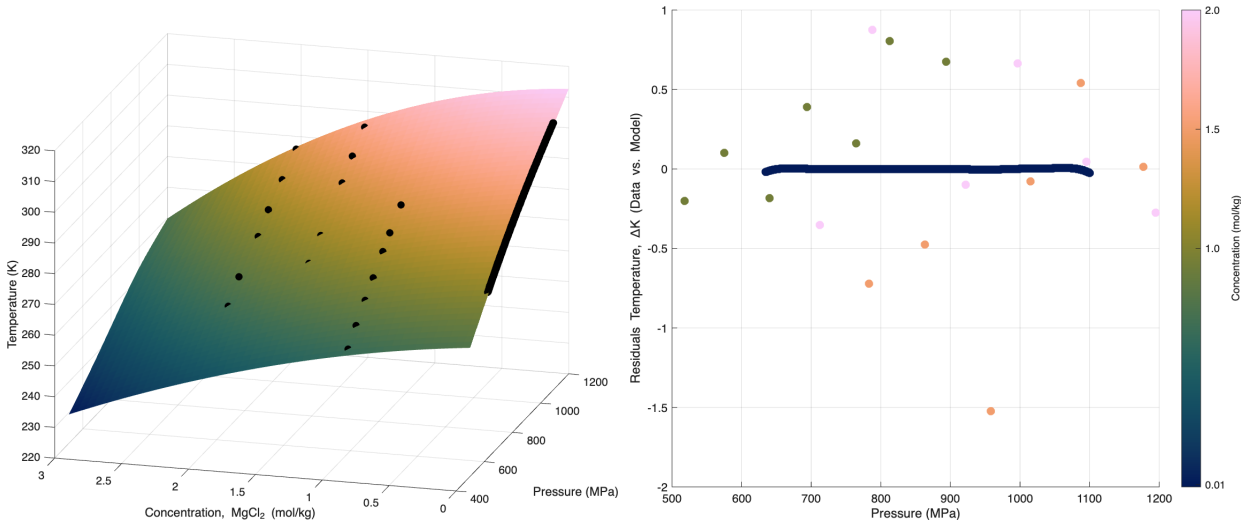

Figure 4.10: Left: the surface constructed from the isomolal melting curves of ice VI in the $MgCl_2$-H_2O binary up to 3 m. Pressures and temperatures range from 500 to 1200 MPa and 230 to 310 K, respectively. Data points (black) are listed in table 4.2. Right: residual plot of the fit of the data. Concentrations are color coded and specified. Color map courtesy of Crameri et al. [45].

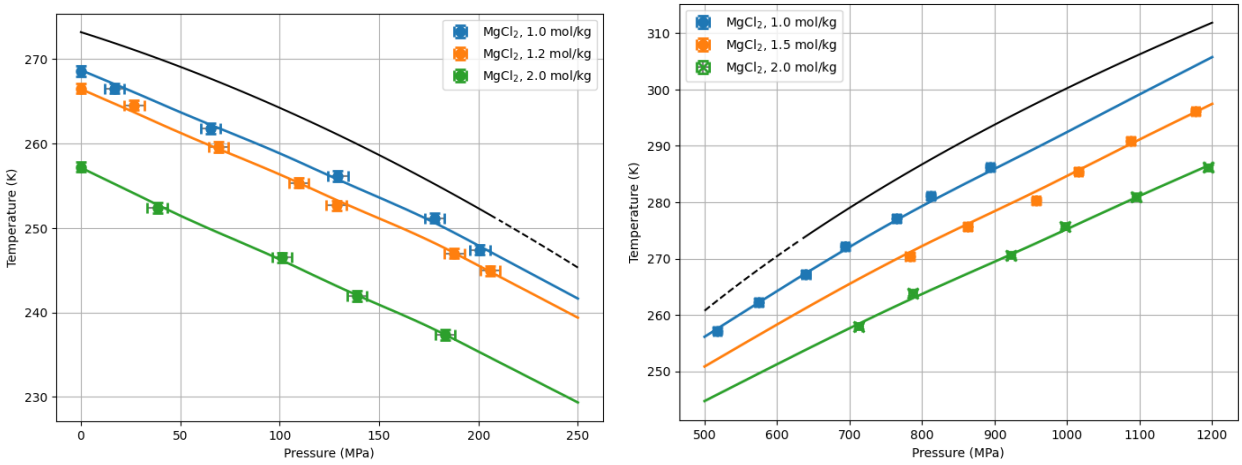

Figure 4.11: Isomolal melting curves of ice Ih (left) and ice VI (right) for the $MgCl_2$-H_2O binary system. Data points are listed in table 4.1 and table 4.2, respectively. Solid, colored curves are the output from the melting surfaces at each concentration (Figure 4.9 and Figure 4.10). The solid, black curve is the liquidus of pure water and is extended if needed to match the full range of pressure-temperature conditions [34]. Data points indicate either traditional density (circle) or density inversion (x) for the single crystal in the sample chamber. Error bars are generalized as ± 10 MPa and ± 0.6 K for all data points.

in agreement with the experimental data, the surface should be considered a satisfactory representation of the liquidus points for the entire pressure, temperature, and concentration space. In general, as the salinity of the sample solutions increases, the liquidus is shifted toward lower temperatures at equivalent pressures. The slope in pressure of the liquidus does not appear to change significantly from its depiction in the pure water system. At the highest, experimentally-tested concentration of $MgCl_2$, the depression on the ice Ih melting curve is roughly 15 K, and the depression on the ice VI melting curve is between about 15 to 25 K (300 to 400 MPa of additional pressure). As concentration increases, the depression on the melting curves of ice Ih and ice VI increases in a non-linear fashion, which is also expected based on the corresponding phase diagram at atmospheric pressure.

4.3.2 Sodium Sulfate Results

The pressure and temperature coordinates for the liquidus of ice VI in the presence of Na_2SO_4 are reported in table 4.3. Again, the minimum and maximum pressures (ΔP_{min} and ΔP_{max}) associated with the calibration for each data point have a variance of less than or equal to 10 MPa around the melting pressure (P_m). Absent here are data characterizing the melting curves of ice Ih at similar concentrations—upon cooling of the sample solutions at ambient pressures, hydrates form ($Na_2SO_4 \cdot 10H_2O$) which are stable at temperatures up to and above 295 K. The concentration of the samples was determined by observing the growth of these hydrates, depressurizing the sample chamber to one bar, and gentle heating of the DAC until all hydrates were observed to melt (outside of the cryostat apparatus).

The melting surface constructed from the data in table 4.3 is given in Figure 4.12. Residuals are included, and the variation around the very dilute curve (estimated 0.01 m Na_2SO_4) with respect to temperature is minimal. The shape of the surface can be attributed in part to the weaker effects of sulfate salts on the melting curve (known to be true at ambient pressures). Including more anchor points in the metastable region for ice VI may improve this representation. The high-pressure eutectic for the Na_2SO_4-H_2O binary likely exists somewhere below 3 m; however, it's exact composition at gigapascal-level pressures has yet to be determined.

4.3.3 Magnesium Sulfate Results

The pressure and temperature coordinates for the liquidus of ice VI in the presence of $MgSO_4$ are reported in table 4.4. As is the case for all of the data sets reported, the variance of pressures (ΔP_{min} and ΔP_{max}) for the calibration of each point is less than 10 MPa total. The melting curves of ice Ih at similar concentrations could not be determined for all samples. Hydrates ($MgSO_4 \cdot 7H_2O$) were observed to form at low temperatures and a concentration of 2.2 m. Unexpectedly, a mixture of hydrates and ice Ih formed at a lower concentration as well (0.7 m). Despite the stability of $MgSO_4$ over a wider range of concentrations in the

Table 4.3: Experimental melting curve points of ice VI for three different concentrations of Na_2SO_4

T_m (K)[1]	P_m (MPa)	ΔP_{min} (MPa)	ΔP_{max} (MPa)
0.8 mol/kg			
294.7	1040	-3	3
289.3	924	-3	3
284.4	854	-1	2
275.8	726	-2	3
272.3	692	-2	1
267.6	637	-3	1
261.6	545	-7	3
257.4	513	-1	4
1.2 mol/kg			
294.3	1062	-5	4
289.2	957	-4	4
287.0	932	-4	3
281.4	834	-3	3
273.0	724	-1	3
269.1	666	-2	4
259.5	556	-1	1
254.0	513	-3	5
249.4	456	-3	1
2.0 mol/kg			
296.1	1305	-3	3
290.4	1197	-4	2
283.1	1095	-4	3
279.2	1009	-5	4
266.3	850	-3	3

[1] Uncertainty related to temperature is ± 0.6 K for all measurements as given by the temperature calibration in Section 2.2.2.

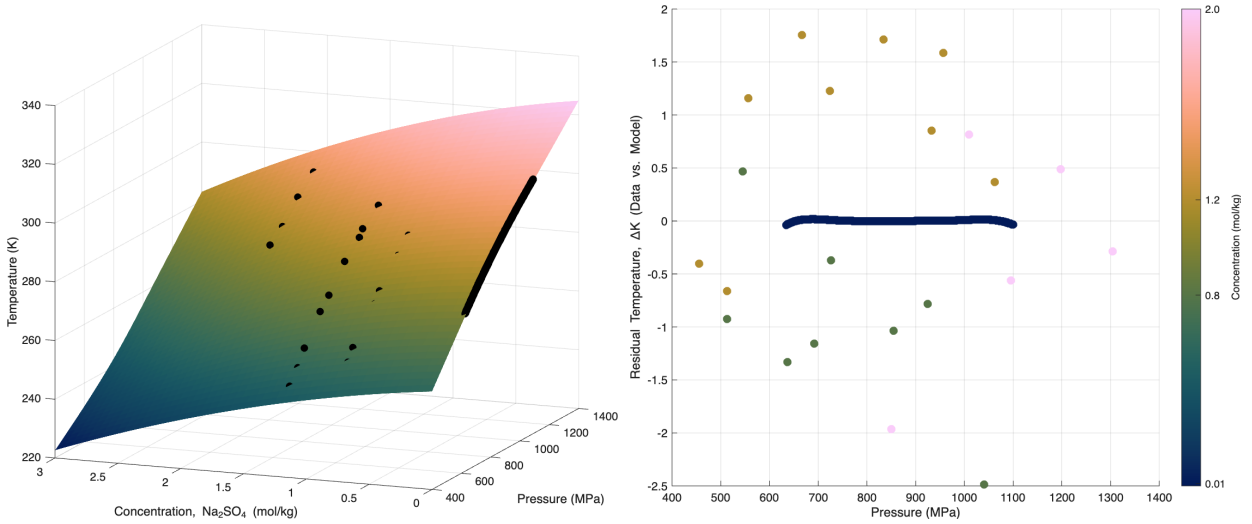

Figure 4.12: Left: the surface constructed from the isomolal melting curves of ice VI in the Na_2SO_4-H_2O binary up to 3 m. Pressures and temperatures range from 400 to 1400 MPa and 220 to 325 K, respectively. Data points (black) are listed in table 4.3. Right: residual plot of the fit of the data. Concentrations are color coded and specified.

liquid phase compared to Na_2SO_4, the overall depression in the ice Ih melting curve is similar at atmospheric pressure. The increased solubility of sulfate salts at high pressures allowed for the measurement of distinct curves.

The melting surface based on the data provided in table 4.4 is shown in Figure 4.14. The residuals of the fit with respect to the dependent variable, temperature, are also given. The very dilute melting curve (assigned 0.01 m with respect to $MgSO_4$) is properly incorporated. The temperatures associated with the surface here are better centered around the experimental data versus the surface for Na_2SO_4 solutions (Figure 4.12).

The extrapolation of isomolal curves from the $MgSO_4$ melting surface are plotted against the reported data (table 4.4) in Figure 4.15. These fit the data and do not deviate from the general shape of the ice VI liquidus for pure water at lower pressures and temperatures. At the highest concentration of $MgSO_4$ tested, the depression on the melting curve is roughly 15 K, or between 200 and 250 MPa of extra pressure. This is also the lowest relative impact on the ice VI liquidus at high concentrations of $MgCl_2$, Na_2SO_4, and $MgSO_4$. $MgSO_4$ has a

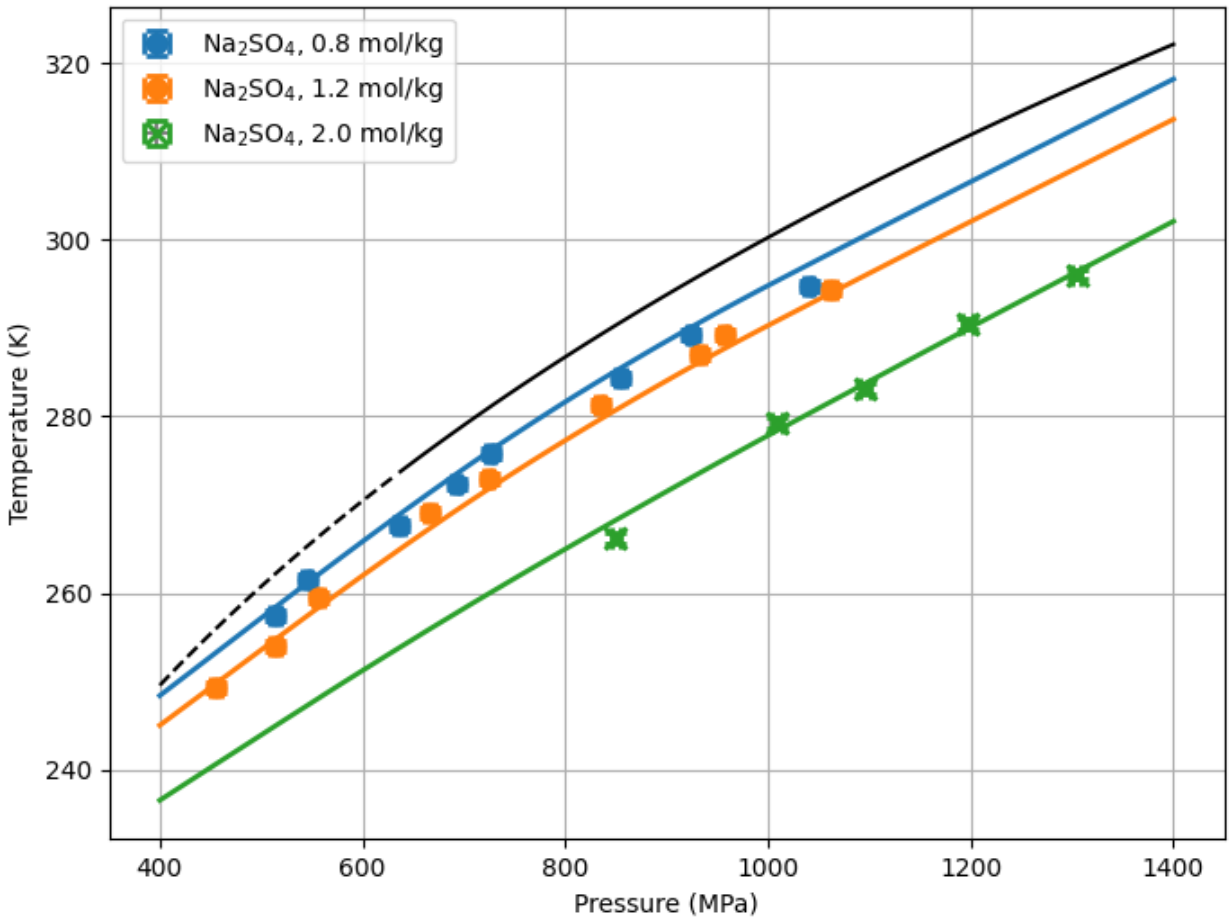

Figure 4.13: Isomolal melting curves of ice VI for the Na_2SO_4-H_2O binary system. Data points are listed in table 4.3. Solid, colored curves are the output from the melting surface at the specified concentration. The solid, black curve is the liquidus of pure water and is extended to match the full range of pressure-temperature conditions [34]. Data points indicate either traditional density (circle) or density inversion (x) for the single crystal in the sample chamber. Error bars are generalized as $\pm$ 10 MPa and $\pm$ 0.6 K for all data points.

Table 4.4: Experimental melting curve points of ice VI for three different concentrations of $MgSO_4$

T_m (K)[1]	P_m (MPa)	ΔP_{min} (MPa)	ΔP_{max} (MPa)
0.7 mol/kg			
295.0	970	-3	1
287.4	880	-3	2
283.3	805	-3	2
275.7	715	-1	2
271.2	661	-2	1
1.3 mol/kg			
293.1	1072	-2	3
286.5	953	-2	2
278.4	830	-2	2
271.0	718	-1	1
264.3	643	-3	2
258.8	586	-3	2
254.8	550	0	2
2.2 mol/kg			
296.3	1220	-2	2
288.2	1096	-3	1
281.0	981	-2	3
271.6	850	-2	1
265.3	767	-3	4
258.5	684	-2	1
254.6	631	-1	0

[1] Uncertainty related to temperature is ± 0.6 K for all measurements as given by the temperature calibration in Section 2.2.2.

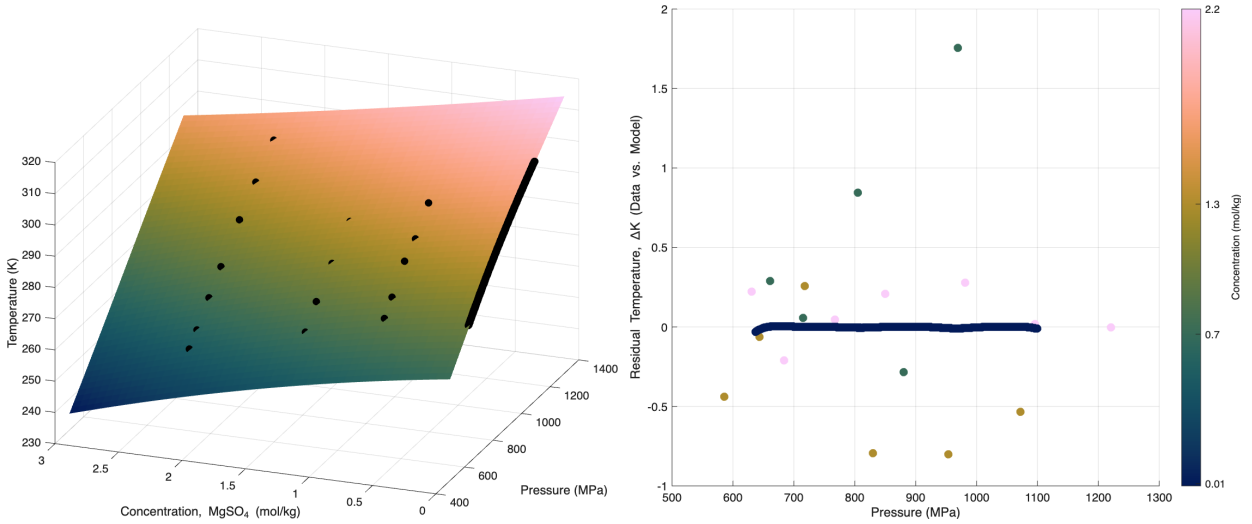

Figure 4.14: Left: the surface constructed from the isomolal melting curves of ice VI in the $MgSO_4$-H_2O binary up to 3 m. Pressures and temperatures range from 500 to 1300 MPa and 235 to 320 K, respectively. Data points (black) are listed in table 4.3. Right: residual plot of the fit of the data. Concentrations are color coded and specified.

lower effective concentration with respect to ions, and so a weaker general effect on the ice VI melting curve is anticipated.

4.4 Discussion

The presence of common salts in solution has a significant impact on the liquidus of ice VI at ambient to low temperatures and on the liquidus of ice Ih at elevated pressures. The determination of the melting curves at high pressure for these salts—aside from being the greatest mass provision of fundamental data on the behavior of these systems, to date—opens avenues for data analysis not previously explored in detail. These include the investigation of ideal behavior for simple salt binaries beyond one bar, the quantification of density inversion conditions for ice VI, and the evaluation of past work for which this data was not available.

Using the ideal modeling framework introduced in Methods section 4.2.2, predicted melting curves based on colligative properties are compared to the data (tables 4.1, 4.2, 4.3, and 4.4) for $MgSO_4$, Na_2SO_4, and $MgCl_2$. As a reminder, the deviation from the ideal line for

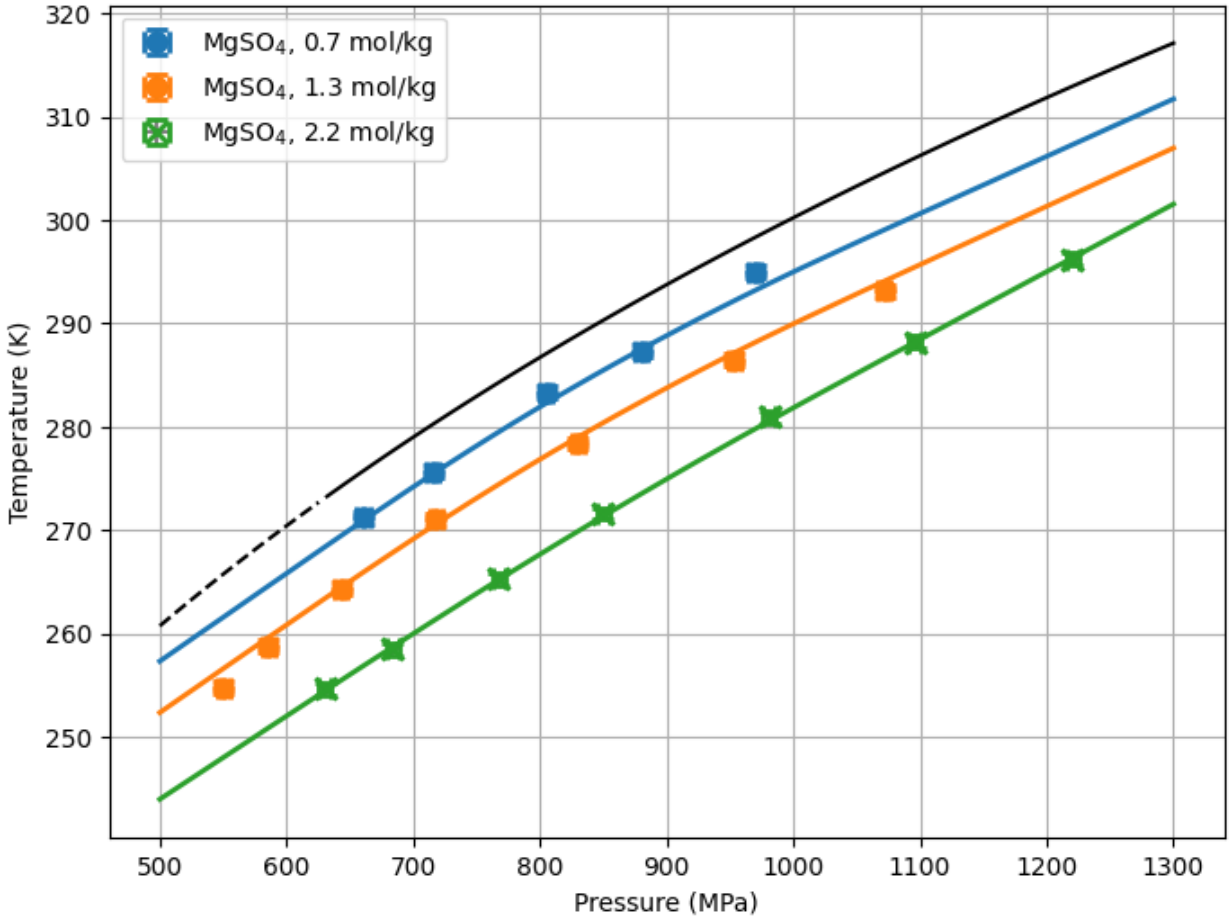

Figure 4.15: Isomolal melting curves of ice VI for the $MgSO_4$-H_2O binary system. Data points are listed in table 4.4. Solid, colored curves are the output from the melting surface at the given concentration. The solid, black curve is the liquidus of pure water and is extended to match the full range of pressure-temperature conditions [34]. Data points indicate either traditional density (circle) or density inversion (x) for the single crystal in the sample chamber. Error bars are generalized as $\pm$ 10 MPa and $\pm$ 0.6 K for all data points.

freezing point depressions of ice Ih at ambient pressure is shown in Figure 4.1. At one bar, sulfates are rarely ideal unless concentrations are below 0.25 to 0.5 m with respect to the salt. $MgCl_2$ tracks with ideality until about 1.0 m. At pressure, findings are presented in Figure 4.16 with the same format as the fits of melting surfaces. Visually, the ideal melting curve for all salt-water binaries seems to match at least the lowest concentration solution tested, in order (a) through (d). For $MgCl_2$ with ice Ih, both 1.0 and 1.2 m experimental data track with their ideal representations. At higher pressures with ice VI, $MgCl_2$ still matches the ideal line at 1.0 m, but sharply departs from the model at greater concentrations. Solutions of Na_2SO_4 also have lower concentration values of 0.8 and 1.2 m scattered around ideal curves. $MgSO_4$ only aligns with the ideal prediction at 0.7 m. These findings suggest that pressure, as an additional parameter, promotes the ideality of binary solutions of simple salts up to much greater concentrations than is observed at one atmosphere. The cutoff would seem to be at around 1 m with respect to the solute for ice VI, and slightly higher molalities for ice Ih with $MgCl_2$. Activity coefficients at high pressures have not been determined, but ideal behavior in this case can somewhat indicate effective activities close to 1, as the model assumes complete dissociation of ions in solution.

The local structure of liquid water has been observed to change to a dense, close-packed state at pressures nearing 4 GPa [48]. Between 500 MPa and 1.9 GPa—more relevant to both the conditions of salt solutions presented here and the predicted interiors of icy worlds—there is still a departure from the purely tetrahedral coordination of liquid water; however, the exact location of the transition is unclear [48]. Additionally, the solvation shell of chloride ions is known to drastically increase at pressure, from 6 water molecules at 0.1 MPa to about 16 water molecules at 1.7 GPa [49]. Together, these factors could contribute to a presumed increase in ideal behavior for aqueous salt binaries, especially if the coordination number of sulfate ions trends with pressure in a similar manner. The extended solvation of anions may disrupt the ability of contact ion-pairs to form in solution, at least at low temperatures. It is also entirely possible that ion-pairing interactions persist in these systems, and that due to a combination of different processes, the net energetic interactions at pressures approaching

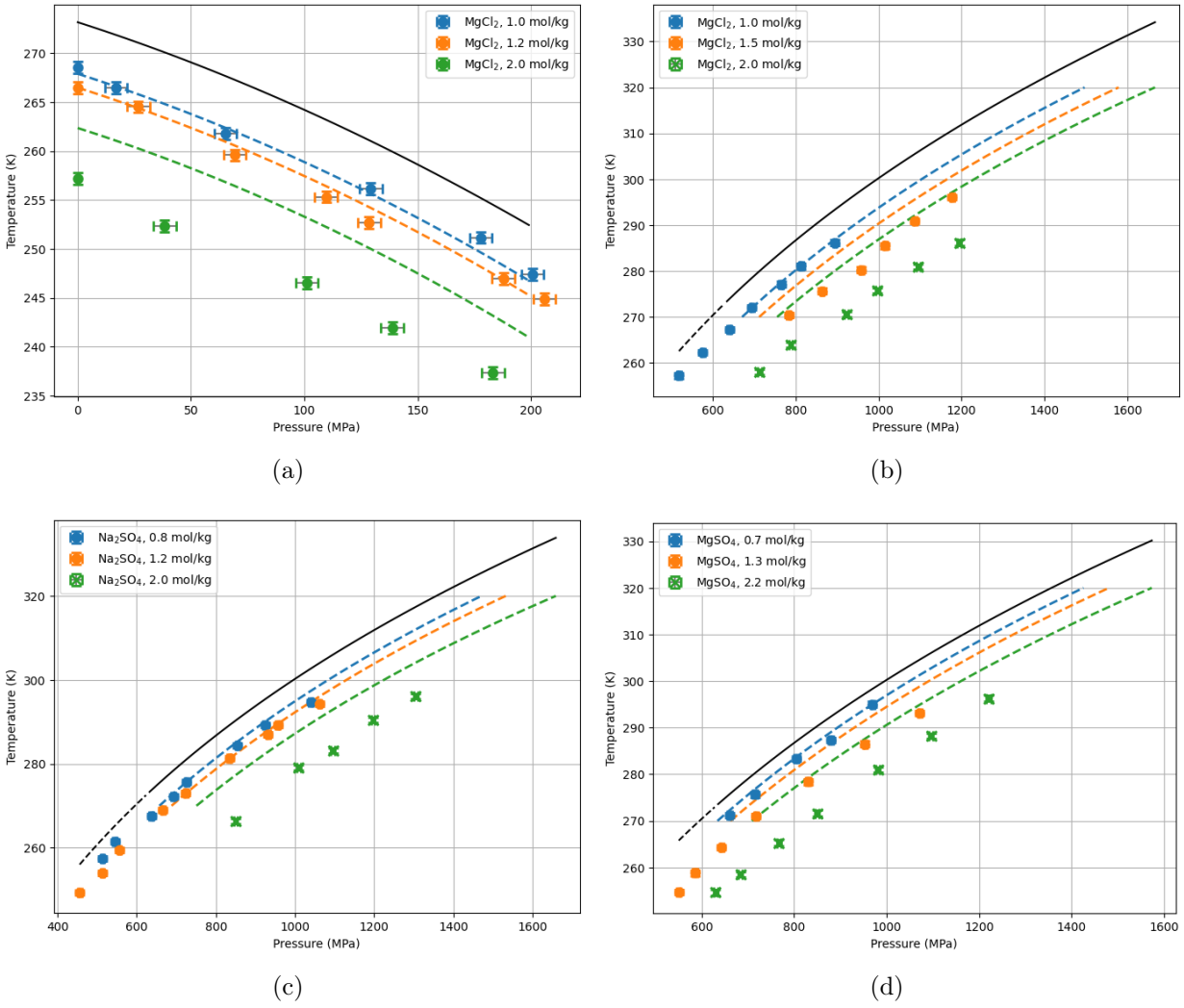

Figure 4.16: Ideal model predictions for the melting curves of (a) ice Ih with $MgCl_2$, (b) ice VI with $MgCl_2$, (c) ice VI with Na_2SO_4, and (d) ice VI with $MgSO_4$. Colored, dashed lines are the ideal curve at the same concentration given for the data points. Density inverted data (x) is denoted. The ideal curves can only be estimated from SeaFreeze up to either the temperature or pressure of the known triple point for their systems (ice Ih-ice III-liquid, or ice VI-ice V-liquid). Error bars are generalized as $\pm$ 10 MPa and $\pm$ 0.6 K for all data points.

a gigapascal sum to zero. Extensive molecular dynamics simulations characterizing the behavior of chloride and sulfate-bearing salts in water within the suggested ideal range (up to a concentration of 1 molal and a gigapascal of pressure) are likely required to underpin the forces responsible for this behavior.

Potential trends related to pressure effects for presumed ideality are explored by comparison of residual temperatures—the temperature difference between the experimental data and the model prediction at equivalent temperatures. Residual plots are given in Figure 4.17. The ideal curve was extended to match the pressure-temperature range of the data for ice VI systems. Data that are randomly scattered around the dashed line at zero indicate a good fit of the ideal model (Figure 4.17, a). Data that trend either towards or away from zero may demonstrate adverse pressure effects on ideality, as is the case for 0.8 and 1.2 m solutions of Na_2SO_4, and to a lesser extent 1.0 m solutions of $MgCl_2$ (Figure 4.17, c and b, respectively). As a more targeted indicator of the regions of ideal behavior, the residuals show that for aqueous solutions of common salts—for both chloride- and sulfur-bearing species—ideal behavior is observed at concentrations up to about 1 m on average and pressures up to one gigapascal. Then, the reverse is also true: given a concentration of salt up to 1 m and at high pressure ($\leq$ 1 GPa), an ideal solution model based on freezing point depression provides a reasonable estimate for the melting curves of ice Ih and ice VI. The major implication here is that the melting curve or surface of the salt-water binary of interest does not have to be mapped in order to approximate the impact of the solute on the liquidus. So long as the conditions are within the given range, the melting curves of high-pressure ices can be approximated with better accuracy versus the phase diagram of pure water alone.

The results of the high-pressure ideal model are within the scope of expected interiors and hydrosphere compositions of icy worlds. Standard ocean salinity on Earth is about 0.55 m with respect to salt compounds, comprised predominantly of the monovalent species NaCl [50]. Other salts are present, though in significantly lower concentrations, with $MgSO_4$ being the next common component. These data are included for equation of state measurements used in the recent modeling of the interior structures of ocean worlds [40, 51];

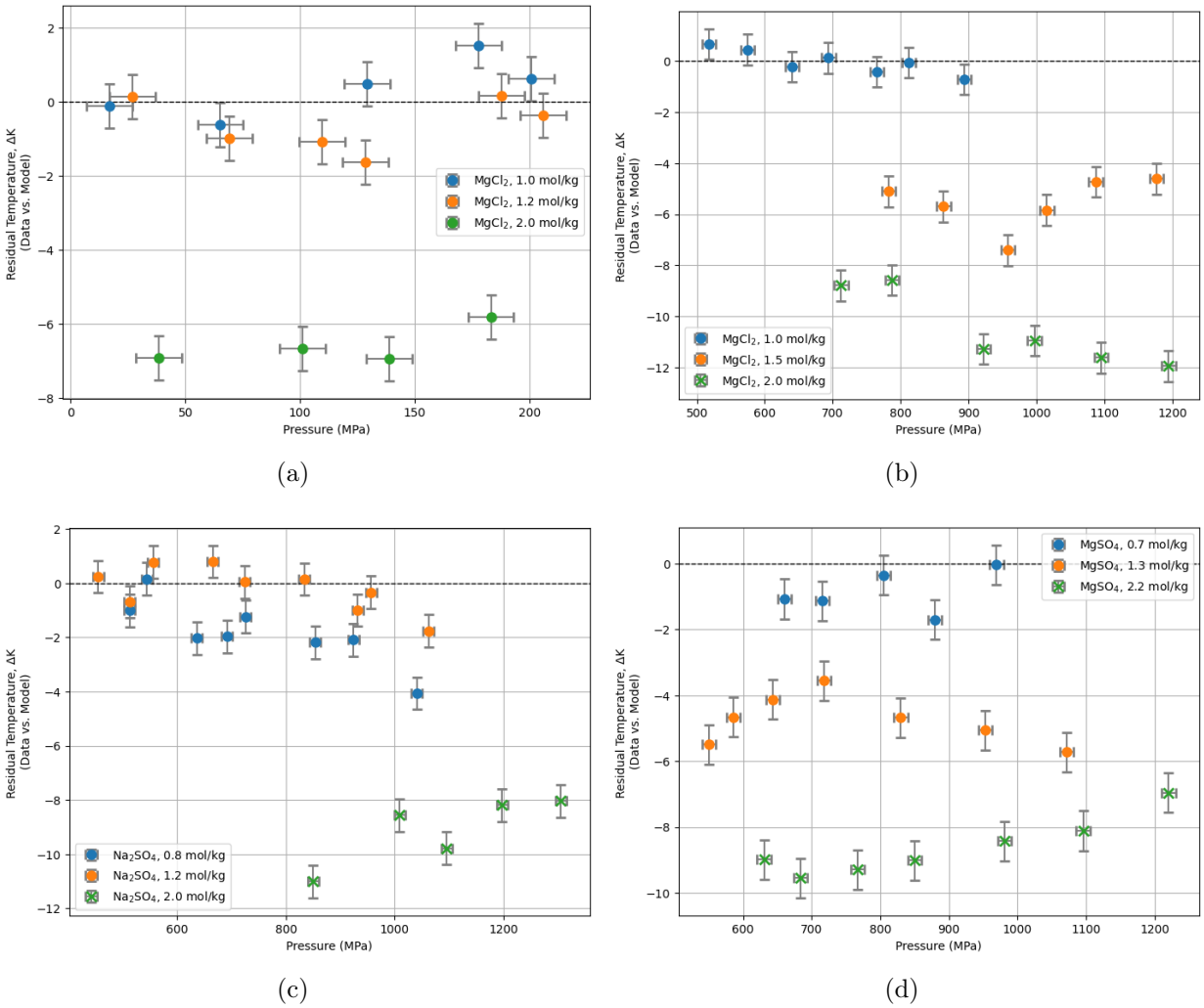

Figure 4.17: Residual temperature differences between experimental data and ideal model predictions for the melting curves of (a) ice Ih with $MgCl_2$, (b) ice VI with $MgCl_2$, (c) ice VI with Na_2SO_4, and (d) ice VI with $MgSO_4$. The dashed line at zero represents the ideal curve, and the data points are color coded to denote their concentrations. Centering at around or close to zero ΔT indicates a good fit of data with the ideal model. Density inversions are also visually separated. Error bars are generalized as $\pm$ 10 MPa and $\pm$ 0.6 K for all data points.

however, their validity is only up to 100 MPa. The ideal model derived here can greatly improve the reliability of these estimates, reducing their uncertainty to that of the measurements themselves. The standard ocean salinity is within the bounds of the ideal model, and it extends the applicable range of pressures by an order of magnitude. For reference, a one degree kelvin depression on the melting curve is equivalent to a change in ocean thickness of tens of kilometers, assuming all other factors remain constant [40]. Changing parameters on a global scale demands re-analysis of geophysical and meteorological data that could significantly impact the current predicted structures of icy, ocean worlds. These findings should be considered and incorporated in the analysis of future data from exploratory space missions.

All of the salts of interest also induce density inversions at high concentrations. These could seem dependent on the identity of the salt, as no density inversion was observed for an effective ionic concentration of 4.5 m with $MgCl_2$, despite one present in solutions of $MgSO_4$ at lower concentrations. However, since each salt has a different molar mass, evaluation of density inversion trends is better suited through weight percentages (%w/w, or wt%) of salts in solution. This metric is normalized with respect to molar mass and does not need to account for differences in total solute ions. Of the data collected here, density inversions were observed exclusively for the highest concentration samples in each set (Figure 4.18). A region of density inversion for ice VI is approximated. This is the range of pressures between the first experimental concentration at which density inversion occurs and the next lowest concentration. The density inversion is reported around the mean concentration: 14.25 $\pm$ 1.75 wt% ($MgCl_2$), 18.35 $\pm$ 3.75 wt% (Na_2SO_4), and 17.25 $\pm$ 3.75 wt% ($MgSO_4$). The documented concentration of density inversion in aqueous NaCl solutions is about 9.1 $\pm$ 3.6 wt% [16]. These are assessed to determine a regime for ice VI density inversion in a brine of simple salts (Figure 4.19). There is no observed concentration common among $MgCl_2$, $MgSO_4$, Na_2SO_4, and NaCl. Though, there is a band from 14.6 and 16 wt% between the salts presented in this work. Interestingly, the density inversion regions for sulfate-bearing salts are almost identical. It is also important to note that concentration calibrations (as described in Sections 2.2.4 and 4.2.1) were not performed for the NaCl solutions used in

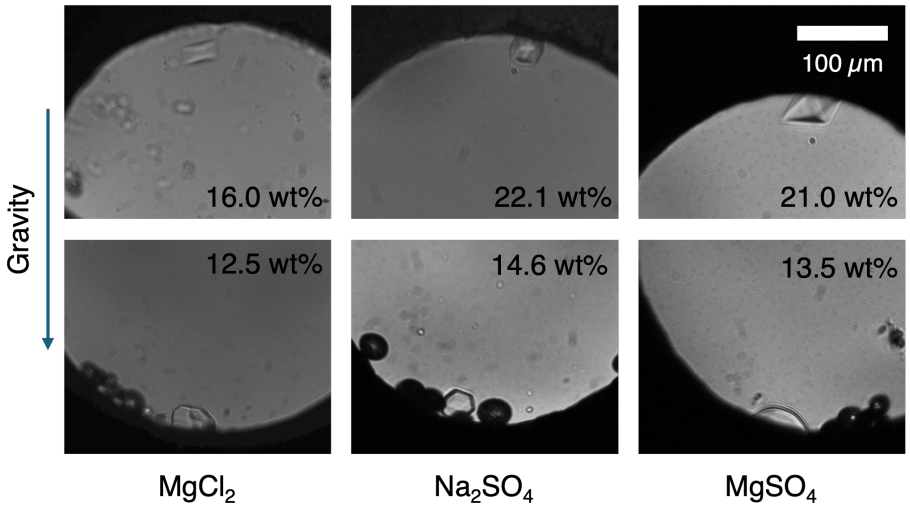

Figure 4.18: Density inversions for ice VI of salts observed at the listed concentrations (top half) and the next lowest concentration samples for which no density inversion was observed. Scale bar is 100 µm for all micrographs. Density inversions persisted over the entire range of pressure and temperature conditions evaluated for applicable samples.

Journaux et al. (2013) [16]. Inhomogeneity of solutions at low concentrations introduces variations in concentration upon loading. Failed experiments (not presented) with $MgSO_4$ include one originally prepared at 5.6 wt%—the same concentration of the lower bound NaCl solution—that exhibited no quantifiable effects on the melting curve of ice Ih or ice VI. On the other end, and especially at higher weight percentages, rapid evaporation during DAC loading almost always results in an increased concentration for sample solutions. The NaCl data may need to be revisited, as no other measurements currently exist.

Additionally, the now-known melting surfaces of ice Ih and ice VI can be leveraged to better characterize data from prior studies of salt-water binaries at high pressure. For example, the novel cenotectic point (κ) was recently found using eight aqueous binary systems [20]. The cenotectic occurs at the discontinuity in slope of the pressure-temperature curves for eutectic solutions. While those conditions are given, the actual concentration of solutions at the cenotectic are unknown. For $MgCl_2$, the cenotectic concentration can be estimated by interpolation of the available data onto its melting surface for ice Ih (Figure 4.20). The

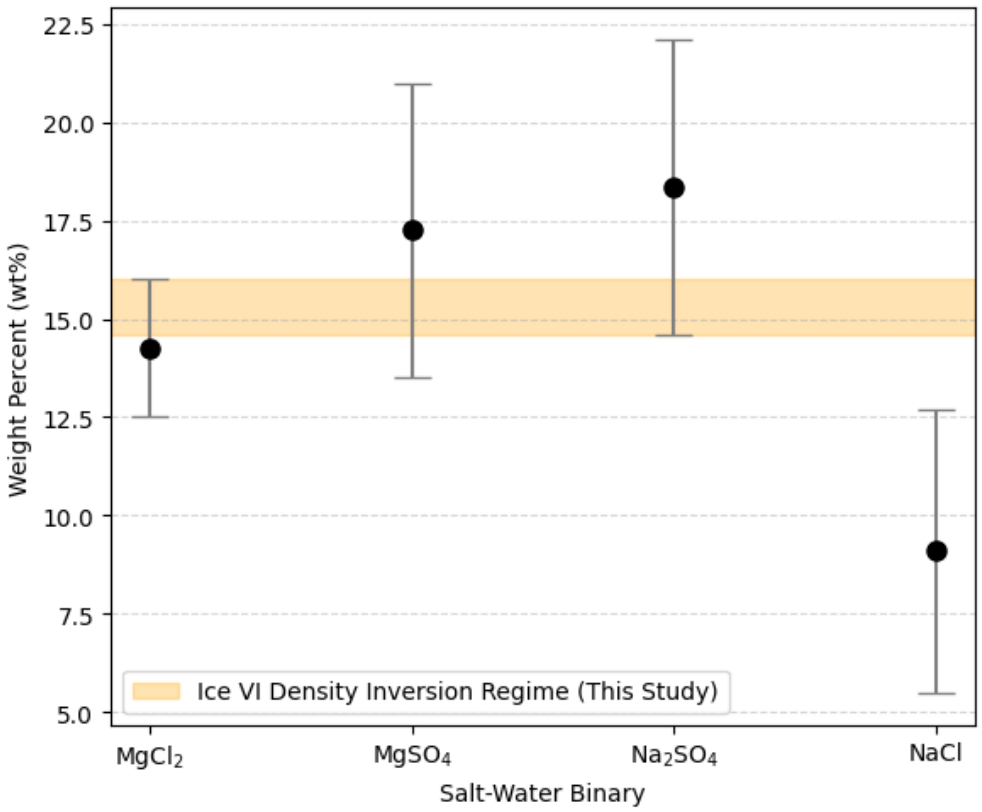

Figure 4.19: A chart comparing the range of concentrations for the density inversion of ice VI in aqueous salt solutions. The plot includes data for NaCl from Journaux et al. (2013) [16]. There is no concentration regime in which density inversions are observed for all salts; however, of the three salts presented in this study, a region exists between 14.6 and 16 wt%.

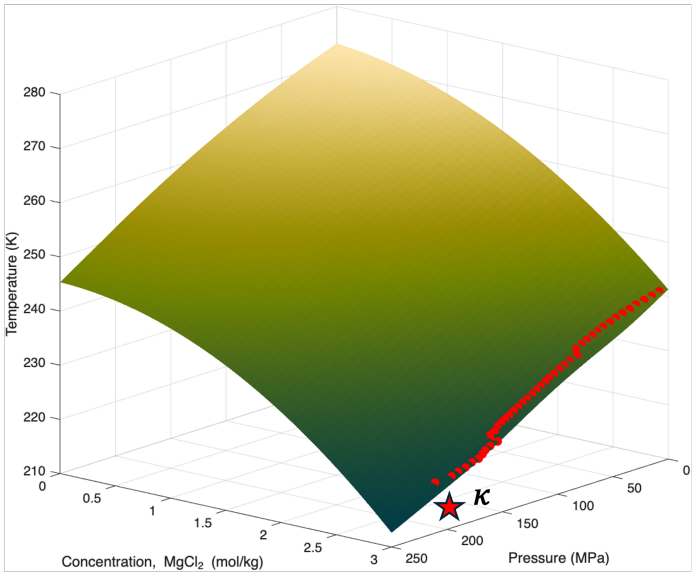

Figure 4.20: The cenotectic profile of aqueous $MgCl_2$ (red dots) projected onto its ice Ih melting surface up to 210 MPa, from the "slow cooling" data set provided by Zarriz et al. (2024) [20]. At the definition of the cenotectic (κ), the concentration is about 2.9 m. The coordinates in pressure, concentration, and temperature space fall between (204.50 MPa, 2.94 m, 218.65 K) and (224.18 MPa, 2.86 m, 218.15 K).

cenotectic is found at about 2.9 m for aqueous $MgCl_2$, the same concentration of the eutectic point at atmospheric pressure. In contrast, a decrease in salt concentration along the eutectic and towards the cenotectic was predicted and observed for salts like NaCl (from 5.2 to 4.8 m) [20]. $MgCl_2$ solutions contained intermediate, metastable hydrate species—some of which represent potential new salt-bearing solid phases—and behaved heterogeneously from sample to sample [20]. While a "slow cooling" methodology was implemented to limit variation, different hydrates induce different liquidus topologies, which require more work to identify. If anything, concentrations, unlike pressures, for cenotectic compositions are not easily predicted without the fundamental thermodynamic data provided here.

4.5 Conclusion

The high-pressure, low-temperature melting curves of ice VI for simple salt-water binaries of $MgSO_4$, Na_2SO_4, and $MgCl_2$ are reported. Melting curves of ice Ih at elevated pressures for $MgCl_2$ solutions are also reported. The novel, thermodynamic data sets are used to produce liquidus surfaces for ices Ih and VI, making the corresponding regions of the phase diagrams for salt systems known at concentrations up to 3 molal.

An ideal mixing model is implemented using the SeaFreeze package [33]. Comparison of model predictions to real data reveals that the freezing point depression of simple salt solutions in water appears to conform to ideality at concentrations of about 1 molal and pressures up to one gigapascal. The implications of near-ideal behavior on solvation properties and net solute-solvent interactions at high pressure are incredibly interesting and warrant further investigation. These results are also pertinent to the predicted interior structures of ocean worlds, density inversions of high-pressure phases of ice, and eutectic and cenotectic compositions of aqueous salts.

Future efforts should include ternary and quaternary salt-water systems containing common ions. If the ideal model also matches the sum contributions of individual salts, it would serve as a reliable predictor of the phase diagram for sea water based on the moderation of colligative properties at pressure.

References

1. Girolami, G. S. A Brief History of Thermodynamics, As Illustrated by Books and People. *J. Chem. Eng. Data* **65,** 298–311 (2020).

2. Blagden, C. X. Experiments on the cooling of water below its freezing point. *Phil. Trans. R. Soc.* **78,** 125–146 (1788).

3. Raoult, F.-M. in *A Source Book in Chemistry 1400-1900* (eds Leicester, H. M. & Klickstein, H. S.) (Harvard University Press, 1952).

4. Atkins, P. W., De Paula, J. & Keeler, J. *Atkins' Physical Chemistry* (Oxford University Press, 2018).

5. Arrhenius, S. in *Nobel Lectures, Chemistry 1901-1921* (Elsevier Publishing Company, 1966).

6. Haghighi, H., Chapoy, A. & Tohidi, B. Freezing Point Depression of Electrolyte Solutions: Experimental Measurements and Modeling Using the Cubic-Plus-Association Equation of State. *Ind. Eng. Chem. Res.* **47,** 3983–3989 (2008).

7. Pillay, V. *et al.* $MgSO_4$ + H_2O System at Eutectic Conditions and Thermodynamic Solubility Products of $MgSO_4{\cdot}12H_2O$(s) and $MgSO_4{\cdot}7H_2O$(s). *J. Chem. Eng. Data* **50,** 551–555 (2005).

8. Denson, J., Chevrier, V., Sears, D. & Ivey, D. M. *Sulfate Reduction: A Model for Subsurface Martian Life* in *Bioastronomy 2007: Molecules, Microbes and Extraterrestrial Life* (2007), 213.

9. Brand, H. E. A., Fortes, A. D., Wood, I. G., Knight, K. S. & Vočadlo, L. The thermal expansion and crystal structure of mirabilite ($Na_2SO_4{\cdot}10D_2O$) from 4.2 to 300 K, determined by time-of-flight neutron powder diffraction. *Phys. Chem. Miner.* **36,** 29–46 (2009).

10. Dougherty, A. J., Avidon, J. A., Hogenboom, D. L. & Kargel, J. S. *Eutectic temperatures for low and high pressure phases of sodium sulfate hydrates with applications to Europa* in *43rd Lunar and Planetary Science Conference* (2012), 2321.

11. Johnson, K. S. & Pytkowicz, R. M. Ion association of chloride and sulphate with sodium, potassium, magnesium and calcium in seawater at 25°C. *Mar. Chem.* **8,** 87–93 (1979).

12. Nesbitt, H. W. Activity coefficients of ions in alkali and alkaline-earth chloride dominated waters including seawater. *Chem. Geol.* **43,** 127–142 (1984).

13. Glasstone, S. *An Introduction To Electrochemistry* (New York: D. Van Nostrand Company, inc., 1942).

14. Adams, L. H. Equilibrium in Binary Systems Under Pressure. I. An Experimental and Thermodynamic Investigation of the System, NaCl-H_2O, at 25°. *J. Am. Chem. Soc.* **53,** 3769–3813 (1931).

15. Nakamura, R. & Ohtani, E. The high-pressure phase relation of the $MgSO_4$–H_2O system and its implication for the internal structure of Ganymede. *Icarus* **211,** 648–654 (2011).

16. Journaux, B., Daniel, I., Caracas, R., Montagnac, G. & Cardon, H. Influence of NaCl on ice VI and ice VII melting curves up to 6 GPa, implications for large icy moons. *Icarus* **226,** 355–363 (2013).

17. Kanno, H. & Angell, C. A. Homogeneous nucleation and glass formation in aqueous alkali halide solutions at high pressures. *J. Phys. Chem.* **81,** 2639–2643 (1977).

18. Hogenboom, D. L., Kargel, J. S., Ganasan, J. P. & Lee, L. Magnesium Sulfate-Water to 400 MPa Using a Novel Piezometer: Densities, Phase Equilibria, and Planetological Implications. *Icarus* **115,** 258–277 (1995).

19. Tanaka, Y., Hada, S., Makita, T. & Moritoki, M. Effect of pressure on the solid-liquid phase equilibria in (water + sodium sulfate) system. *Fluid Phase Equilib.* **76,** 163–173 (1992).

20. Zarriz, A., Journaux, B. & Powell-Palm, M. J. On the equilibrium limit of liquid stability in pressurized aqueous systems. *Nat. Commun.* **15,** 10666 (2024).

21. Vance, S. D., Journaux, B., Hesse, M. & Steinbrügge, G. The Salty Secrets of Icy Ocean Worlds. *J. Geophys. Res.: Planets* **126,** e2020JE006736 (2021).

22. Vance, S., Bouffard, M., Choukroun, M. & Sotin, C. Ganymede's internal structure including thermodynamics of magnesium sulfate oceans in contact with ice. *Planet. Space Sci.* **96,** 62–70 (2014).

23. Kargel, J. S. Brine volcanism and the interior structures of asteroids and icy satellites. *Icarus* **94,** 368–390 (1991).

24. Sohl, F., Spohn, T., Breuer, D. & Nagel, K. Implications from Galileo Observations on the Interior Structure and Chemistry of the Galilean Satellites. *Icarus* **157,** 104–119 (2002).

25. Fredriksson, K. & Kerridge, J. F. Carbonates and Sulfates in CI Chondrites: Formation by Aqueous Activity on the Parent Body. *Meteoritics* **23,** 35–44 (1988).

26. Carlson, R. W. *et al.* in *Europa* (eds Pappalardo, R. T., McKinnon, W. B. & Khurana, K.) 283–327 (University of Arizona Press, 2009).

27. Cartwright, R. J. Evidence for Sulfur-bearing Species on Callisto's Leading Hemisphere: Sourced from Jupiter's Irregular Satellites or Io? *Astrophys. J. Lett.* **902,** L38 (2020).

28. Schneider, N. M. & Bagenal, F. in *Io After Galileo: A New View of Jupiter's Volcanic Moon* (eds Lopes, R. M. C. & Spencer, J. R.) 265–286 (Springer, 2007).

29. Johnson, R. E. *et al.* in *Jupiter: The Planet, Satellites and Magnetosphere* (eds Bagenal, F., Dowling, T. E. & McKinnon, W. B.) 485–512 (Cambridge University Press, 2004).

30. King, O. & Fletcher, L. N. Global Modeling of Ganymede's Surface Composition: Near-IR Mapping From VLT/SPHERE. *J. Geophys. Res.: Planets* **127,** e2022JE007323 (2022).

31. Zolotov, M. Y. Aqueous fluid composition in CI chondritic materials: Chemical equilibrium assessments in closed systems. *Icarus* **220,** 713–729 (2012).

32. Journaux, B. *et al.* Large Ocean Worlds with High-Pressure Ices. *Space Sci. Rev.* **216,** 7 (2020).

33. Journaux, B. *et al.* Holistic Approach for Studying Planetary Hydrospheres: Gibbs Representation of Ices Thermodynamics, Elasticity, and the Water Phase Diagram to 2,300 MPa. *J. Geophys. Res. E: Planets* **125,** e2019JE006176 (2020).

34. Wagner, W., Riethmann, T., Feistel, R. & Harvey, A. H. New Equations for the Sublimation Pressure and Melting Pressure of H_2O Ice Ih. *J. Phys. Chem. Ref. Data* **40,** 043103 (2011).

35. Bridgman, P. W. The Phase Diagram of Water to 45,000 kg/cm2. *J. Chem. Phys.* **5,** 964–966 (1937).

36. Sohl, F. *et al.* Subsurface Water Oceans on Icy Satellites: Chemical Composition and Exchange Processes. *Space Sci. Rev.* **153,** 485–510 (2010).

37. Bollengier, O. *et al.* Phase equilibria in the H_2O–CO_2 system between 250–330 K and 0–1.7 GPa: Stability of the CO_2 hydrates and H_2O-ice VI at CO_2 saturation. *Geochim. Cosmochim. Acta* **119,** 322–339 (2013).

38. Bollengier, O., Brown, J. M., Journaux, B., Vance, S. & Tobie, G. *Getting Salty! High-Pressure Thermodynamic Properties of Na-Mg-Cl-SO_4 Aqueous Solutions for Icy Worlds.* in *2022 Astrobiology Science Conference* (2022).

39. Vance, S. D. *et al.* Geophysical Investigations of Habitability in Ice-Covered Ocean Worlds. *J. Geophys. Res. E: Planets* **123,** 180–205 (2018).

40. Styczinski, M. J., Vance, S. D. & Melwani Daswani, M. PlanetProfile: Self-Consistent Interior Structure Modeling for Ocean Worlds and Rocky Dwarf Planets in Python. *Earth Space Sci.* **10,** e2022EA002748 (2023).

41. Brown, J. M. Local basis function representations of thermodynamic surfaces: Water at high pressure and temperature as an example. *Fluid Phase Equilib.* **463,** 18–31 (2018).

42. Valenti, P., Bodnar, R. J. & Schmidt, C. Experimental determination of H_2O–NaCl liquidi to 25 mass% NaCl and 1.4 GPa: Application to the Jovian satellite Europa. *Geochim. Cosmochim. Acta* **92,** 117–128 (2012).

43. Mao, H. K., Xu, J. & Bell, P. M. Calibration of the ruby pressure gauge to 800 kbar under quasi-hydrostatic conditions. *J. Geophys. Res.: Solid Earth* **91,** 4673–4676 (1986).

44. Journaux, B. *et al.* Salt partitioning between water and high-pressure ices. Implication for the dynamics and habitability of icy moons and water-rich planetary bodies. *Earth Planet. Sci. Lett.* **463,** 36–47 (2017).

45. Crameri, F., Shephard, G. E. & Heron, P. J. The misuse of colour in science communication. *Nat. Commun.* **11,** 5444 (2020).

46. DeVoe, H. *Thermodynamics and Chemistry (DeVoe)* [Online; accessed 2025-08-03]. 2022.

47. Bollengier, O., Brown, J. M. & Shaw, G. H. Thermodynamics of pure liquid water: Sound speed measurements to 700 MPa down to the freezing point, and an equation of state to 2300 MPa from 240 to 500 K. *J. Chem. Phys.* **151,** 054501 (2019).

48. Katayama, Y. *et al.* Structure of liquid water under high pressure up to 17 GPa. *Phys. Rev. B* **81,** 014109 (2010).

49. Yamaguchi, T., Fukuyama, N., Yoshida, K. & Katayama, Y. Ion Solvation and Water Structure in an Aqueous Sodium Chloride Solution in the Gigapascal Pressure Range. *J. Phys. Chem. Lett.* **12,** 250–256 (2021).

50. Millero, F. J., Feistel, R., Wright, D. G. & McDougall, T. J. The composition of Standard Seawater and the definition of the Reference-Composition Salinity Scale. *Deep Sea Res. Part I* **55,** 50–72 (2008).

51. McDougall, T. J. & Barker, P. M. *Getting started with TEOS-10 and the Gibbs seawater (GSW) oceanographic toolbox* 1–28. ISBN: 978-0-646-55621-5 (SCOR/IAPSO WG127, 2011).

Appendix A

CHAPTER 3 SUPPLEMENTARY INFORMATION

A.1 Supplementary Methods

A.1.1 Raman Spectroscopy

Raman spectroscopy (and PL) experiments were conducted using a custom-built optical setup. A single-mode Coherent 532 nm laser (Sapphire 532 SF NX) with a maximum output power of 150 mW served as the excitation source. The laser intensity was adjusted using a variable neutral density (ND) filter to 1 mW. The laser beam was directed onto the sample via silver-coated plane mirrors and a NoiseBlock 90/10 beam-splitter (BS-532.2-5-90/10-1") and focused through a 10X Mitutoyo Plan Apochromat long-working distance objective lens (0.28 NA) for precise Raman scattering collection. The back-scattered light was collected and filtered using three OD3 532 nm Bragg notch filters (RFS-OD3-11M) to suppress the Rayleigh scattered light, allowing the detection of Raman signals starting from 100 cm^{-1}. The filtered signal was routed to a Princeton Instruments ISO-Plane 320 spectrometer, and the Raman spectra were recorded using a thermoelectrically cooled PIXIS 100 BRX CCD detector, operating at -75 °C for optimal sensitivity. Sample alignment and visualization were achieved using an integrated IDS Imaging Color CMOS camera, illuminated by a white light source coupled with a fiber.

A.1.2 Pressure Calibrations

Pressure calibrations for each sample squeeze assay, leveraging either ruby photoluminescence (PL) or diamond anvil Raman scattering, were performed on an identical optical setup as previously described (above). Pressure was calculated as is typical [1–3].

A.1.3 UV-visible (UV-Vis) Spectroscopy

UV-Vis was measured using both a Thermo Scientific Evolution 300 spectrophotometer and a Thermo Scientific NanoDrop One microvolume spectrophotometer. Single scans at a variety of working concentrations were collected and compared to determine the molar extinction coefficient at 280 nm of type III AFP in water. Scans for the Evolution 300 were performed in a 1 cm path length quartz cuvette and background subtracted. Aqueous samples for the NanoDrop were placed directly onto the instrument anvil.

A.1.4 Circular Dichroism (CD) Spectroscopy

CD was measured using a Jasco 1500 CD spectrophotometer at room temperature. Three scans in the far-UV between 180 nm and 260 nm were collected and averaged for 0.1 mg/mL type III AFP in water. Scans were performed in a 1 mm path length quartz cuvette.

A.1.5 Sample Degradation

To produce the naturally-occuring degradation products of IBP 8, a fresh sample solution of 1 mg/mL IBP 8 in 0.5 m NaCl (aq) was prepared and tested via splat assay to confirm activity. Two degradation pathways were explored—under ambient conditions, and at pressure. Under ambient conditions, the remaining sample solution was placed in a sealed tube and transferred to a sand bath. The sand bath ensured that the sample temperature remained stable between 20 and 25 °C and that the sample was not exposed to light. At pressure, following the initial splat assay, the sample pressure was decreased to around 800 MPa to remain in the liquid phase, and the DAC was also stored away from any light sources. After three weeks, sample solutions were re-tested via squeeze assay and determined to have no significant IRI activity.

A.1.6 PCA on MS/MS Spectra

In order to guide sample interpretation, principal component analysis (PCA) was performed on tandem mass spectrometry (MS/MS) results in python. For PCA, the top 150 raw

intensity values were extracted from MS/MS plots using gaussian filtering (sigma = 1; peak threshold = 0.1) for m/z 150 - 1500. Raw intensity values were then analyzed and plotted using PCA from the sklearn.decomposition module from scikite-learn in [4].

A.2 Supplementary Figures

A.2.1 Characterization of Type III AFP

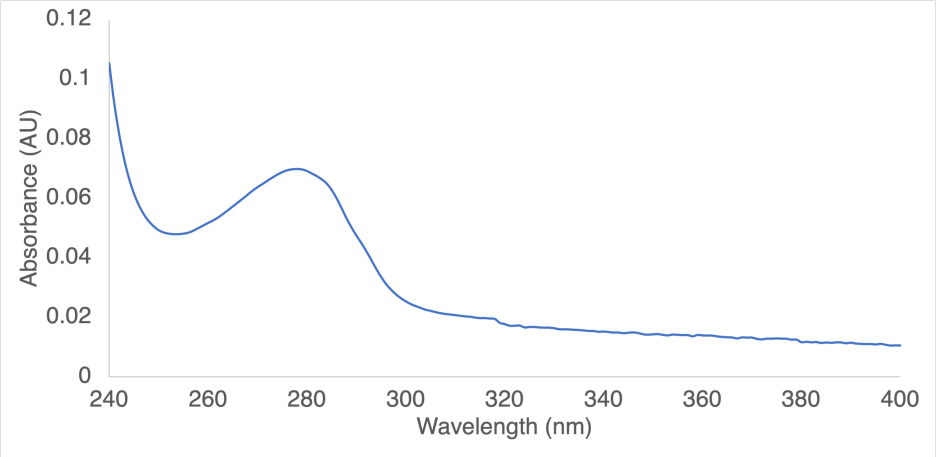

Figure A.1: UV-Vis spectrum of 0.33 mg/mL type III AFP in water. Extinction coefficient determination used in tandem with far-UV CD to confirm integrity of type III AFP prior to pressurization via squeze assay.

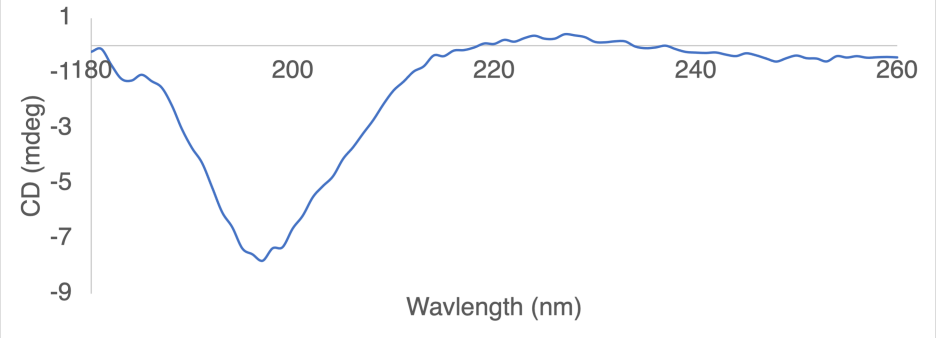

Figure A.2: Far-UV CD spectrum of type III AFP in water. Spectrum used in tandem with UV-Vis to confirm integrity of type III AFP prior to pressurization via squeeze assay.

A.2.2 Squeeze Assay Pressure Calibration and Raman Spectroscopy

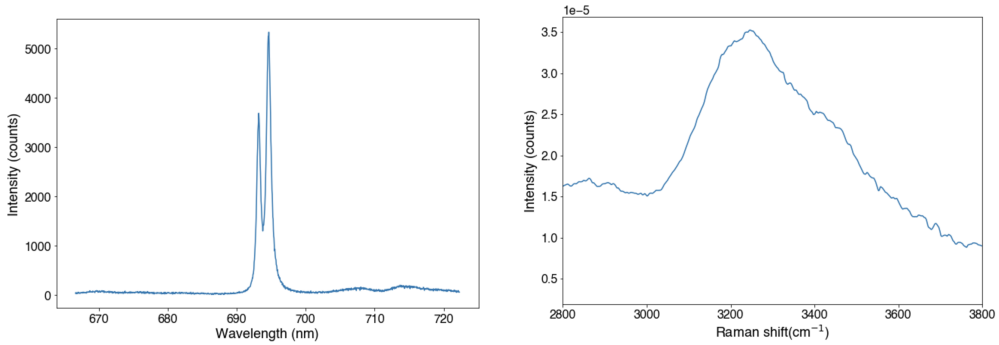

(a) (b)

Figure A.3: Characterizing spectra for 0.5 m NaCl sample solution during squeeze assay via (a) ruby PL and (b) water Raman. The ruby PL indicates a sample pressure of 1.21 GPa. The Raman spectrum of the OH symmetric stretching mode for water confirms the phase is ice VI.

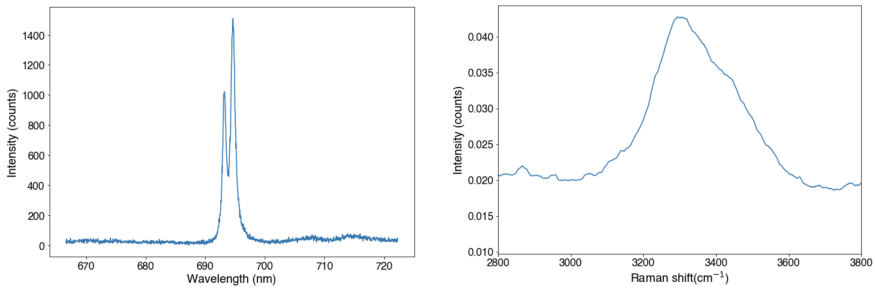

(a) (b)

Figure A.4: Characterizing spectra for 1 mg/mL non-ice-binding peptide sample solution during squeeze assay via (a) ruby PL and (b) water Raman. The ruby PL indicates a sample pressure of 1.21 GPa. The Raman spectrum of the OH symmetric stretching mode for water confirms the phase is ice VI.

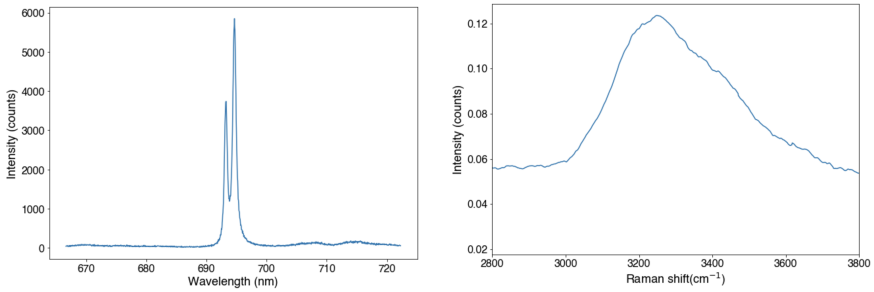

(a) (b)

Figure A.5: Characterizing spectra for 0.1 mg/mL type III AFP sample solution during squeeze assay via (a) ruby PL and (b) water Raman. The ruby PL indicates a sample pressure of 1.21 GPa. The Raman spectrum of the OH symmetric stretching mode for water confirms the phase is ice VI.

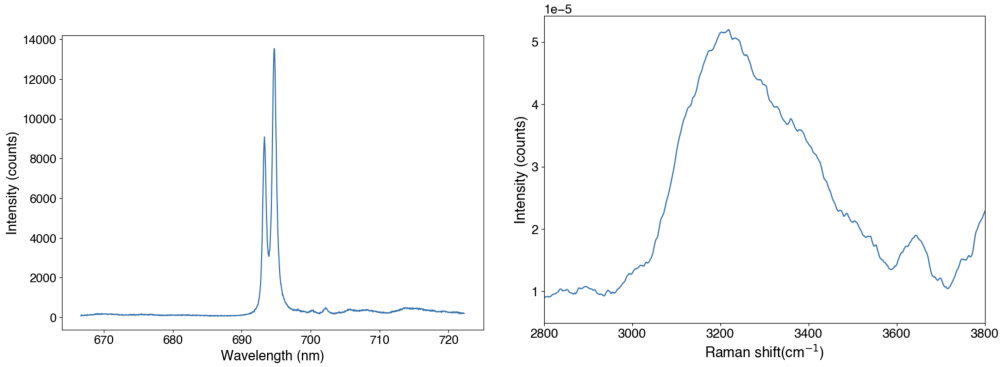

(a) (b)

Figure A.6: Characterizing spectra for 1 mg/mL IBP 8 sample solution during squeeze assay via (a) ruby PL and (b) water Raman. The ruby PL indicates a sample pressure of 1.32 GPa. The Raman spectrum of the OH symmetric stretching mode for water confirms the phase is ice VI.

A.2.3 Squeeze Assay Micrograph Segmentation

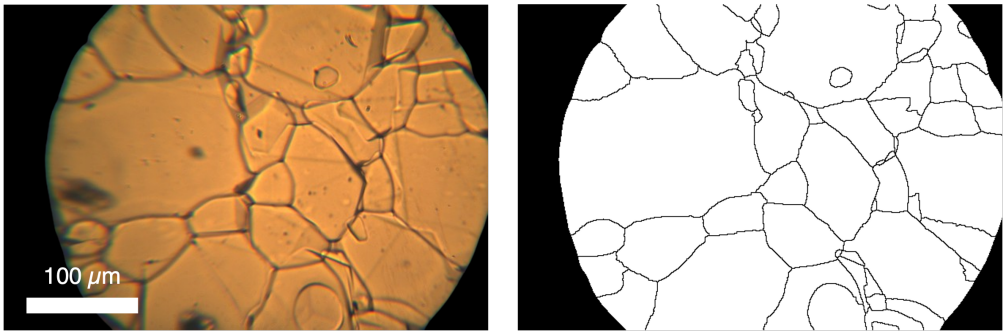

Figure A.7: Side-by-side comparison of (left) 0.5 *m* NaCl sample solution and (right) watershed plot for grain size analysis following 30 minutes of ice VI recrystallization at pressure. Scale bar is 100 µm. Segmentation map is as generated by the interactive software, and provides a rough approximation of grain metrics.

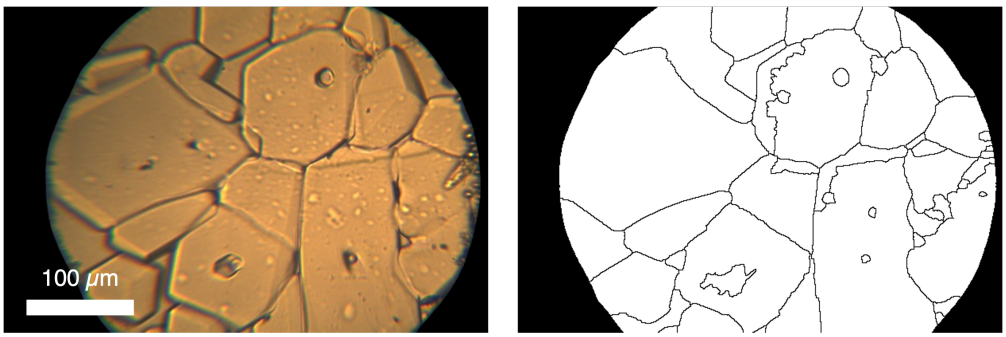

Figure A.8: Side-by-side comparison of (left) 1 mg/mL non-ice-binding peptide sample solution and (right) watershed plot for grain size analysis following 30 minutes of ice VI recrystallization at pressure. Scale bar is 100 µm. Segmentation map is as generated by the interactive software, and provides a rough approximation of grain metrics.

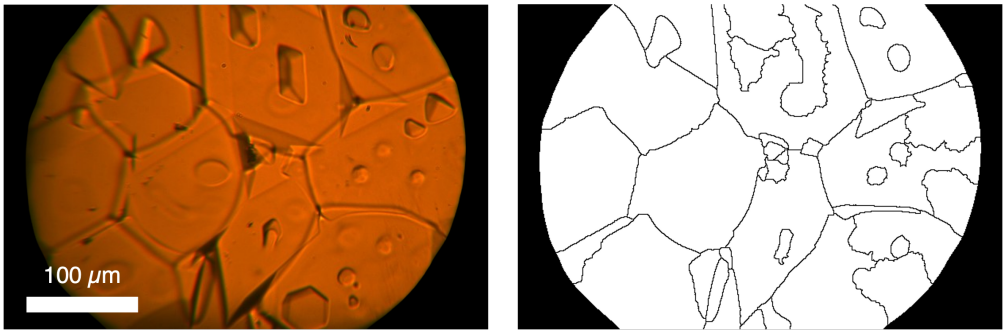

Figure A.9: Side-by-side comparison of (left) 0.1 mg/mL type III AFP sample solution and (right) watershed plot for grain size analysis following 30 minutes of ice VI recrystallization at pressure. Scale bar is 100 µm. Segmentation map is as generated by the interactive software, and provides a rough approximation of grain metrics.

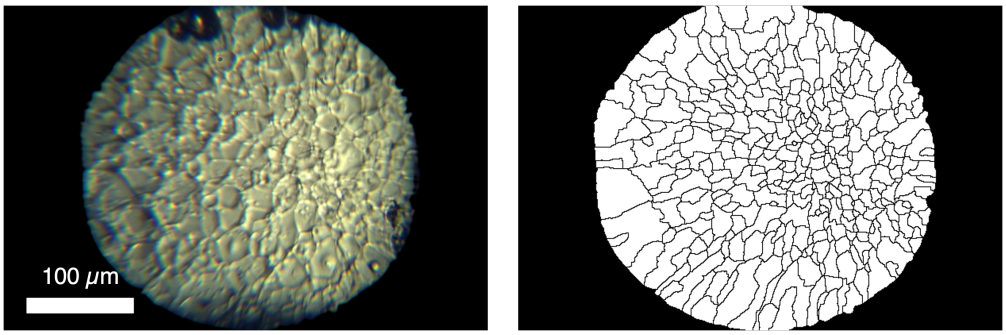

Figure A.10: Side-by-side comparison of (left) 1 mg/mL IBP 8 sample solution and (right) watershed plot for grain size analysis following 30 minutes of ice VI recrystallization at pressure. Scale bar is 100 µm. Segmentation map is as generated by the interactive software, and provides a rough approximation of grain metrics.

A.2.4 Degradation Panel and Characterization

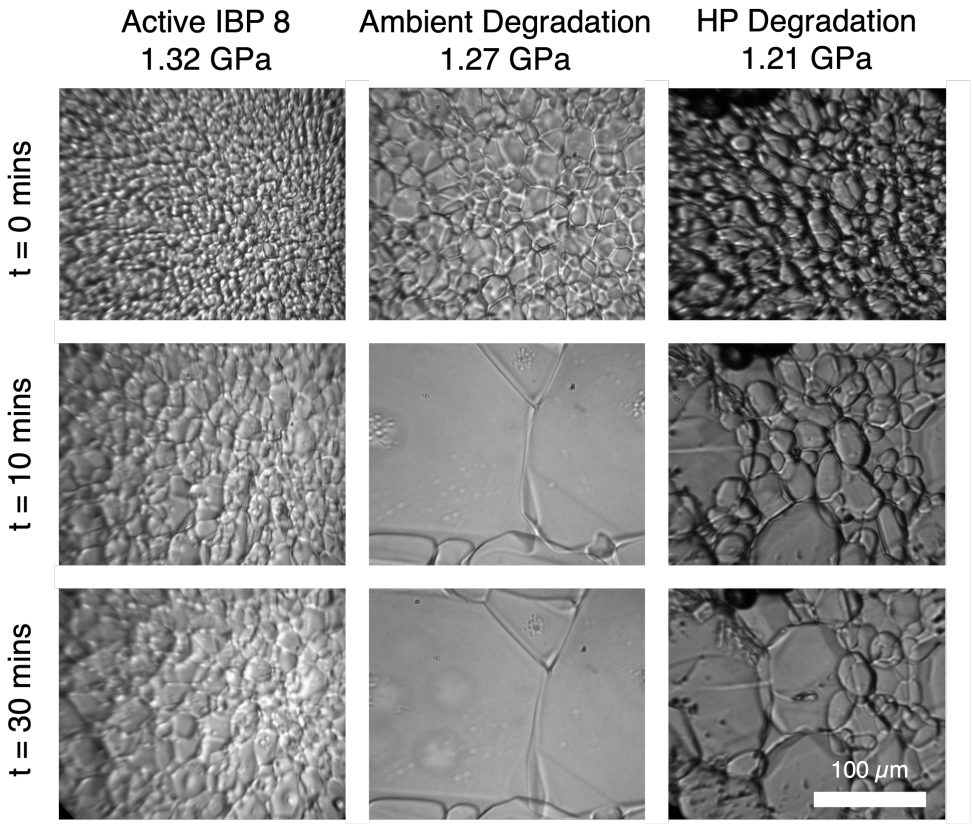

Figure A.11: Micrographs of squeeze assays for degradation experiments up to 30 minutes of ice VI growth. All samples are prepared in chambers of equivalent dimensions to minimize grain boundary overlap and held under static pressure following the onset of crystal growth. Scale bar (top left) is 100 µm and consistent for all micrographs. Sample information is given in section A.1.5.

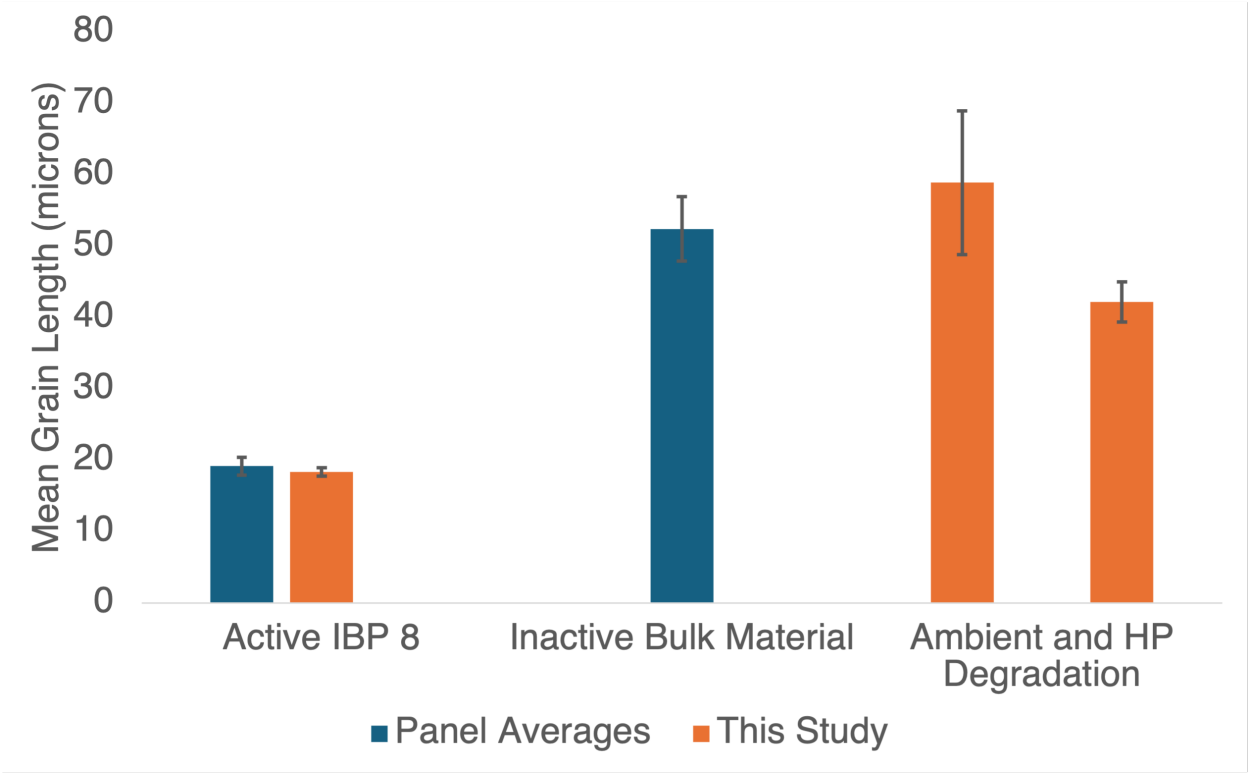

Figure A.12: Comparison of mean grain length with respect to fresh IBP 8 solution and solutions containing degraded peptide as described in section A.1.5 and shown in Figure A.11, denoted as "This Study." Panel averages are given.

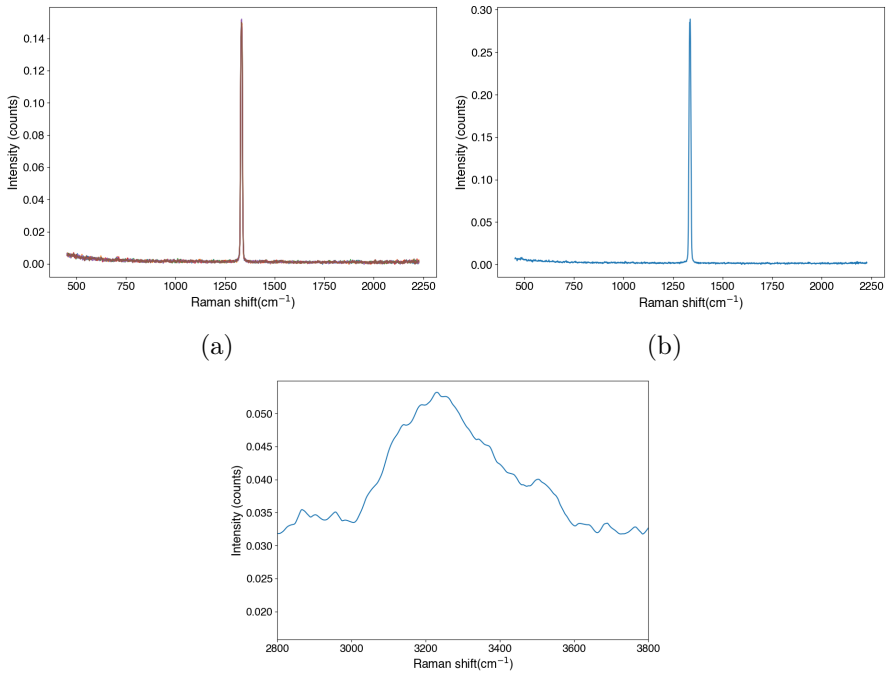

Figure A.13: Characterizing spectra for 1 mg/mL IBP 8 sample solution degraded under ambient conditions via (a) external diamond anvil Raman, (b) internal diamond anvil Raman, and (c) water Raman. The external anvil Raman is at ambient pressure, while the internal anvil Raman is at high pressure. Combined, the calibration indicates a sample pressure of 1.27 GPa. The Raman spectrum of the OH symmetric stretching mode for water confirms the phase is ice VI.

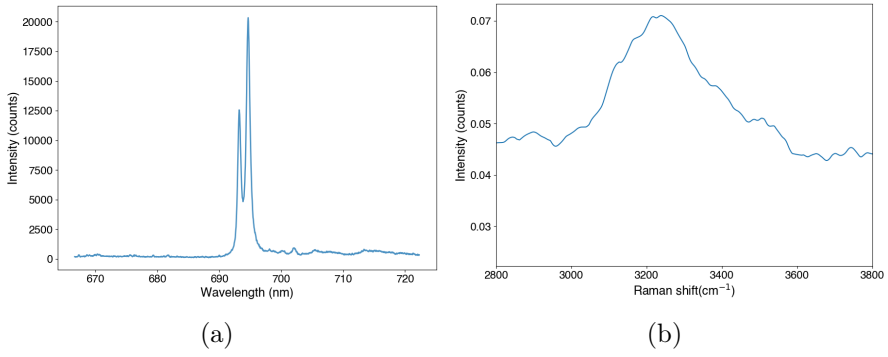

Figure A.14: Characterizing spectra for 1 mg/mL IBP 8 sample solution degraded under high-pressure conditions via (a) ruby PL and (b) water Raman. The ruby PL indicates a sample pressure of 1.21 GPa. The Raman spectrum of the OH symmetric stretching mode for water confirms the phase is ice VI.

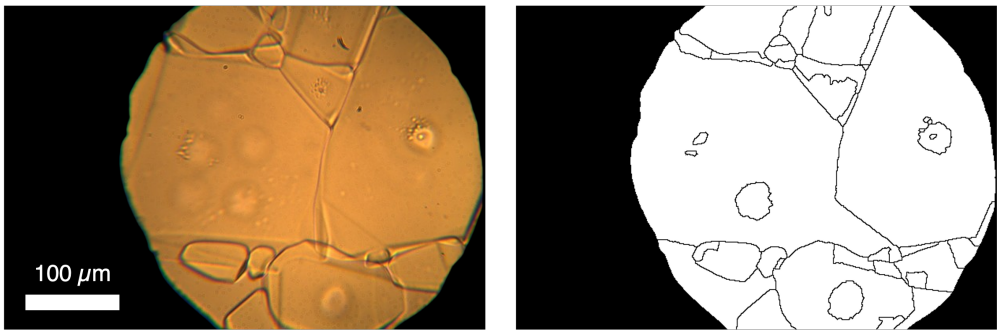

Figure A.15: Side-by-side comparison of (left) 1 mg/mL IBP 8 sample solution degraded under ambient conditions and (right) watershed plot for grain size analysis following 30 minutes of ice VI recrystallization at pressure. Scale bar is 100 µm. Segmentation map is as generated by the interactive software, and provides a rough approximation of grain metrics.

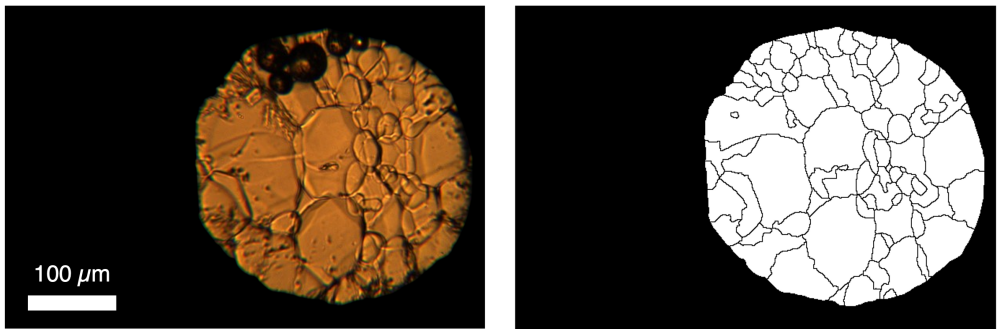

Figure A.16: Side-by-side comparison of (left) 1 mg/mL IBP 8 sample solution degraded under high-pressure conditions and (right) watershed plot for grain size analysis following 30 minutes of ice VI recrystallization at pressure. Scale bar is 100 µm. Segmentation map is as generated by the interactive software, and provides a rough approximation of grain metrics.

A.2.5 PCA Results and IBP 8 Sequencing

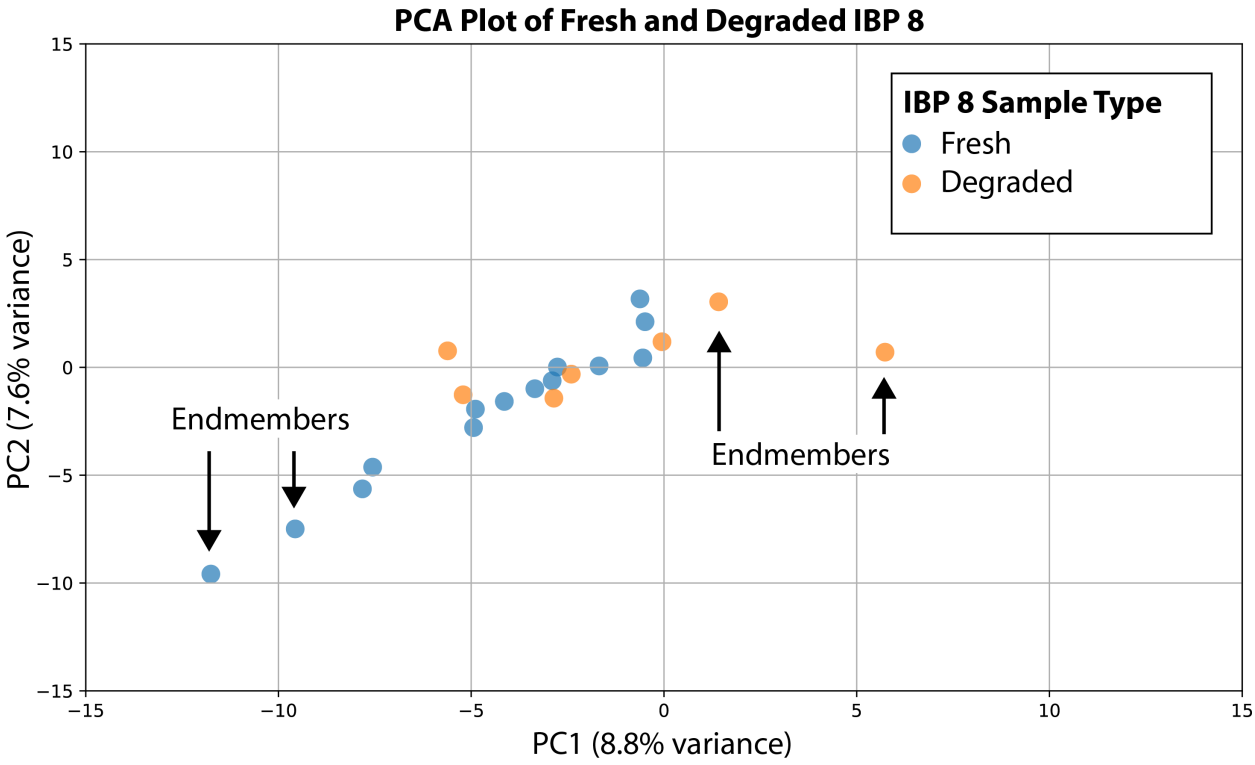

Figure A.17: PCA plot produced on raw intensity values extracted from MS/MS data of IBP 8. Fresh IBP 8 (blue) and degraded IBP 8 (orange) were included.

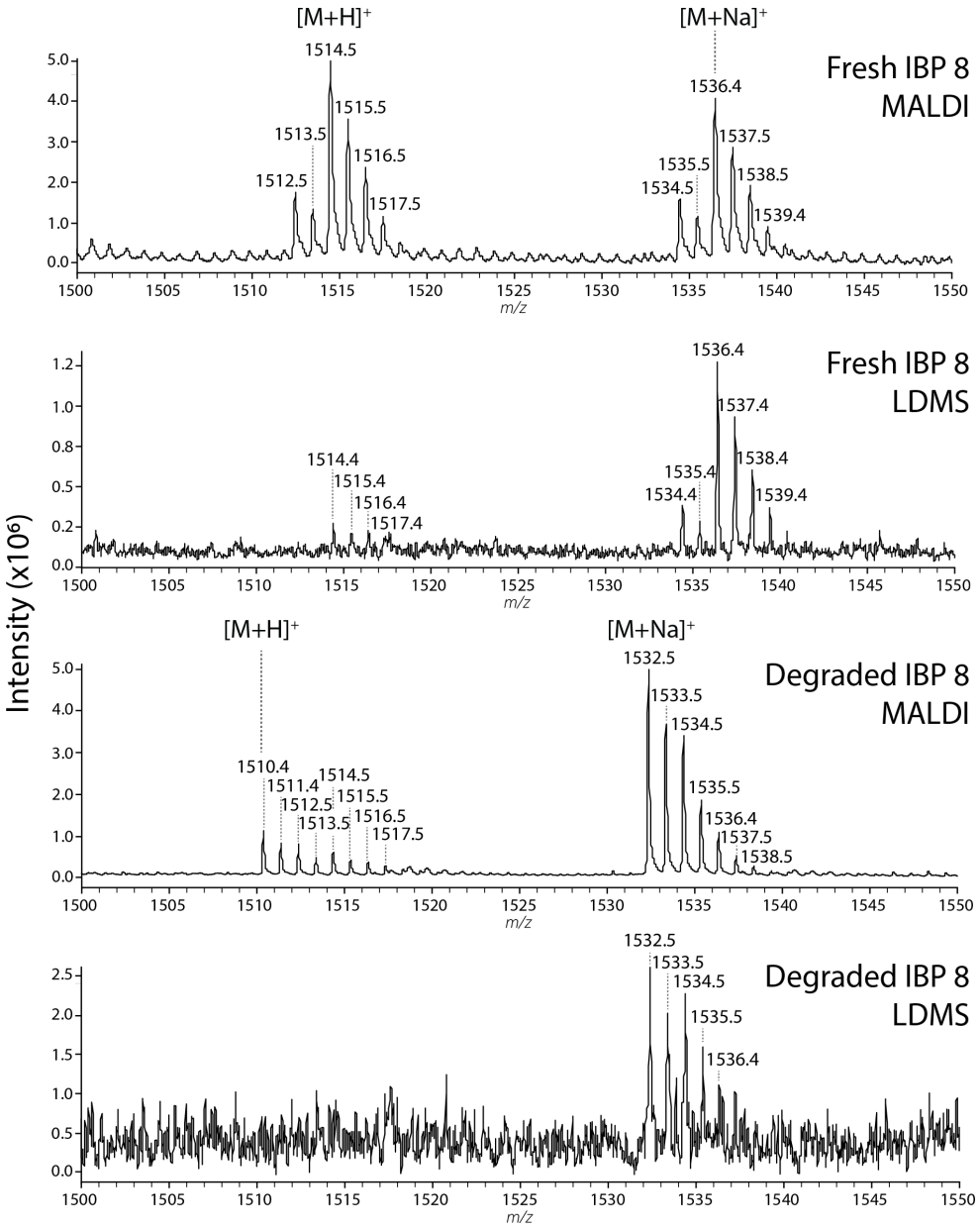

Figure A.18: IBP 8 is detectable with and without a MALDI matrix and spectra of fresh IBP 8 and degraded IBP 8 are distinguishable via both MALDI and LDMS. Spectra shown are of fresh IBP 8 (top half) and degraded IBP 8 (bottom half) both analyzed with CHCA (MALDI) and without CHCA (LDMS) on a commercial Bruker AutofleX maX. Non-sodiated $[M+H_x]^+$ and sodiated $[M+H_x+Na]^+$ peaks are indicated.

Table A.1: IBP 8 sequence, including all peptide fragment labels (Frag. #) and fragment ion masses in Da

IBP 8 Sequence	A, B, C Frag. #	A	B	C	X, Y, Z Frag. #	X	Y	Z
K	1	101.11	129.10	146.13	14	-	1514.59	1497.56
C	2	204.12	232.11	249.14	13	1412.47	1386.49	1369.47
C	3	307.13	335.12	352.15	12	1309.46	1283.48	1266.46
T	4	408.17	436.17	453.19	11	1206.45	1180.47	1163.45
K	5	536.27	564.26	581.29	10	1105.40	1079.42	1062.40
N	6	650.31	678.31	695.33	9	977.31	951.33	934.30
C	7	753.32	781.32	798.34	8	863.27	837.29	820.26
D	8	868.35	896.34	913.37	7	760.26	734.28	717.25
S	9	955.38	983.37	1000.40	6	645.23	619.25	602.23
T	10	1056.43	1084.42	1101.45	5	558.20	532.22	515.19
A	11	1127.46	1155.46	1172.49	4	457.15	431.17	414.15
H	12	1264.52	1292.52	1309.54	3	386.11	360.13	343.11
C	13	1367.53	1395.53	1412.55	2	249.05	223.07	206.05
T	14	1468.58	1496.57	-	1	146.04	120.07	103.04

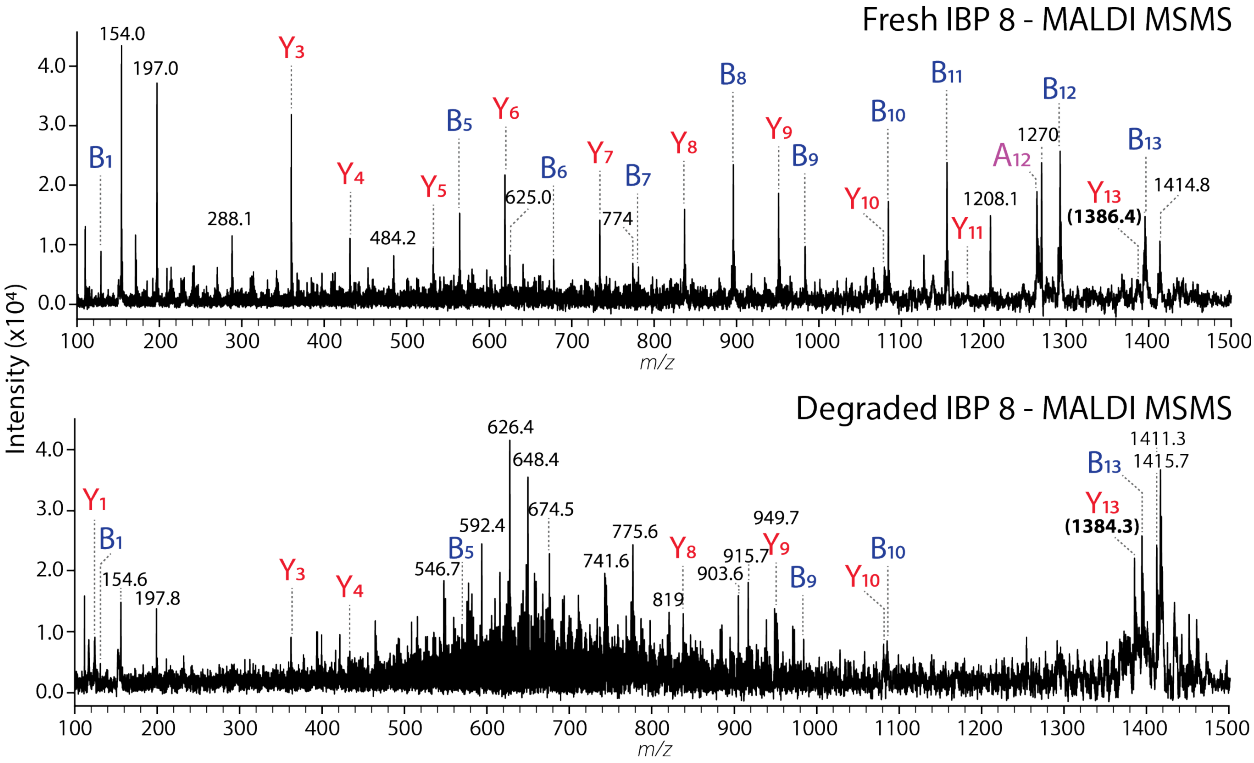

IBP 8 MSMS Fragments		1	2	3	4	5	6	7	8	9	10	11	12	13	14
Fresh IBP 8	Y					+Na	+Na	+Na	+Na		+Na	+Na			
	B							+Na	+Na			+Na	+Na		
Degraded IBP 8	Y								+Na -2Da	-2Da	+Na -2Da			-2Da	-2Da
	B												+Na	+Na -2Da	

+Na = Sodiated fragments ions are observable

-2Da = 2 Da mass shifted peaks are observable

Figure A.19: Top: MS/MS spectra of fresh IBP 8 and degraded IBP 8 collected with a MALDI matrix on m/z 1512.4. B and Y fragment ions are labelled in blue and red respectively. The A_{12} fragment was also detectable (purple) in the fresh spectra. High intensity unidentified ions are marked for reference. A -2 Da shift from fresh to degraded IBP 8 is highlighted in bold for the Y_{13} ion. Bottom: table highlighting the B and Y fragment ions observed across all IBP 8 MS/MS analyses from m/z 1510.4, m/z 1512.4, and m/z 1514.5, with detectable B and Y fragment numbers indicated by filled boxes. Ions detectable in one sample set but missing from the other are indicated with hashed boxes. Ions that contain a -2 Da mass shift from fresh to degraded IBP 8 are indicated. Additionally, peaks that contained MS/MS fragment ions with sodium adducts are indicated.

A.2.6 Impact Ionization Mass Spectrometry

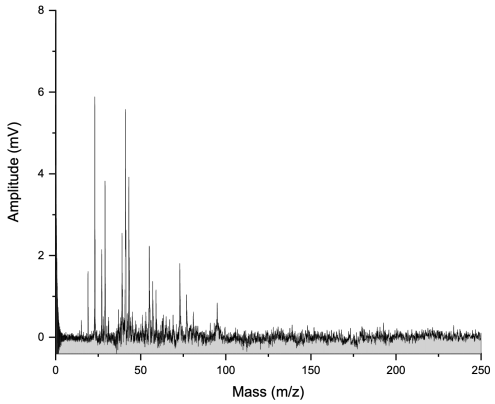

(a)

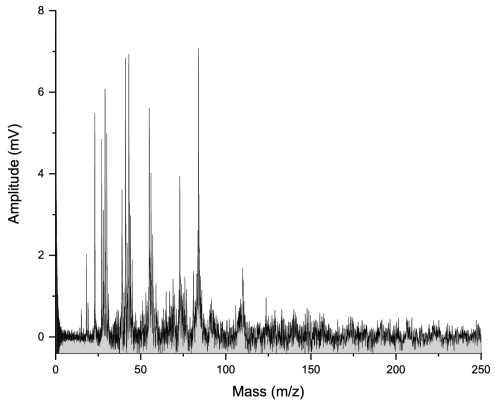

(b)

Figure A.20: Impact ionization mass spectra of ice grains generated using aqueous solutions of 10 mM NaCl (a) and 30 mM IBP 8 (b) collected at an impact velocity of 4 km/s.

References

1. Shen, G. *et al.* Toward an international practical pressure scale: A proposal for an IPPS ruby gauge (IPPS-Ruby2020). *High Pressure Res.* **40,** 299–314 (2020).

2. Datchi, F. *et al.* Optical pressure sensors for high-pressure–high-temperature studies in a diamond anvil cell. *High Pressure Res.* **27,** 447–463 (2007).

3. Akahama, Y. & Kawamura, H. Pressure calibration of diamond anvil Raman gauge to 310 GPa. *J. Appl. Phys.* **100,** 043516 (2006).

4. Pedregosa, F. *et al.* Scikit-learn: Machine Learning in Python. *J. Mach. Learn. Res.* **12,** 2825–2830 (2011).

Appendix B

ASSORTED PHASE DIAGRAMS

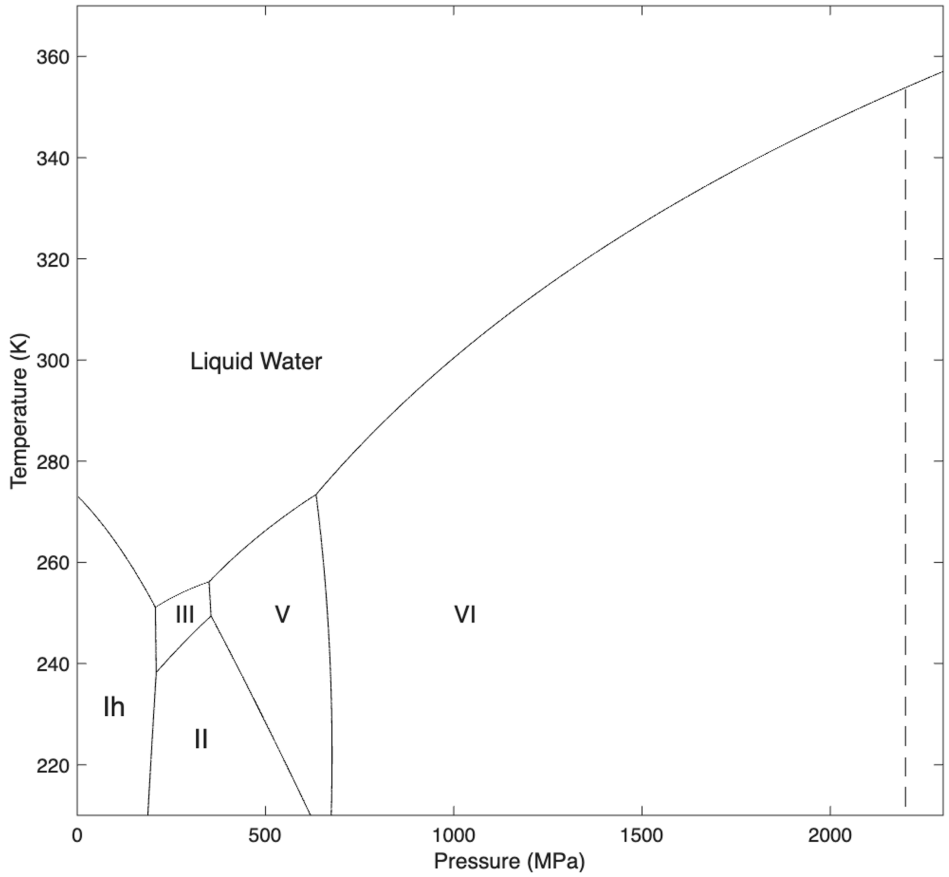

Figure B.1: Water phase diagram from 210 to 370 K and 0.1 to 2300 MPa. Dashed line at 2200 MPa is the solid-solid phase transition from ice VI to ice VII. Phase diagram is modified from Figure 1.1 and produced via SeaFreeze [1].

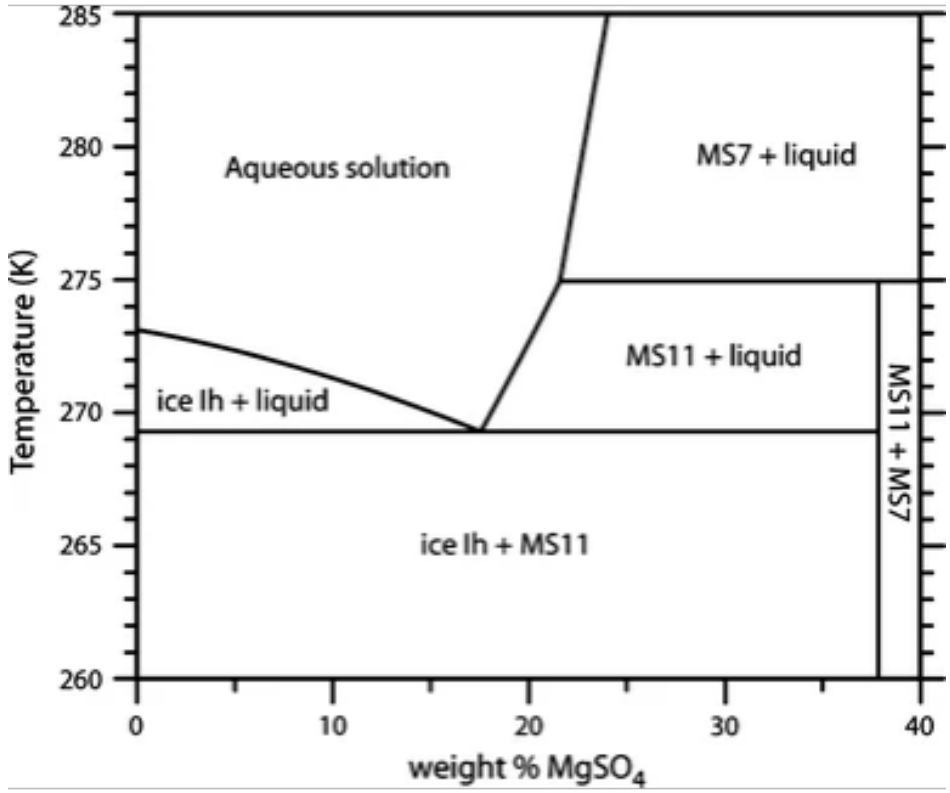

Figure B.2: $MgSO_4$-water phase diagram at ambient pressure, from 260 to 285 K and from 0 to 40 weight percent $MgSO_4$. Magnesium sulfate undecahydrate (MS11) and heptahydrate (MS7) are observed. Phase diagram from Fortes et al. (2008) [2].

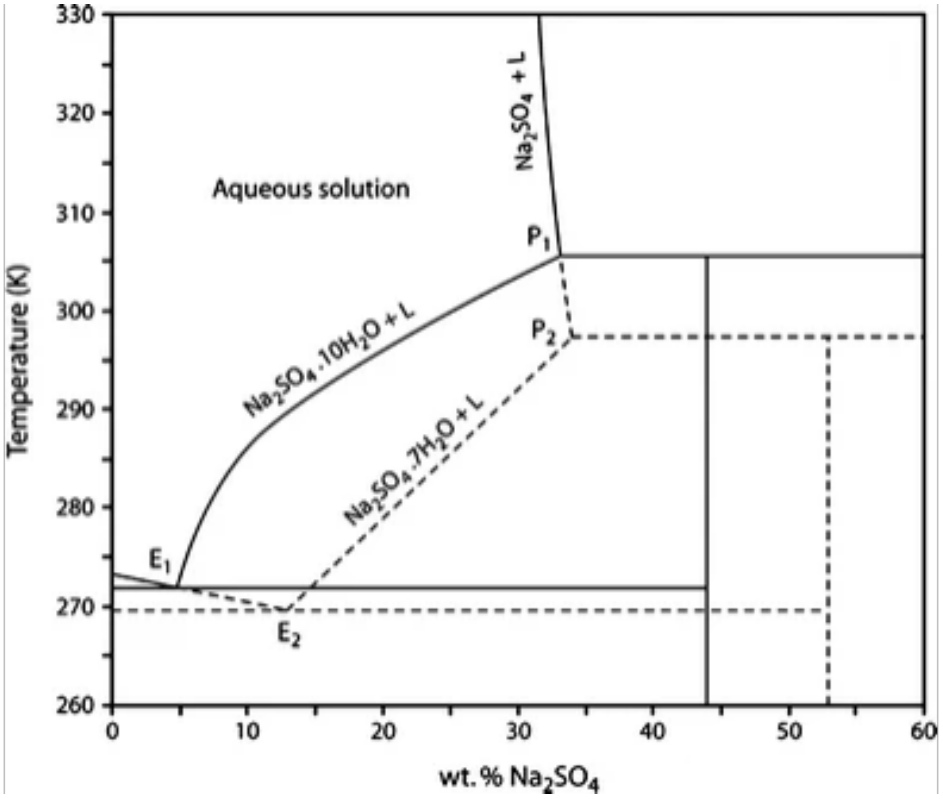

Figure B.3: Na_2SO_4-water phase diagram at ambient pressure, from 260 to 350 K and from 0 to 60 weight percent Na_2SO_4. Sodium sulfate decahydrate and heptahydrate are observed. E1 and E2 are the eutectics for these hydrates with ice, and P1 and P2 are the peritectics for these hydrates with solid sodium sulfate and liquid solution, respectively. Phase diagram from Brand et al. (2009) [3].

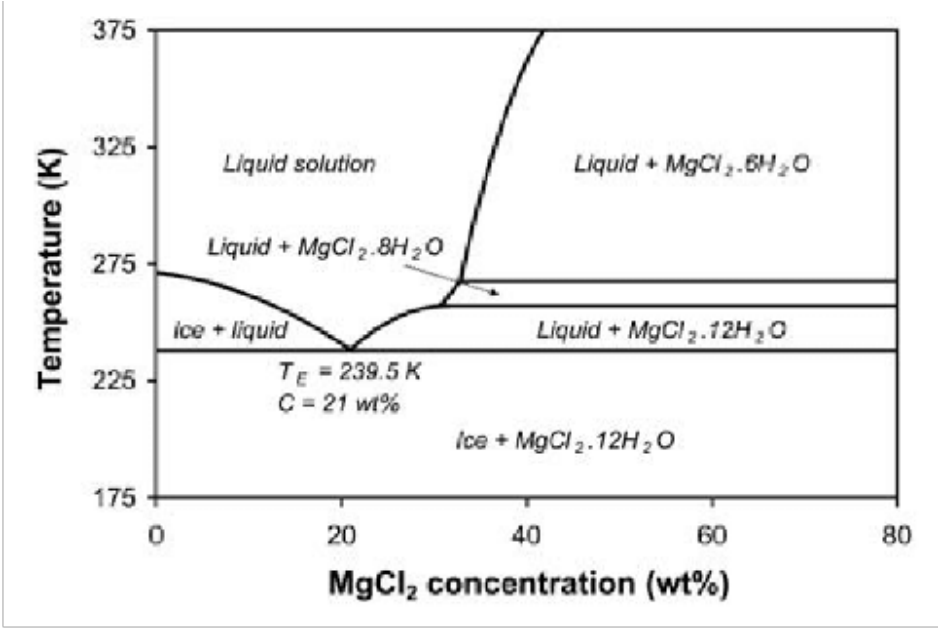

Figure B.4: $MgCl_2$-water phase diagram at ambient pressure, from 175 to 375 K and from 0 to 80 weight percent $MgCl_2$. Magnesium chloride dodecahydrate, octahydrate, and hexahydrate are observed. Phase diagram from Davis et al. (2009) [4].

References

1. Journaux, B. *et al.* Holistic Approach for Studying Planetary Hydrospheres: Gibbs Representation of Ices Thermodynamics, Elasticity, and the Water Phase Diagram to 2,300 MPa. *J. Geophys. Res. E: Planets* **125,** e2019JE006176 (2020).

2. Fortes, A. D., Wood, I. G. & Knight, K. S. The crystal structure and thermal expansion tensor of $MgSO_4$–$11D_2O$(meridianiite) determined by neutron powder diffraction. *Phys. Chem. Miner.* **35,** 207–221 (2008).

3. Brand, H. E. A., Fortes, A. D., Wood, I. G., Knight, K. S. & Vočadlo, L. The thermal expansion and crystal structure of mirabilite ($Na_2SO_4{\cdot}10D_2O$) from 4.2 to 300 K, determined by time-of-flight neutron powder diffraction. *Phys. Chem. Miner.* **36,** 29–46 (2009).

4. Davis, B. L., Chevrier, V. F., Altheide, T. S. & Swaffar, C. *Reflectance Spectra of Low-temperature Chloride and Perchlorate Hydrates and their Relevance to the Martian Surface* in *40rd Lunar and Planetary Science Conference* (2009), 1387.